Università degli Studi di Bergamo

Dipartimento di Ingegneria e Scienze Applicate (Dalmine)

Scuola di Dottorato in
Meccatronica, Informazione,
Tecnologie Innovative e Metodi Matematici

XXVI Ciclo

Integrated Experimental and Modelling Approach for the Characterization of Thermo-Tribological Phenomena in Hot Rolling Processes

Doctoral Dissertation of

Fabio ARIZZI

Advisor: Prof. **Egidio RIZZI**

A Milena

...e alla piccola Flavia

Abstract

In industrial hot rolling processes, contact conditions are strongly influenced by local thermal effects occurring at the interface between tool and workpiece. Indeed, the presence of high temperatures influences the material properties and, hence, the contact conditions. Thus, thermal conditions in the contact zone shall be accurately predicted in order to characterize the contact mechanical behavior.

In the present doctoral dissertation, a comprehensive experimental and modelling methodology is developed, by investigating heat exchange phenomena under hot rolling conditions. Dedicated experimental activities are first designed and carried out on an innovative high-temperature ring-on-ring tribometer in an industrial setting. Then, thermal fluxes under high contact pressures and temperature differences are quantitatively assessed through a numerical procedure of inverse analysis, apt to estimate the heat transfer parameters based on measurements and on an effective mathematical modelling of the underlying physical phenomena.

Specifically, the thesis develops a mathematical treatment of the heat transfer equation for a cylindrical geometry representing conditions occurring at the tribometer scale and derives consistent analytical and numerical solutions. These set a convenient modelling reference for the purposes of inverse analysis, based on experimental data obtained by ring-on-ring tribometer tests, which ultimately provide quantitative estimates of the physical parameters, useful for an accurate description of industrial production processes.

Extended summary

During hot deformation processes, tool surfaces experience severe frictional stresses and thermal fluxes. The present doctoral dissertation aims at developing a quantitative description of such phenomena, through an integrated experimental and modelling approach based on inverse analysis.

Dedicated experimental activities devoted to assess friction behavior under hot rolling conditions show that classical Coulomb's friction law may not represent the best description of interfacial phenomena. Indeed, during hot rolling, plastic deformation processes arise. Once the material undergoes plastic deformation, a linear proportionality relation between friction shear stress and contact pressure no longer holds. Therefore, a constant friction coefficient cannot fully explain the actual frictional stress trend. Since material properties are temperature dependent, and so is yield stress, a thorough thermal condition analysis must be performed, in order to characterize in detail the contact mechanical behavior. Heat fluxes to which the tool is subject to during hot processes depend on heat conduction, which in turn is a function of the surface state, the application of lubricants or the presence of surface oxides, as well as on specific contact conditions and temperature differences with the workpiece.

To assess quantitatively thermal fluxes under high contact pressures and temperature differences, a characterization procedure based on inverse analysis has been developed, to evaluate heat fluxes from sample surface temperature evolutions measured in specific tribological tests, performed with an innovative high temperature ring-on-ring tribometer implemented in an industrial setting. Indeed, conditions typical of real industrial production processes can be idealized in experimental setups that reproduce, as closer as possible, the hot

working conditions, such as in high-temperature ring-on-ring tribometer testing. Such experimental device and attached systematic experimental procedures and investigations allow for gathering conspicuous data, as truly representative of industrial hot rolling conditions. Long-run tests have been carried out under pure rolling (no relative sliding and no consequent frictional effects) whereby the surface temperature evolution due to the rotating contacts has been measured by a pyrometer.

Inverse analysis has required first the assembly of a robust mathematical model of the tribological test under target. A two-dimensional time-dependent analytical solution has been developed for the temperature distribution calculation in an infinite (solid and hollow) cylinder subjected to a thermal flux over a narrow surface arc segment. The solution relies on basics and research advances from the pertinent literature but develops a full, integrated approach that takes and analyses the process in subsequent steps, with different levels of complexity. The produced outcomes appear rather innovative, by themselves, in the specific scientific field and in the research theme under target. The analytical solution is consistently compared to Finite Element Method (FEM) modelling of the same ideal process, with comparisons in terms of effective representation and, most of all, of computational cost, which should be reduced to a minimum, given the target of the subsequent iterative inverse analysis. This solution has been then adapted to mimic the specific testing configuration conditions and further simplified to reduce the computational effort.

Given the availability of comprehensive sets of material data and robust modelling of the physical processes, inverse analysis arises as an effective, fundamental tool, in order to determine the values of the physical parameters that are truly representative of the exchange phenomena that are involved in hot rolling. Thus, the target here is that of identifying the values of the model parameters, based on data from experimental tests, specifically from ring-on-ring tribometer tests. Hence, an algorithm of inverse analysis has been implemented to evaluate heat fluxes and relevant modelling parameters, through the minimization of the discrepancies between measured experimental results and analytical numerical simulation outcomes. The

developed methodology allows to effectively estimate the heat fluxes between contact surfaces under operating conditions similar to those occurring in hot deformation industrial processes such as hot rolling.

In conclusion, in this dissertation a robust approach has been proposed to accurately quantify the characteristic parameters of heat flow occurring between tool and workpiece in a ring-on-ring tribometer, apt to reproduce hot working conditions typical of industrial hot rolling processes. In the current literature these parameters can be recorded as either very accurate but based on laboratory measurements taken under conditions that are really far away from industrial ones, or very rough, since they are depending on coarse measurements taken under industrial conditions. The proposed methodology aims at bridging this considerable gap. Since the detected frictional behavior under plant conditions appears to be effectively conditioned by local temperature variations in the contact zone, the work presented here appears as a decisive, fundamental step, in the quantitative characterization of contact phenomena in hot deformation processes, and in the detailed understanding of the mechanical contact conditions under hot rolling, with relevance in industrial contexts.

Acknowledge

Desidero ringraziare, innanzitutto, il prof. Egidio Rizzi per l'incoraggiamento ad affrontare questo ciclo di studi e per il sostegno che mi ha sempre assicurato. Ringrazio anche il prof. Daniele Dini e la Fondazione Cariplo per il supporto (accademico e finanziario) da loro ricevuto durante la breve, ma intensa, trasferta estera.

Desidero ringraziare, poi, il Centro R&D di TenarisDalmine nelle persone del dott. Mario Rossi, direttore del centro, e del dott. Ettore Anelli, principal scientist, per l'opportunità concessami. Voglio esprimere, inoltre, la mia personale riconoscenza a Adriano Tavasci che in questi quattro anni è stato maestro, consigliere e compagno di viaggio.

L'ultimo ringraziamento va, infine, alle mie famiglie: quella "vecchia" e quella "nuova". Sono grato alla mia "vecchia" famiglia per l'appoggio che mi ha sempre garantito durante tutto il percorso, di studi e non. Sono grato a quella "nuova" per lo stesso motivo…e per tutto il resto!

Index

Chapter 1. Introduction

The present work concerns a tribological investigation on the contact phenomena that arise in industrial hot working processes of steel production, with specific reference to hot rolling processes. The industrial need of parameters that control industrial production processes have stimulated several researches aimed at characterizing the most important phenomena, among which there appear the phenomena of energy transfer by contact, both mechanical and thermal. Starting from existing studies, new experimental and numerical methodologies have been developed here ,in order to reach accurate estimates of the parameters which describe such phenomena.

1.1. General framework of the present research

Nowadays, the knowledge of the parameters that control industrial production processes represents really a key factor for the companies' competitiveness. Indeed, only through this achievement it is possible to manage and, above all, to optimize the whole production cycle. However, the complexity of an industrial process and the absence of reliable data make the identification of these parameters particularly difficult to be realized in real industrial settings.

The present research focuses on the characterization of crucial parameters typical of hot deformation processes, in particular of hot rolling, in the production of seamless pipes. During a hot process, temperature is above the metal recrystallization temperature. In this way, during the processing, deformed grains recrystallize, thus maintaining an isotropic microstructure and preventing the metal from undergoing work hardening. A clear advantage of hot working is that the material keeps soft and ductile, which means that the workpiece can be formed at lower

forces and larger deformations than in cold working. However, this requires a large amount of energy to heat the material and the dimensions tolerance and surface finishing may end-up poorer than for cold working operations. Moreover, the working tools are subjected to strong thermal and mechanical stresses, which entail severe tool wear.

Instead, rolling is basically a metal forming process in which the metal stock is passed through one or more pairs of rotating (in opposite directions) cylinders, named rolls, to reduce the thickness and to make it uniform. Then, hot rolling is such a metal working process when it occurs at high temperature, where metal is soft and ductile. Hot rolling is a very important metal working condition used mainly for flat productions, as for metal sheets. However, hot rolled products can also be shaped as rods, wires, pipes or various profiles, such as beams and rails.

Although modern rolling plants are endowed with sophisticated measuring systems that allow to monitoring various aspects of the hot rolling process, the accuracy of the available data may not be entirely acceptable, from the point view of either phenomenological investigations or, in some cases, of industrial process control. This is due to the fact that industrial environments are affected by severe conditions in terms of ambient temperature, electromagnetic noise, etc., which do not allow to achieve reliable signals.

The present doctoral dissertation arises in such an industrial context and develops an innovative integrated methodology, based on ad-hoc laboratory measurements that allow both to analyze contact phenomena occurring during hot rolling and to achieve more accurate industrial parameter estimates, by a qualitative and quantitative description of the involved physical processes. To avoid data uncertainty given by rough and approximate industrial measurements, an innovative laboratory equipment apt to replicate in a controlled environment real working conditions has been designed and built in an industrial setting. Such experimental facility allows to investigate with great accuracy the contact conditions occurring between tool and workpiece during hot rolling. Hence, the focus of this thesis is on the characterization of the energy exchange, both mechanical and thermal, between tool and workpiece during a hot rolling

process, by means of an integrated experimental and analytical/numerical modelling approach, relying also on techniques of inverse analysis devoted to parameter identification.

The experimental activities have been carried-out in this new laboratory facility. This is, basically, a ring-on-ring tribometer capable to replicate, in a controlled setting, typical industrial contact conditions in terms of contact pressure and rolling speed (with potential relative sliding). Moreover, the tribometer is equipped with an induction heating system, for each ring-sample, to replicate and control temperatures that can be observed in the industrial plant.

Instead, the modelling approach consists of an analytical/numerical description of the experimental set-up, complemented by an inverse analysis procedure that allows to identify the unknown parameters governing the involved physical processes, specifically the various energy exchange phenomena.

1.2. Specific tribology context under target

The present dissertation context concerns a tribological investigation on the technical conditions that arise in industrial production processes of steel materials and components, with specific reference to hot rolling processes. Thereby, the understanding of physical phenomena and material behavior at the interface between working tool and workpiece material displays several significant implications in the industrial context, specifically in terms of effectiveness of the production process, maintaining costs and quality of the final product. This leads to a rising quest of analyzing such processes on a technical-scientific way, which opens-up true research scenarios in the present dedicated literature. In this thesis, the main phenomena under target are the characterization of friction and of heat transfer that occur for conditions typical of industrial production processes such as hot rolling of seamless steel pipes.

In hot rolling industrial processes, many contact phenomena of a different nature take place between tool and workpiece. These phenomena overlap and their global outcome can be detected through the measurement of friction behavior. By simply computing the ratio between

the tangential friction force and the normal force exchanged by two bodies, under different contact conditions, it is possible to analyze the effect of a few key process parameters on the contact mechanical behavior.

The present innovative experimental results that are achieved in the body of this work show the inadequacy of the so-called classical "Coulomb-Amonton's law of friction" to describe the contact mechanical properties by a constant friction coefficient, evaluated as the ratio above. The transition phase from Coulomb's law (effective at low normal loads) to the constant friction stress model (effective at high normal loads) was detected experimentally under hot rolling conditions of steel. Apparently, this is the first experimental confirmation in such a context. The experimental investigation develops a methodology apt to define a comprehensive friction law, and also to highlight some key variables, which can modify the mechanical interaction of the two bodies, such as sliding speed, surface oxidation, etc. Among these, the most important one is with no doubts temperature. In fact, temperature strongly influences the mechanical properties of the materials under contact and also promotes various chemical processes (such as surface oxidation, deterioration of any lubricants, etc.), thus resulting in wide changes of the mechanical response of the contact.

Therefore, a full understanding of the phenomena that occur at the workpiece/tool interface cannot disregard a complete analysis of the thermal fields and of the heat flows between tool and workpiece. For this reason, most of the present original research project focusses on the implementation of an integrated experimental and modelling approach devoted to characterize temperature and heat flow distributions during tribological tests representing true plant conditions. A dedicated experimental activity has been carried-out and a mathematical description of the ring-on-ring tribological test has been developed, by solving analytically the heat conduction equation in cylindrical coordinates.

In particular, this last modelization approach has led to a new two-dimensional time-dependent analytical solution which allows to compute the temperature distribution in an infinite cylinder subjected to a thermal flux over a narrow surface arc segment, with a

considerably lower computational time than for other solving approaches, for instance by the use of the Finite Element Method (FEM). The solution relies on basics and research advances from the pertinent literature but develops a full, integrated approach that takes and analyses the process in subsequent steps, with different levels of complexity, producing in the end outcomes that appear rather innovative, by themselves, in the specific scientific field. Subsequently, by integrating the experimental results with the analytical solution through an inverse analysis algorithm, heat fluxes have been characterized with higher accuracy than that currently available in the literature, with appropriate quantitative identification of key physical process parameters.

1.3. State of the art of the present research and statement of purpose

The increasingly widespread adoption of numerical models for industrial process description and simulation, optimization and control has pushed to achieve an increasing modelling detail, with consequent quest of characterization of reliable and accurate process parameters. Basically, in the present research work focus is made, among others, on two of these important parameters: the *Coefficient of Friction* (*CoF*) and the *Heat Transfer Coefficient* (*htc*).

Regarding the *CoF* and attached friction law, it has been noted above that Coulomb's law [27] cannot explain exhaustively the mechanical interaction between tool and workpiece during full hot rolling processes. However, despite that other more appropriate friction laws could be used in hot deformation process modelling (among these the law of Wanheim and Bay [97]), there are no reliable databases supplying real-valued parameters for such laws. This is due to the very nature of the friction phenomenon itself that is strongly influenced by many factors, some of which become quite difficult to be controlled in practice, especially at high temperatures. For this reason, while it may be feasible to identify a suitable friction law, it actually looks quite challenging to attribute to its various parameters correct

numerical values. In fact, they should be measured under conditions that run as closer as possible to those which actually occur during industrial hot rolling processes.

Similar arguments could be outlined for the determination of the *htc*. It may be straight-forward to introduce a mathematical law of the phenomenon, but it is actually harder to identify the law's characteristic parameters. However, given the great scientific and industrial interest on this topic, several evaluations of this parameter may be found in the literature [63]. Nevertheless, these estimates may be misleading due to the conditions in which they have been determined. In fact, in the available literature, there appear either evaluations that are very accurate but not very representative of industrial process conditions [66], or estimates based on rough industrial measurements [84], much less accurate and, especially, not easily applicable to different plant conditions, because of their specificity of the contact conditions in which they were determined.

In the present thesis, experimental activities aimed at assigning suitable values to the *CoF* in hot rolling conditions have shown that the contact mechanical behavior is strongly influenced by the thermal fields. By investigating the mechanical interaction between tool and workpiece, it has been found that the description of the mechanical behavior requires a full knowledge of the various heat flows. Hence, it is necessary to characterize the parameter describing this phenomenon, namely the *htc*. To determine with sufficient accuracy such a coefficient, a devoted integrated experimental and numerical methodology has been developed. By defining a methodology that would allow to replicate in the laboratory typical plant conditions, accurate estimates of the phenomena that occur in extreme industrial conditions can be achieved, by filling the gap that is currently detectable in the present literature.

1.4. Doctoral thesis structure

The present doctoral dissertation is organized as briefly reported below, with specific reference to the scientific and technical content of each chapter.

First of all, in Chapter 2, the state of the art concerning both mechanical and thermal contact phenomena is introduced. Starting from a brief historical point of view, the two aspects will be investigated in the industrial field of relevance, with particular attention to highlight the hot working conditions.

In Chapter 3, after introducing the innovative laboratory equipment (ring-on-ring tribometer), the experimental results concerning the friction coefficient behavior are presented under few rolling parameter variations. The *CoF* dependency on some most influential process parameters is investigated and, among these, the temperature effect is analyzed in much detail. So, in the same chapter, in light of the previous results, an experimental methodology is introduced to investigate thermal flows occurring at the interface.

These heat flows could be assessed quantitatively only by a parallel analytical/numerical analysis based on an mathematical description of the idealized tribometer thermal problem. The essential mathematical model is identified in the analytical solution of the heat conduction equation in cylindrical coordinates. So, an original analytical solution of the idealized experimental test is developed in Chapter 4. It is shown how the obtained solution computes the temperature distribution in much less computational time than that necessary for other approaches, like e.g. by FEM simulations, with, at the same time, no loss of accuracy. After introducing the idealized solution, further model developments are illustrated. So, radiation contributions, which are very important at high temperatures, convective cooling estimation, internal boundary condition approximation, etc. are considered and added to the mathematical model. These improvements are necessary to make the model, from one side, less idealized and as close as possible to the real configuration and, on the other side, to make it much competitive as possible, from the point of view of required computational time. This is due to the fact that

the analytical solution is then going to make reference for the objective function evaluation of the inverse analysis procedure to be implemented and run next.

Before illustrating the algorithm implemented for the heat flow identification, some essential concepts of the adopted inverse analysis procedure are introduced in Chapter 5, together with some basic notions behind the inverse analysis application to the present thermal problem. Then, the implemented optimization method is briefly described in terms of theoretical aspects of the chosen algorithm and of practical implementation in the computational environment.

Finally, in Chapter 6 results obtained by applying the algorithm of inverse analysis relying on the experimental results are presented, in terms of calibration of the *htc*. The capability to estimate radiation, convective and internal heat fluxes allows to keep the *htc* characterization detached from other phenomena, so as to achieve a clear value of this parameter. Moreover, particular attention is paid to the contact area estimation, for which a dedicated FEM model has been developed. Thanks to this model, the dependency on the contact pressure is investigated.

Chapter 7 summarizes all the work done and presented in this doctoral dissertation, focusing on methodological innovations introduced in both experimental and analytical/numerical approaches. The results obtained so far pave the way for further developments in various fields. So, in the end, some possible advances, endorsed by this work, are also outlined.

Lastly, in Appendix A the industrial context in which this work has been developed is presented. In Appendix B some fundamental aspects on the theory of heat conduction in solids are reported, in order to allow for a full understanding of the analytical solution developed in Chapter 4. With the same aim, in Appendix C the separation of variable method is presented. Finally, some basic properties of the Bessel functions, used extensively in the analytical solution, are presented as well in Appendix D.

Chapter 2. Fundamentals on key physical processes in thermo-tribological phenomena

The phenomena at the surfaces under tribological contact include the transfer of energy as the result of the actions of normal and shearing forces and of temperature differences. Effects of mechanical energy exchanges are described by means of dedicated friction models; instead, thermal energy exchanges are depicted by heat flows governed by specific parameters. In this chapter, historical approaches to these two energy transfer phenomena are briefly discussed.

2.1. Friction modelling: an introduction

The term "Tribology" was suggested in 1966 by Peter Jost in his milestone report [55] as a codified name to designate research and engineering applications related to describe phenomena of contact, friction and wear. The word is derived from the Greek word *tribos* meaning rubbing. So the literal translation would be "the science of rubbing".

The Jost Report [55] gave some economic considerations about tribology investigations. In 1966, it estimated an annual cost of £515 million that insufficient understanding or inappropriate applications of tribological principles may cause. In 1978, Czichos [28] assessed that nearly 30% of the energy generated in the industrialized world is consumed by friction and then the losses constitute a significant portion of the gross national product. Similarly, in 1982, Rabinowicz [77] evaluated that up to 6% of the gross national product was lost because of friction and wear. Further details of various cost estimates are available in Rabinowicz [78].

One may conclude that investments in research, concerning the fundamental mechanisms of tribology, may result in very good returns. Hence, the purpose of research in tribology is understandably the minimization and elimination of losses resulting from friction and wear at all levels of technology where the rubbing of surfaces is involved. Research in tribology leads to greater plant efficiency, better performance, fewer breakdowns, and significant savings.

2.1.1. Brief history of the physics of friction

Apart from the reference name, tribology is actually an ancient discipline. Tribological phenomena accompany the progress of humanity since its beginning: for instance, tribology is implied in the creation of fire through frictional heating; it is involved in the discovery of the wheel and plays a crucial role in the use of fluids to reduce frictional effects. However, the rational developments of this branch of knowledge took basically place starting from the contributions of *Leonardo da Vinci* during the Renaissance [76].

In his Codex-Madrid I, Leonardo da Vinci describes the ball-bearing, which he invented, and the composition of a low-friction alloy, as well as his experimental examinations of friction and wear phenomena. He was the first scientist and engineer who persistently and quantitatively attemped to formulate the laws of friction. He arrived at the main conclusion that can be summarized as two fundamental Laws of Friction [31]:

- The frictional force is proportional to the normal force, or load.
- The frictional force is independent of the contact surface area.

Leonardo da Vinci was the first to introduce the term Coefficient of Friction (*CoF*) and to experimentally determine it to a value of $1/4$.

These results were nearly forgotten at the time and only around 200 years later, were rediscovered in 1699 by the French physicist Guillaume Amontons [4]. The stated proportionality of the frictional force to the normal force is, therefore, known after as "Amontons' Law of Friction".

Leonard Euler occupied himself too with friction, from both the mathematical and experimental points of view [32]. He introduced the differentiation between static frictional forces and kinematic frictional forces and solved the problem of rope friction, probably the first contact problem to be analytically solved in history. He was the first to lay down the foundations of the mathematical way of dealing with the law of dry friction and, in this way, he promoted further developments. Moreover, he introduced the symbol μ to indicate the *CoF* as the ratio between frictional and normal forces. Euler worked with the idea that friction originates from the interlocking between small triangular irregularities and that the *CoF* is equal to the slope of these irregularities. This understanding survived, in different variations, for a hundred years and it is also adopted nowadays as the so-called "Tomlinson Model", in connection with friction at the atomic scale.

An outstanding and still relevant contribution to the examination of dry friction was achieved by French engineer *Charles Augustin Coulomb*. In fact, the law of dry friction actually carries on his name. Coulomb confirmed Amontons' results and established that, to a first order approximation, sliding friction is independent of the sliding speed. He undertook a very exact quantitative examination of dry friction lubrication, sliding speed, resting time for static friction, atmospheric humidity, and temperature. Only since the appearance of his book [27] the differentiation between kinematic and static friction could be quantitatively substantiated and established. Coulomb used the same idea of the origin of friction as that of Euler, but added another contribution to friction: adhesion. Furthermore, Coulomb established deviations from the known simple law of friction; for example, he found out that the static force grows with the amount of time along which the object has remained stationary. His book contained practically everything that originated the original branches of tribology.

Examinations of rolling friction have not played a prominent role in history as that of sliding friction, probably because rolling friction is much smaller in magnitude than sliding friction and, therefore, less annoying. The first ideas on the nature of rolling friction for rolling

on plastically deformable bodies, of which the most important elements are still considered to be correct, came from Robert Hooke [51]. Nevertheless, Osborne Reynolds [79] was the first to experimentally examine the details of the events happening in the contact area during rolling contact and established that on a driven wheel, there are always areas in which the two bodies are in no-slip contact and areas where slip takes place. It was the first attempt to put tribological contact under a magnifying glass and at the same time the end of the strict differentiation between static friction and kinematic friction. Reynolds accounted for the energy loss during rolling with the existence of partial sliding. A quantitative theory could later be achieved by Carter [20] in 1926 only after the foundations of contact mechanics were laid by Hertz, as discussed next.

Above all others, classical contact mechanics is associated with the name of Heinrich Hertz [48]. In 1882, Hertz solved the problem of contact between two elastic bodies with curved surfaces. Even today, this classical result forms a basis for contact mechanics. It took almost a century until Johnson, Kendall, and Roberts found a similar solution for adhesive contact ([54], JKR-Theory). This may come from the general observation that solid bodies do not adhere to each another. Only after the development of micro-technology, did engineers run into the problem of adhesion.

An advance in the understanding of contact mechanics, as well as of dry friction, in the middle of the twentieth century is bound to two further names: Bowden and Tabor [16]. They were the first researchers to advise on the importance of the roughness of the surfaces of the bodies in contact. Because of this roughness, the real contact area between the two bodies is typically orders of magnitude smaller than that of the apparent contact area. This understanding abruptly changed the direction of many tribological examinations and again brought about Coulomb's old idea of adhesion being a possible mechanism of friction. In 1950, Bowden and Tabor proposed a concept which suggested that the origin of sliding friction between clean, metallic surfaces is explained through the formation and shearing of cold weld junctions. According to this understanding, the *CoF* is approximately equal to the ratio of critical shear

stress to hardness and must be around 1/6 in isotropic, plastic materials. For many non-lubricated metallic pairings (e.g. steel with steel, steel with bronze, steel with iron, etc.), the *CoF* actually does take a value in the order of $\mu \simeq 0.17$.

The works of Bowden and Tabor triggered an entirely new line of theory of contact mechanics regarding rough surfaces. As a pioneering work on this subject, mention should be made to the works of Archard [5], who concluded that the contact area between rough elastic surfaces is approximately proportional to the normal force. Further important contributions were made by Greenwood and Williamson [42], Bush et al.[18], and Persson et al. [73]. The main result of these examinations was that the real contact areas of rough surfaces are approximately proportional to the normal force, while the conditions in individual micro-contacts (pressure, size of micro-contacts) depend only weakly on the normal force.

Contact mechanics definitely forms the foundations of today's understanding of frictional phenomena. In history, frictional phenomena were earlier and more fundamentally examined in comparison to pure contact mechanical aspects.

2.1.2. Friction modelling in hot working

The usual choice of friction coefficient modelling leads to the Coulomb-Amontons' law $\mu = \tau/p$, which expresses the *CoF* as the ratio between the interfacial shear stress τ and the contact pressure, or interfacial pressure p. However, sometimes this *CoF* may not be the best description of interfacial phenomena (Lenard [62]). For example, in hot metal working, the normal pressure p may increase significantly beyond the material flow strength. The interfacial shear stress τ may also increase but it cannot rise above the metal's yield strength in pure shear; this imbalance leads to unrepresentative ratios. The problem may be overcome instead by the use of Tresca's friction factor m. The friction factor m is defined as the ratio of the interfacial shear stress to the metal flow strength k in pure shear, $m = \tau/k$. Nevertheless, Coulomb's *CoF* is widely used and is also often adopted in the mathematical modeling. Neither the Coulomb-Amontons' model nor the constant friction model are fully comprehensive. Therefore, in the

literature, several approaches were proposed to bridge the gap between these two models. For instance, to model friction in metal working, Nadai [68] proposed a viscous slipping friction proportional to the relative slip velocity; instead, Orowan [70] dived the contact areas into two zones and used a different friction model in each of them: in one, sticking occurs (constant friction model); in the other, dry slipping occurs (Coulomb law) and so on.

In their works, Wanheim and Bay [95], [96] and [97] introduced a nonlinear continuous relationship between frictional and normal stresses. Applying the slip-line method for the analysis of plastic deformation of workpiece surface asperities in contact with a smooth tool surface, these authors proposed in [96] and [97] a general friction model, confirming that Coulomb friction is valid at low normal pressures, whereas the friction stress goes towards a constant value at high normal pressures. They proposed the following analytical expression for the friction stress:

$$\frac{\tau}{k} = \frac{\tau^*}{k}\frac{p/\sigma_y}{p^*/\sigma_y} \tag{2.1}$$

for $p \leq p^*$, and

$$\frac{\tau}{k} = \frac{\tau^*}{k} + \left(m - \frac{\tau^*}{k}\right)\left[1 - e^{\frac{(p^*/\sigma_y - p/\sigma_y)\cdot\tau^*/k}{(m-\tau^*/k)\cdot p^*/\sigma_y}}\right] \tag{2.2}$$

for $p > p^*$, where σ_y is the yield stress, $\frac{\tau}{k}$ and $\frac{p}{\sigma_y}$ are called the dimensionless friction stress and the dimensionless normal pressure, respectively. The limit of proportionality between friction stress and normal pressure (τ^*, p^*) is defined by [11]:

$$\frac{\tau^*}{k} = 1 - \sqrt{1-m} \tag{2.3}$$

and:

$$\frac{p^*}{\sigma_y} = \frac{1 + \frac{\pi}{2} + arccos\, m + \sqrt{1-m^2}}{\sqrt{3}\left(1+\sqrt{1-m}\right)} \tag{2.4}$$

The reliability of this approach for bulk metal forming was confirmed numerically by Petersen et al. [74]. This approach was applied also to model the pressure distribution in plate rolling and cross shear plate rolling processes (Christensen, Everfelt and Bay [23], Zhang and Bay [107]).

Moreover, there are different formulas available in the literature for the Coulombian *CoF* estimation in hot rolling conditions, which attempt to take into account the operating conditions such as temperature or sliding speed. However, these correlations are rather empirical and often based on not reliable data. Among available correlations, it is worthwhile to point-out Roberts's formula [80], which provides an increasing relation between *CoF* and temperature u (in °*C*):

$$\mu = 2.7 \cdot 10^4 \, u - 0.08 \qquad (2.5)$$

Geleji's formula, instead, indicates the opposite trend with respect to the influence of temperature [101]:

$$\mu = 1.05 - 0.0005 \, u - 0.056 \, v \qquad (2.6)$$

where u is the temperature in °*F* and v is the rolling velocity in *m/s*. The relation was obtained for steel rolls by applying an inverse method matching the measured and calculated roll forces. For doubled poured and cast rolls, the formula for the estimation of the *CoF* is slightly different:

$$\mu = 0.94 - 0.0005 \, u - 0.056 \, v \qquad (2.7)$$

and it changes again for ground steel rolls:

$$\mu = 0.82 - 0.0005 \, u - 0.056 v \qquad (2.8)$$

These relations, indicating a decreasing *CoF* with increasing temperature, are in accordance with the experimental results obtained by Rowe [82]:

$$\mu = 0.84 - 0.0004 \, u \qquad (2.9)$$

Eq. (2.9) was obtained for temperatures higher than 700 °C.

A comparison of the *CoF* obtained using formulas (2.5)-(2.9) indicates that such relations may provide large differences for different rolling temperatures and therefore may be not completely reliable.

2.2. Contact heat exchange phenomena: an introduction

Contact heat transfer is present at almost every contact between two surfaces. The transfer of thermal energy is of equal importance to the transfer of forces and thus it forms a significant branch of tribology (Lenard [61]). There is a broad variety of applications that have been investigated in the last 50 years or more.

2.2.1. A mechanism of contact heat transfer: Thermal Contact Conductance

Thermal contact conductance is the mechanism which is deputed to describe heat conduction between solid bodies under thermal contact. The thermal contact conductance coefficient, h_s, represents a property indicating the thermal conductivity, or the ability to conduct heat, between two bodies in contact.

Looking at the microscopic level, a surface that has undergone certain finishing operations is characterized by three properties: roughness, waviness and flatness. Among these, roughness is of most importance because it prevents perfect contact between two surfaces. That means that contact is only obtained at discrete points, separated by relatively large gaps. This not only reduces the actual contact area, but may also largely influence the total heat flow across the interface through the gases/fluids filling these gaps.

As stated by Madhusudana [63], the heat transfer through two bodies in contact may be considered to be composed only of three components:

- conduction though the actual contact spot;
- conduction through the interstitial medium, such as air;
- radiation.

The interfacial gap thickness, generally in the order of 1 μm, is too small and heat transfer by convection cannot take place. Radiation can be neglected, unless the temperature at the joint

is in excess of 300 °C, but it may also be significant if the temperature difference across the interface is large. It is often considered that the heat conduction through the actual contact spots is the only significant component. However, the area available for the flow through the interstitial gaps is frequently 2 to 4 orders of magnitude greater than that of the actual contact area [63]. Hence, the heat flow through the gaps cannot be neglected, especially if the solids are relatively poor conductors such as for stainless steel, or if the interface medium is a good conductor.

Thermal contact conductance, h, is defined as the ratio of the heat flux (Q/A) to the additional temperature drop (Δu) due to the presence of an imperfect joint (Holman [50]):

$$h = Q/(A \cdot \Delta u) \tag{2.10}$$

In Eq. (2.10), Q is the total heat flow and A is the nominal contact area.

Some researchers define the thermal contact resistance R that is simply the reciprocal of the thermal contact conductance:

$$R = 1/h = (A \cdot \Delta u)/Q \tag{2.11}$$

If it is possible to separate the heat flow through the solid spots, Q_s, from the heat flow through the fluid in the gaps Q_g, such that:

$$Q = Q_s + Q_g \tag{2.12}$$

Then, the solid spot conductance can be defined as:

$$h_s = Q_s/(A \cdot \Delta u) \tag{2.13}$$

and the gap fluid conductance as:

$$h_g = Q_g/(A \cdot \Delta u) \tag{2.14}$$

Then, form Eq. (2.10):

$$h = h_s + h_g \tag{2.15}$$

The heat flow through the solid spots Q_s is usually determined by conducting the heat transfer test under vacuum. Q_g is determined by conducting the test in the work environment and by taking the difference. However, it has been appreciated that the two flows are not

independent [63]. In fact, thermal contact conductance is a complicated phenomenon, influenced by many factors. Besides surface roughness and interstitial material, as previously discussed, the experience shows that thermal contact conductance is related to the apparent contact pressure (the real one depends on roughness) and/or to the hardness of the softer contacting material (Cooper et al. [26], Wusatowski [102]) and to the surface deformation (Williamson and Majumdar [100]).

An earlier calculation of the actual contact heat transfer was presented by Fenech and Rosenhow [33]. The first model considering heat flow through several contact spots due to surface roughness was proposed by Cooper et al. [26]. Instead, the first model considering elastic and plastic deformation of the surface peaks was proposed by Mikic [66]. Since then, numerous authors have developed contact models for specific applications, providing a huge amount of even more accurate estimations. However, only a few of them have considered high loads and high pressures. Before Fieberg and Kneer [35], validated models existed only for contact pressures up to 7 *MPa*. For this reason, these authors developed a new approach based on transient temperature measurements to characterize thermal contact conductance under contact pressures up to 70 *MPa* and temperatures up to 280 °*C*. Anyway, this work has shed light on the non-applicability of these methodologies in the characterization of industrial hot working conditions.

Thermal contact conductance is an important factor in a variety of applications, largely because many physical systems contain a mechanical combination of two materials. Some of the fields where the contact conductance is of importance are: in industry, in particular for nuclear reactor cooling, gas turbine cooling, internal combustion engines, heat exchangers and so on; in aeronautical engineering for hypersonic flight vehicles, thermal supervision of space vehicles; in electronics, where heat transfer is an area of great importance due the present trend toward microminiaturization and consequent increase in power densities (Madhusudana [63]).

2.2.2. Heat transfer in hot working processes

In hot deformation processes the thermal history of the workpiece has a profound influence on the final properties of the products, see [58]. There appears a strong industrial need for more accurate, predictive, computer-based models of these processes. However, these models are inadequate due to a coarse and sometime wrong definition of mechanical and thermal boundary conditions, namely friction and heat transfer respectively. In particular, heat conduction to the work rolls, as well as radiation to the environment, convection to descaling and backwash sprays have been considered to be the main modes of heat loss during hot strip rolling.

The complexity of the interface between tool and workpiece makes measurements very difficult. The direct measurement of heat transfer, and often also of friction, is rather impractical, for most industrial hot metal-forming operations, and even for many conducted in the laboratory. Due to such complications, heat exchange is not usually described through the thermal contact conductance that considered only the real fraction exchanged by contact, but by a less refined *Heat Transfer Coefficient* (*htc*) that includes thermal effects. Then the *htc* can be defined as:

$$htc = Q_c/(A_c \cdot \Delta u) \tag{2.16}$$

where Q_c is the total amount of heat transferred by contact, A_c the contact area and, finally, Δu is the temperature difference between the two surfaces. Thus, in the absence of detailed insight and with a lack of a fundamental understanding of the mechanisms of heat transfer at a moving interface, most modelers assume a simpler description, or an average value, of the *htc*.

In the past years, several efforts have been made to understand more about heat transfer phenomena during hot working processes, and in particular during hot rolling. For example, it has been observed that the contacting points between two surfaces serve as paths of lower resistance for heat flow, in comparison to adjacent regions where heat transfer occurs by conduction through air gaps (Samarasekera [84]). Based on experimental results, Devadas et al. [30] concluded that the variation of the *htc* with thickness reduction, rolling speed and lubrication observed through pilot mill tests on stainless steel could be explained on

the basis of the influence of these rolling parameters on the actual contact area. As expected, the interface heat transfer coefficient increases during rolling, because the real area of contact between two surfaces under applied load increases with higher pressure. The influence of other factors, such as roll reduction, rolling temperature, roll speed, roll and rolled material and their roughness, can be related to their effect on the roll pressure distribution through the roll gap. It has been found that the average *htc* is linearly related to the mean roll pressure (Chen et al. [22]). The relationship between *htc* and mean pressure can be used to determine the magnitude of the *htc* in industrial rolling, from an estimate of the rolling load. According to the estimation, the heat losses to the work rolls during rough rolling (i.e., shortly after the stock leaves the reheating furnace) can be more than 30%. This shows the significance of accurately characterizing the interface *htc* in the roll bite.

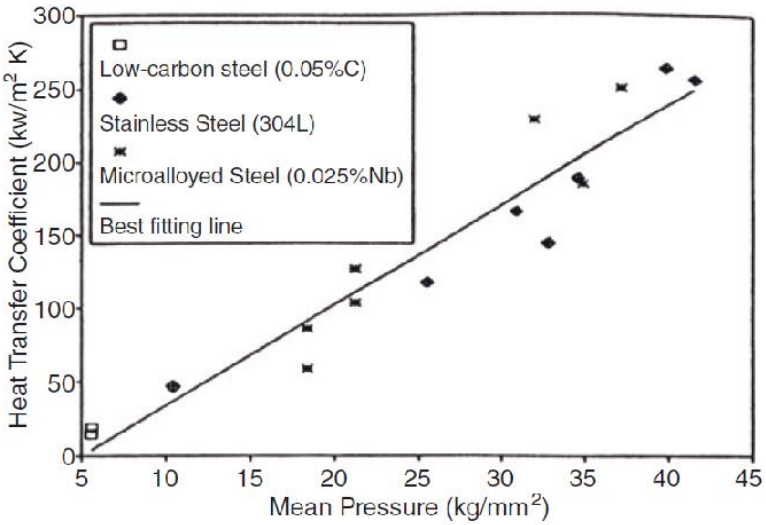

Figure 2.1: Influence of the mean roll pressure on the average heat transfer coefficient during hot rolling [22].

However, despite current efforts, the difficulties of making laboratory measurements, combined with the complexity of the tool-workpiece interface, result in a wide range of reported values of the *htc*, see e.g. Table 2-1 (Beynon [14]). In recent years, the increase of the available computing power has led to the development of numerical models that allow to predict temperature and thermal flow of a roll under working conditions. For instance, Guo [36] used a semi-analytical method involving Laplace and inverse transforms to pursue the unsteady

solution for typical boundary conditions. In order to optimize the geometry of the water spray of the cooling system, Saboonchi and Abbaspour [83] proposed a simplified model, by the Finite Difference Method (FDM), which computes the three-dimensional temperature field. The equation is computed along the circumferential direction with respect to time. Zhang et al. [105] proposed the FDM or the Finite Element Method (FEM) to predict the temperature field in the roll and the thermal crown, by neglecting the variations along the circumferential direction but by taking into account variations along the axis of the roll. Montmitonnet [67] also proposed a predictive FEM model of the whole rolling process, by coupling the strip and the roll thermal behaviors with iterative methods.

Reference	$\boldsymbol{htc}$ $\boldsymbol{[kW/m^2K]}$
Malinowski, Lenard and Davies (*1984*)	**2÷20**
Pietrzyk and Lenard (*1989*)	**5÷50**
Chen, Samarasekera and Hawbolt (*1993*)	**10÷260**
Stevens, Ivens and Harper (*1971*)	**18÷38**
Murata, Morise, Mitsutsuka, Haito, Kumatsu and Shida (*1984*)	**23÷82**
Sellars (*1985*)	**200**

Table 2-1: heat transfer coefficent between roll and rolled material for the hot rolling of steel, from Beynon [14].

The availability of complex models for the rolling process simulation provides the capability to achieve a more accurate evaluation of the *htc* by means of inverse analysis. In fact, the use of such solutions as objective function in dedicated inverse analysis algorithms allows to precisely characterize the *htc* related to the plant from which experimental data come from. Many inverse methods are based on matching the input (measurements) and output of the model equations. The least square method and the conjugate gradient method are often used towards this purpose. Huang et al. [52] proposed an unsteady-state inverse analysis based on the conjugate gradient method, to obtain the heat fluxes in the strip-roll arc of contact, by measuring

inside the roll body with a fully embedded local sensor. The iterative method consists in solving numerically the direct problem (or objective function) on each iteration, the sensitivity problem and the adjoin problem in minimizing the error between the estimated temperatures and the measured temperatures. Tseng et al. [91] proposed an inverse FEM assessment. The measurements are used to quantify the heat flux in the roll gap. The heat transfer coefficient in the spray portion was evaluated through an inverse heat conduction technique. Keanini [57] proposed three-dimensional inverse methods to evaluate the heat flux entering the roll, by measuring at several different locations. These contributions were based on the FDM or the FEM, with matrix forms and least square method. More recently, Chen and Yang [21] proposed a 2D steady approach based on the conjugate gradient technique. Since the computation times do not allow for a real time evaluation, the time dependence was neglected. Moreover, a recent two-dimensional semi-analytical inverse method adapted to rotating cylinders has been proposed and applied by Volle et al. [93] and Gradeck et al. [17]. This method is based on Fourier and Laplace transforms of the unsteady heat equation; then, the deconvolution is performed with a numerical algorithm. Minimization, between the measured and calculated temperatures, is performed with least square methods and regularized with classical techniques. Very recently Weisz-Patrault et al. [94] published a fully analytical 2D (radial and circumferential directions) inverse method, by considering only one thermocouple embedded inside the roll, and dealt with the rolling conditions. The method was very fast and relied on the 2D unsteady heat equation.

Although these methods allow to achieve more refined parameters, these are still subjected to measurement errors typical of the plant and, above all, these approaches do not “guarantee” a “general” result. In fact, this kind of parameter characterization is performed on data coming from a specific mill, or pilot mill, and so, the results work only for the specific plant from which experimental data come from. Moreover, since they use a (pilot) mill instead of a laboratory equipment, this does not allow for an influence analysis on most contact parameters.

Chapter 3. Experimental approach at the tribometer scale

An innovative high-temperature ring-on-ring tribometer has been specifically designed and assembled in order to analyze thermo-mechanical phenomena occurring during hot processes. Thermal and mechanical behavior are analyzed on this device through two dedicated kinds of tribological tests. In this section, after a brief explanation of the laboratory equipment, an example of the mechanical interaction analysis is provided. This allows, from one side, to highlight the device's capabilities and, on the other side, to introduce the impact of thermal phenomena in the surface interactions. Then, the experimental methodology developed to analyze the thermal effect occurring at the contact is presented.

3.1. Ring-on-ring implemented laboratory facilities

Aiming at evaluating friction coefficient and heat transfer coefficient trends at variable loading conditions, experiments were run on a newly-assembled industrial tribometer, designed on purpose as a pilot plant towards assessing wear and friction behaviour of tools under real hot rolling contact conditions. In particular, high temperature tests were carried-out with a Ring-on-Ring testing configuration, as schematically illustrated in Figure 3.1.

A sample, which is simply a ring or a disc, representing the hot material is mounted on an axis; instead, samples representing the working tool, as a piercing plug or mandrel, are mounted on the other axis. Each axis is driven by a motor in order to achieve a sliding speed from 0 *m/s*, which is equivalent to a pure rolling condition, up to 5 *m/s*, so as to scan the entire industrial range.

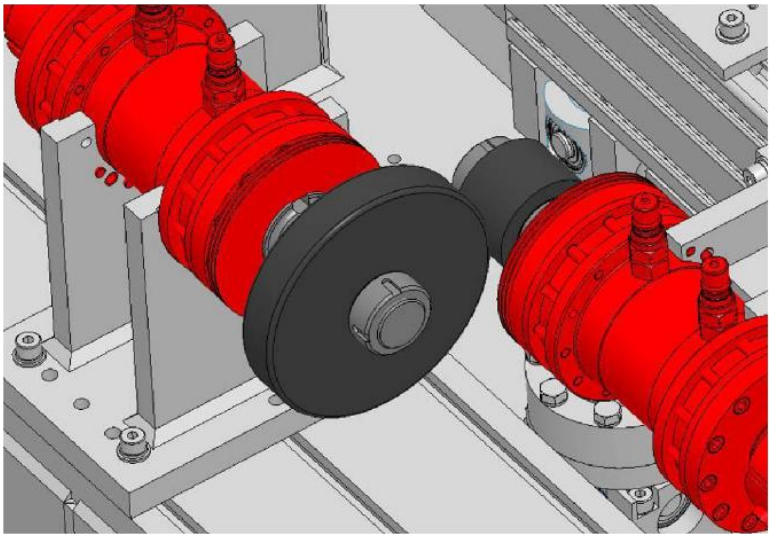

Figure 3.1: Ring-on-ring configuration for tribological testing at high temperature [88].

Samples are put in contact through a pneumatic cylinder able to reach Normal Loads up to 7 *kN*. That allows to reach the yield condition in the contact area close to the contact conditions occurring during hot deformation processes. To replicate plant conditions as closer as possible, the device is equipped with an induction heater for each sample, regulated by a closed loop control based on pyrometer measurements, in order to measure and, possibly, to control the samples' thermal cycle. The main induction heaters can heat the sample up to 1200 °*C*. Moreover, in order to reproduce the tools thermal cycle accurately, this machine is equipped with a cooling system composed by nozzles able to spray both water and compressed air directly on the samples' surface.

Friction is measured through signals coming from load cells that constitute also the support structure for one of the two samples. These cells measure the loads applied and exchanged between the samples in contact. In particular, they measure the applied normal load and the tangential one but also verify any misalignment between the samples in contact.

3.2. Test design and set-up

The ad-hoc designed tribometer is a versatile apparatus allowing to analyze many different phenomena occurring during hot working processes. Each phenomenon requires a specific test

design in order to highlight the most relevant factors affecting the phenomenon under target. In this work, an experimental method was tailored to assess friction coefficient measurements for the case of piercing of hot steel billets by means of plugs in seamless pipe production (presented in [88]). The achieved experimental results show that frictional behavior is strongly influenced by temperature. So, a second methodology was tailored to assess the thermal condition. In particular, this methodology focuses on the characterization of the so-called heat-transfer coefficient under high temperature and severe contact pressure conditions (presented in [89]).

3.2.1. Friction behavior in the piercing process

Manufacturing of seamless pipes through the well-known piercing process (also named Mannesmann process) is performed by feeding a steel billet into a piercer, thus generating a hollow through the use of piercing plugs (further details about seamless pipes manufacturing can be found in Appendix A). During hot piercing, plugs undergo severe thermo-mechanical working conditions at the surface, leading to exceed the yield strength, with consequent onset of plastic deformation. Under these conditions, plug wear is severe and the tool profile rapidly evolves into shapes that can no longer withstand the piercing process, with consequent strong reduction of process efficiency and limits in the production. The piercing time required to achieve the critical working conditions represents therefore on upper limit, beyond which the steel plugs show a reduced service life.

To identify the most impacting parameters which affect the plug working conditions, mechanical energy transfers between plug and pierced material were analyzed in terms of frictional behavior. In particular, the case of plugs coated by an oxide layer were considered. During hot working, oxide acts as a natural lubricant and also provides a thermal barrier, by protecting the substrate from overheating due to both friction work and heat transfer with the hot billet.

3.2.1.1. Experimental procedure

To investigate the piercing condition, a devoted test procedure was setup. Ring-shaped samples of 80 *mm* diameter, which were representing the plug in the piercing process, were cyclically put in contact under sliding conditions against a steel ring of 140 *mm* diameter, induction heated to about 1100 °C, representing the steel billet. Aiming at being representative of true industrial tribological couplings between piercing plug and hot billet, samples were machined directly from steel plugs and, prior of being tested, subjected to oxidation treatments in the same industrial furnaces where industrial piercing plugs are truly treated. About the billet material, two steels used for seamless pipe production were selected, thus reproducing two typical industrial piercing conditions. The rings were machined from bars of carbon steel (0.40%C, called C40) on one side and high-alloyed steel (ASTM A335 P91) on the other side.

Normal load was applied by a pneumatic piston, ranging from 0.5 *kN* to 3 *kN*. Rotation speeds were tuned in the attempt of get sliding speeds of 0.3 *m/s*, 0.9 *m/s* and 2.7 *m/s*, thus to scan possible hot contact conditions during the piercing process. During the time contact with the other ring, the temperature of the sample representing the steel rose from room temperature up to about 900 °C. Its surface temperature was measured in the middle of the specimen width through a pyrometer whose emissivity ε was set to a constant value of 0.75. At the end of each contact step, which lasts 180 *s*, the sample representing the plug was water cooled, as it occurs in the industrial process. Five working cycles were repeated for each testing condition.

Experimental friction coefficients were calculated by the ratio between the measured frictional force T and the applied normal load N, as recorded along the contact phase:

$$\mu_{exp} = \frac{T}{N} \qquad (3.1)$$

Temperatures of the wearable sample, as well as chemical composition of the counterbody and relative sliding speed, were thus taken into account to assess the behaviour of the frictional stresses which the plug undergoes during the piercing process.

3.2.2. Thermal phenomena in hot rolling

A different testing design was needed for the analysis of thermal phenomena occurring during hot deformation processes. The methodology developed to investigate heat transfer by contact consisted, basically, in a controlled contact between a disc kept at a constant temperature (hot disc) and another disc whose temperature is only measured (cold disc). The contact was hold in the absence of friction. So, tests were carried out at a zero slide/roll ratio, corresponding to pure rolling conditions. During the test, cold disc temperature rises up due to heat transferred by contact and to the other thermal contributions, like convection or radiation. Long-runs were needed to appreciate significant temperature variations.

Two discs of carbon steel (0.40% of carbon) were employed. Their dimensions were: 120 *mm* diameter and 20 *mm* wide (hot disc); 50 *mm* diameter and 34 *mm* wide (cold disc). All specimens presented a surface finishing from smooth lathe machining. Likewise for the contact duration, the cold disc dimensions were chosen to achieve an appreciable surface temperature increase under the test conditions.

Essentially, tests were carried out as follows. Initially, the rotating discs were put very close (but not in contact) and heated up separately and in the absence of contact, to target surface temperatures which were different for the hot disc and for the cold disc, respectively. This step duration was enough to let both samples to achieve a steady state condition of temperature distribution. Once the steady state temperature was approached, samples were put in contact under the normal load and the test was run for 1500 seconds. At this stage, only the main induction heater was switched on, to guarantee a constant surface temperature for the hot disc during all the contact time, whereas the second induction heater was turned off and the surface temperature evolution was recorded for the cold disc. Under these working conditions, the temperature profile of the cold disc evolved due to the heat flux at the contact region, the radiation from the hot disc, as well as the radiation and convection in air. The induction heater was excluded to gain more sensitivity towards these variables (uncontrolled fluctuations in

power supply could be as relevant as the heat flux). During the contact step, surface temperature evolution due to the rotating contacts was measured at the surface, in the middle of the specimen width, using a pyrometer located at 90° from the contact region (Figure 3.2). The pyrometer provides a stable data acquisition from 80 °C to 600 °C. The emissivity was set to a constant value of 0.75, after comparison with thermocouple measurements.

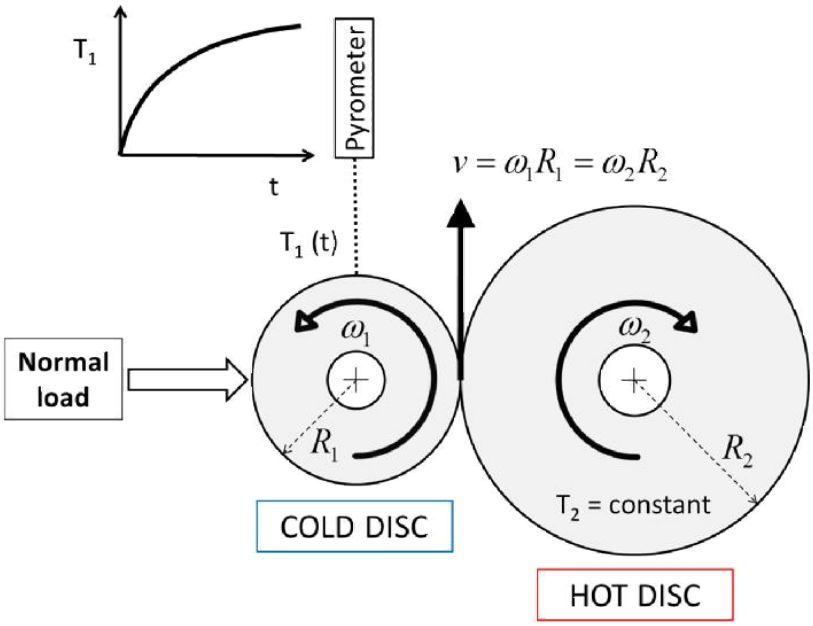

Figure 3.2: Schematic of the testing configuration and temperature measurement.

3.3. Experimental results

Experimental results from the previous two methodologies are now presented. Results concerning friction in the piercing process are briefly discussed to highlight the great influence of temperature in the frictional behavior.

3.3.1. Coefficient of Friction in the piercing process

The Coefficient of Friction (*CoF*) has been analyzed from different points of view. In particular, the effects of relative sliding speed, temperature of the sample, material coupling, as well as normal load were taken into account, to assess the behaviour of the frictional stresses during the piercing process.

3.3.1.1. Sliding speed effect on friction

The effect of the sliding speed was investigated. For this purpose, the friction coefficient μ_{exp} was evaluated at the beginning of the contact phase with the low carbon steel C40 (run-in condition, i.e. at relatively low temperature) and at the end (steady-state condition, i.e. at high temperature) at different counterbody temperatures.

According to [78], the friction coefficient decreases when relative motion increases (Figure 3.3). This means that during piercing the local friction conditions are different, as the sliding speed between the plug and the billet material changes along the longitudinal and transverse plug profiles. Also, it represents a first indication that Coulombian friction law is not able to model the friction behaviour during hot working processes.

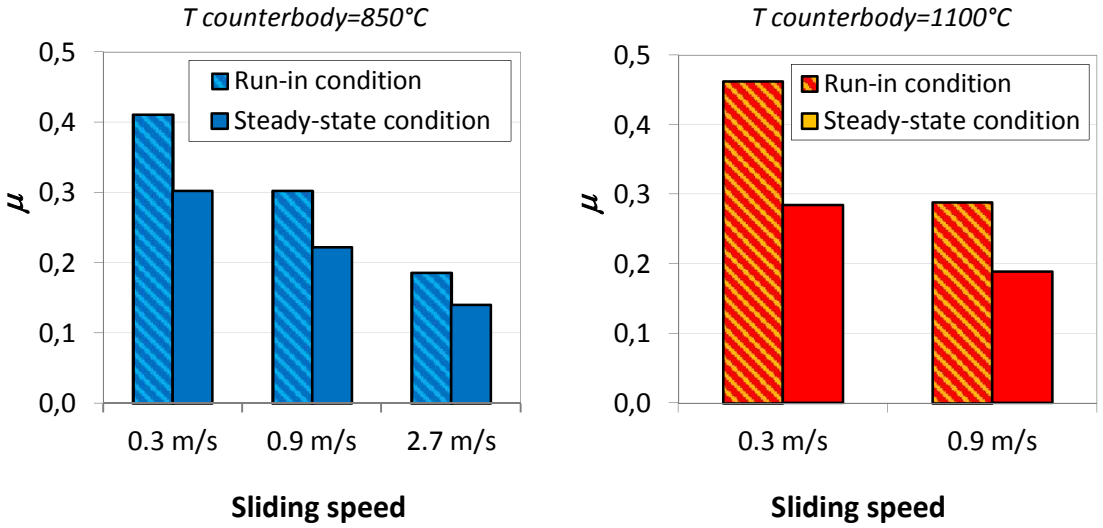

Figure 3.3: Friction coefficient estimates at different sliding speeds and at different counterbody temperatures.

Moreover, moving from the run-in condition to the steady-state condition, a further reduction of the friction coefficient is detected, meanwhile a temperature increase is observed. In the same way, at a higher counterbody temperature, a lower friction coefficient can be observed. So, this drop in friction seems to occur as temperature increases. The further analyses described in the next Sections could help to better understand this phenomenon.

3.3.1.2. Surface temperature effect on friction

In Figure 3.4, two examples of friction coefficient trends along the contact time window are plotted for the full time history, by distinguishing the contact with the high alloy steel P91 at 1100 °C and with the low carbon steel C40 at 1100 °C. The lubricant effect of the surface oxide was evaluated for 0.9 *m/s* sliding speed and by imposing the same normal load and the thermal cycle.

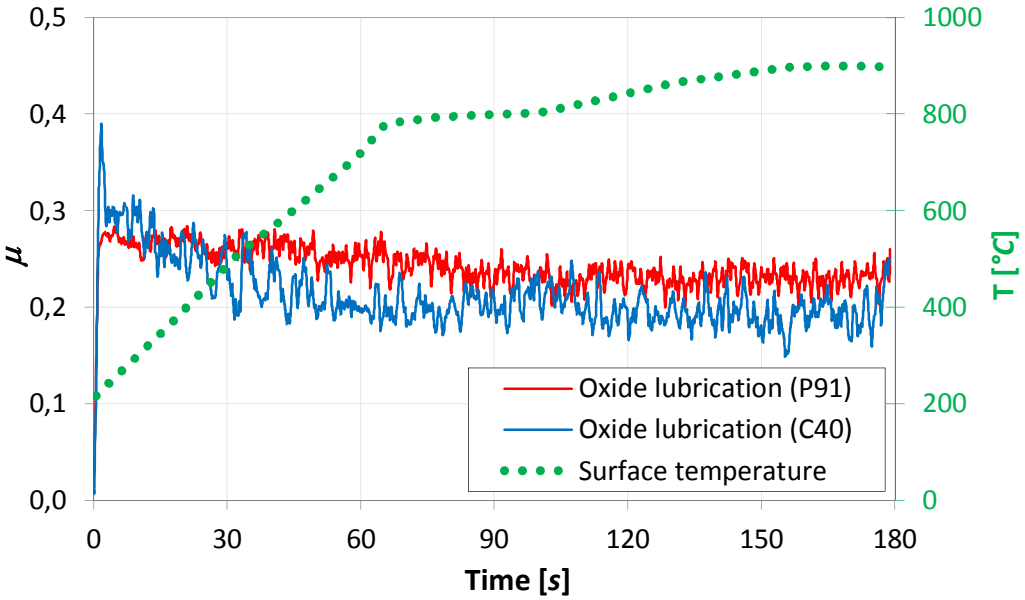

Figure 3.4: Friction coefficient trend and temperature variation along the contact time window occurring on the surface of the plug sample.

As seen in the previous section, moving from the run-in condition to the steady-state condition, a decrease of friction is detected in both cases, at the increasing of the sample surface temperature. This decrease appears more evident for the carbon steel and this could be due to the fact that at high temperature, low carbon steel is more predisposed to promote chemical reactions whose product maybe acting as a lubricant.

Another hypothesis is that, for temperature increases, mechanical properties of the low carbon steel (in particular, yield strength) decrease more quickly than properties of P91. In any case, these assumptions must be further investigated.

3.3.1.3. Effect of material coupling on friction

For the same plug material, friction coefficients were measured for two counterbody steels: C40 and P91 at 0.9 *m/s* sliding speed.

Moving from C40 to P91 led to an average increase of 11% in the estimate of the Coulombian friction coefficient, independently on the normal applied load, as shown in Figure 3.5.

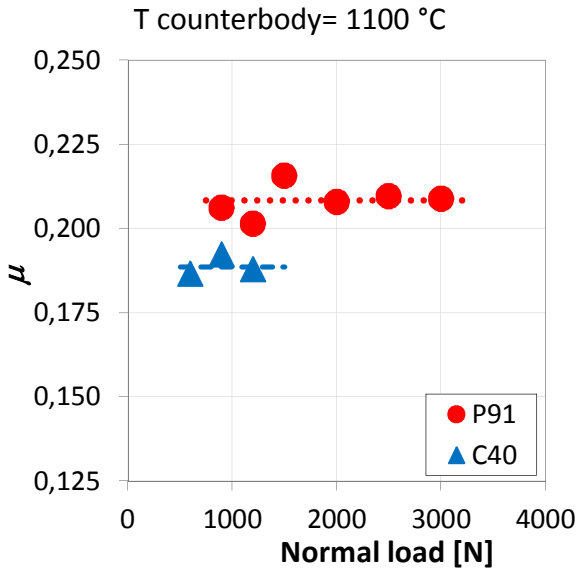

Figure 3.5: Measured friction coefficients for two billet materials (C40 vs. P91).

Looking at the plug sample surface at the end of each test, it is clear that the carbon steel appears to be more prone to generate a layer of material transferred to the surface of the plug sample. This rapidly oxidizes and continuously grows, until a steady-state condition of material loss (by means of wear) and regeneration (by means of oxidation) is stabilized. Figure 3.6 shows an example of the material transferred from the C40 counterbody to the wearable plug sample surface.

Increasing the normal load, transferred material phenomena are promoted and, increasing the number of testing cycles, a continuous layer is formed. However, being the friction coefficient scattering within the five working cycles of each test quite narrow for all the testing conditions, it is possible to state that friction work is dependent on the presence of an oxide

layer, but it is not influenced by the thickness of that layer, since oxide layers keep on growing during five testing cycles.

Hence, the frictional behavior depends on the oxidation rate occurring on the transferred material from the counterbody to the plug sample. This behavior can be reasonably different using high chromium steel (as in the case of grade P91), instead of very low chromium steel (as in the case of grade C40). Obviously, the oxidation process is always facilitated by the high temperatures.

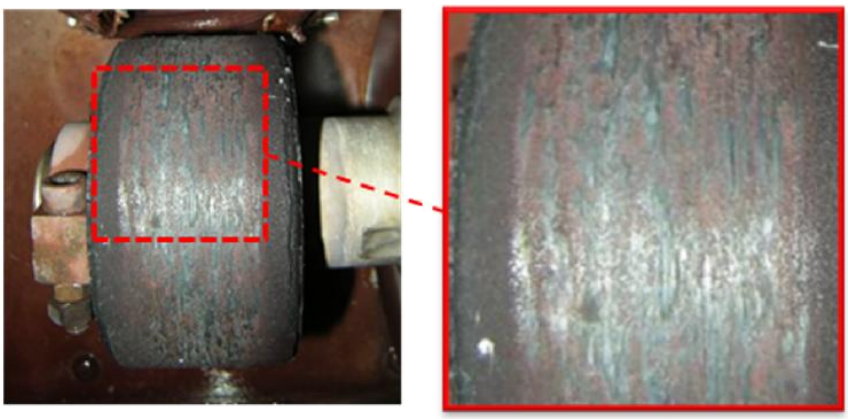

Figure 3.6: Transferred material from the 0.40%C steel counterbody to the wearable sample.

3.3.1.4. Frictional vs. normal force measurements

In Section 3.3.1.2, two assumptions were made regarding the friction decrease at the increasing of sample surface temperature. One was proven in the previous section. The other was not refuted yet. Indeed, the previous test were performed under elastic contact conditions; no results under plastic contact conditions were given yet. In order to verify also the second hypothesis, other tests were performed, then, applying normal loads such as to induce plastic deformation.

By assessing the tangential forces versus applied normal load during the steady-state regime, friction coefficient values, obtained according to the Coulombian law expressed in Eq. (3.1), were determined for the oxidized plug sample against the carbon steel sample at high temperature.

Experimental data (Figure 3.7) clearly show that, when the limit of proportionality between the frictional force and the normal one is overcome, a decreasing trend of the measured friction coefficient versus normal load is observed. In this case, the counterbody samples underwent macroscopic surface flow.

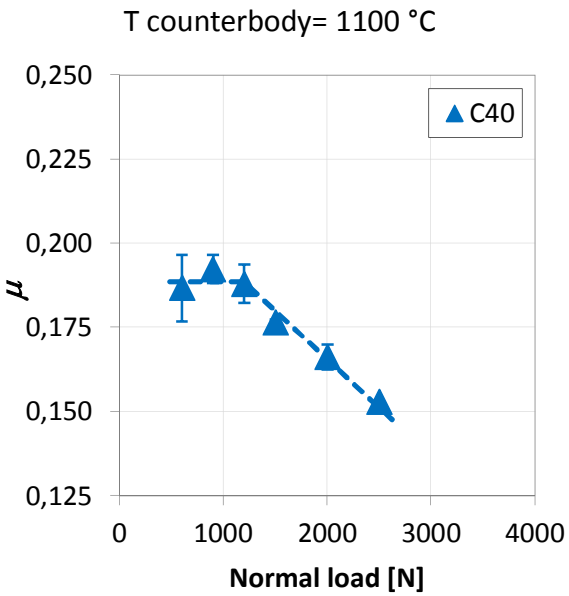

Figure 3.7: Measured friction coefficient as a function of normal load.

The region of smooth transition from the constant friction stress towards linear trend was further investigated by comparison with the high chromium steel behavior under the same testing condition. Instead of referring to normal load and friction coefficient, tests results were treated in terms of stresses, namely contact pressure p and tangential stress τ. These were assessed as the ratio between normal load and tangential load, respectively, and the Hertzian estimation of the contact area. Data were then normalized to the C40 limit frictional stress τ_0 and contact pressure p_0, beyond which τ and p are no longer proportional.

Figure 3.8 shows the change of the friction stress τ when normal pressure p is increased for both C40 and P91 samples. Being carbon steel C40 less resistant than high-alloyed P91 steel, the condition of deviation from proportionality between the frictional stress and the contact pressure due to the onset of material plastic deformation occurs at a lower value of contact pressure for steel C40, and this can be detected clearly. Moreover, it was verified that the

Wanheim-Bay model (see Eq. (2.1) and (2.2)), which takes into account the friction factor m, (in this case, m is equal to *0.776*) fits well the experimental data (Figure 3.8), confirming that the decreasing trend of the experimental friction coefficient, visible in Figure 3.7, is due to the onset of plastic deformation during contact. Being the friction factor a property of tribological coupling, the friction factor m, as stated in the mathematical model adopted for the experimental data elaboration, is strongly affected by the material elasto-plastic transition which, in turn, deeply depends on the material temperature, as shown for example in Figure 3.10. Hence, temperature could also affect the frictional behaviour, altering the mechanical material properties.

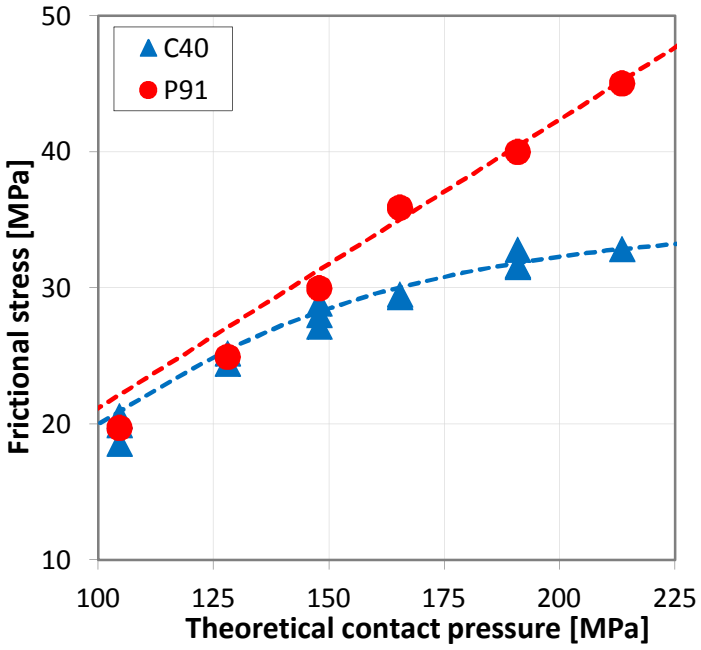

Figure 3.8: Frictional behaviour under hot piercing conditions: experimental data vs. best fit using the Wanheim-Bay model.

Finally, it was shown once again that the Coulombian friction law does not appear suitable for hot working friction modelling. Indeed, during hot working processes, the material plastic condition is generally reached and such condition is strongly influenced by the high temperatures typical of these processes.

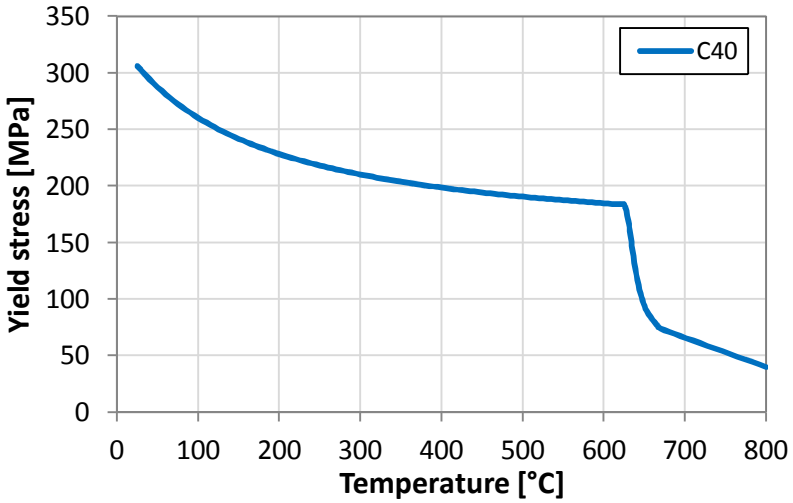

Figure 3.9: Yield stress trend of C40 steel as a function of temperature.

3.3.1.5. Considerations on the experimental results

Results presented in the previous sections show how temperature is able to affect frictional behaviour. Indeed, the surface temperature can promote chemical reactions or material surface modifications, which can modify significantly the tribological behaviour, as shown in Section 3.3.1.2. On the other hand, material properties are strongly influenced by temperature, so any change in the surface temperature can lead to notable alterations in the mechanical force transfers, namely in friction, as explained in Section 3.3.1.4. Without a deep knowledge of the interface thermal conditions, it looks quite impossible to understand which is the predominant effect due to the temperature increase.

Referring to interface thermal conditions, it is important to mention that surface temperature is not uniform during the contact between bodies. Indeed, in the contact area temperature rises up due to the heat generated by friction and/or to the heat transfer provided by the thermal gradient between the two bodies in contact. This temperature increase is very intense and also it is a very localized and fast phenomenon. It was studied for the first time by Block [15] who introduced, then, the concept of "*flash temperature*", namely the sharp temperature rise that takes place at the interface between two rubbing solids upon motion. Hence, to understand the frictional behaviour detected in any tribological test, it is fundamental

to know in detail the thermal phenomena occurring during contact. A comprehensive knowledge of the thermal conditions in the contact zone could help to recognize which phenomenon is dominating the force exchange. For this purpose, a devoted experimental approach was defined. As a first stage of the study, only heat transfer by contact is taken into account (i.e. heat generated by friction is not considered). Anyway, the approach could be easily extended to analyse also all thermal phenomena occurring during contact.

3.3.2. Heat transfer coefficient

According to the experimental procedure presented in Section 3.2.2, measurements of the surface temperature evolution during the contact step are shown in Figure 3.10, for the investigated cases reported in Table 3-1.

Case	Initial temperature		Initial temperature difference	Normal Load
	Hot disc	Cold disc		
1	400 °C	~ 180 °C	~ 220 °C	500 N
2				1000 N
3				1500 N
4				2000 N
5				2500 N
6				3000 N
7	600 °C	~ 290 °C	~ 310 °C	500 N
8				1000 N
9				1500 N
10				2000 N
11				2500 N
12				3000 N
13	800 °C	~ 390 °C	~ 410 °C	500 N
14				1000 N
15				1500 N
16				2000 N
17				2500 N

Table 3-1: Test conditions.

Previous results are summarized in Figure 3.11, where the temperature difference between the beginning and the end of the test for the cold disc is plotted as a function of the different test conditions. The graph clearly shows how by increasing the normal load, the temperature

difference raises. Also, hot disc temperature affects cold disc temperature increase; however, its contribution appears to be less impacting at higher temperature.

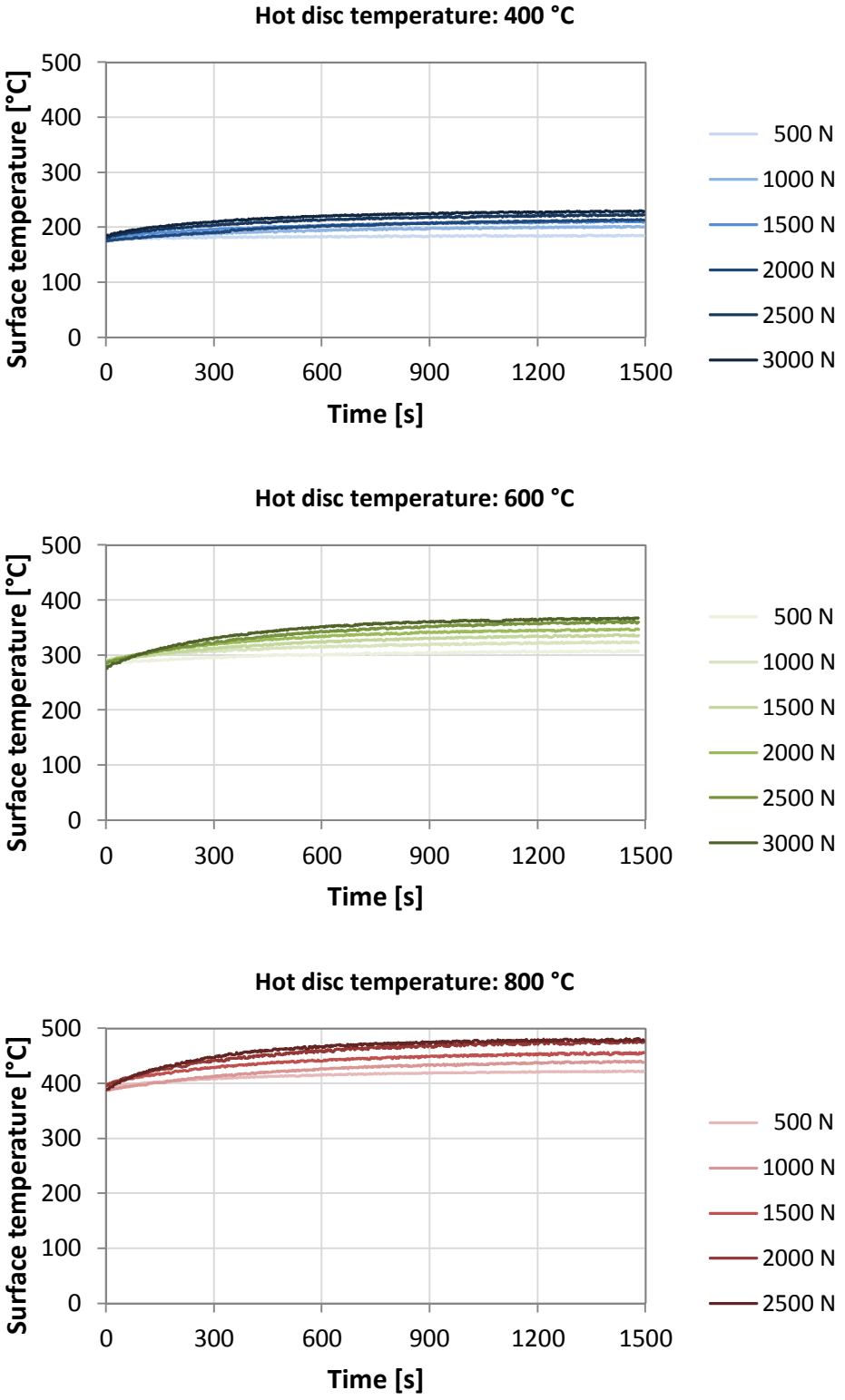

Figure 3.10: Experimental temperature increase evolution for different test conditions.

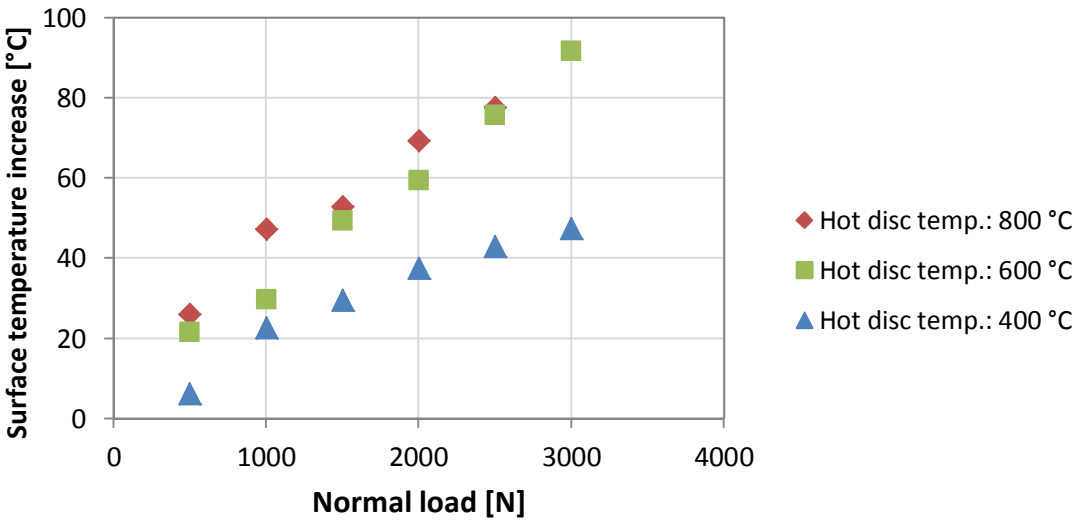

Figure 3.11: Experimental temperature increase during the tests for different testing conditions.

During tests, the environmental conditions reported in Table 3-2 were detected. These data are useful to characterize the general thermal condition to which the cold disc is subjected to during a test.

	Hot disc temperature		
	400 °C	***600 °C***	***800 °C***
Air temperature	60 °C	70 °C	130 °C
Room temperature	75 °C	80 °C	145 °C

Table 3-2: Environmental conditions.

From the curves in Figure 3.10 and the other information, it is evident that it is not possible to extract directly a parameter able to describe the contact thermal behaviour. Indeed, the experimental results are affected by different phenomena (for instance heat conduction or heat transfer by radiation or convection and so on) whose effects on the temperature increase shall be recognized. So, in order to characterize a significant parameter for the heat transfer during contact, namely the so-called heat transfer coefficient, a complete inverse analysis procedure shall be implemented (see Chapter 5). In turn, this procedure requires a mathematical description of the experimental test (see Chapter 4). These two mathematical tools are extensively described in the next chapters of the thesis.

3.3.2.1. Additional investigations

Since the experimental campaign presented above allows to analyse the surface temperature under different conditions, but does not provide information about the temperature gradient along the radius, additional tests could help in understanding more deeply the thermal phenomena which the sample undergoes during contact. In particular, previous tests did not examine the heat transfer between sample and its spindle. For this reason, a further simple test was performed, in order to detect the magnitude of the heat transfer on the hollow sample. By means of the induction heater, the disc was heated under controlled conditions. While the sample was heated up, both the disc surface temperature and the spindle temperature were measured. As shown in Figure 3.12, the results of this test point out a similar trend in the temperature increase. In details, the temperature difference between outer and inner surface appears to be constant all along the test. This means that the heat transfer from the disc to its spindle can be considered as a constant heat flow during the test. Moreover, its value could be very low due to the fact that the temperature difference between the spindle and the internal surface of the disc could be low since the spindle temperature increase appears very similar to that of the disc.

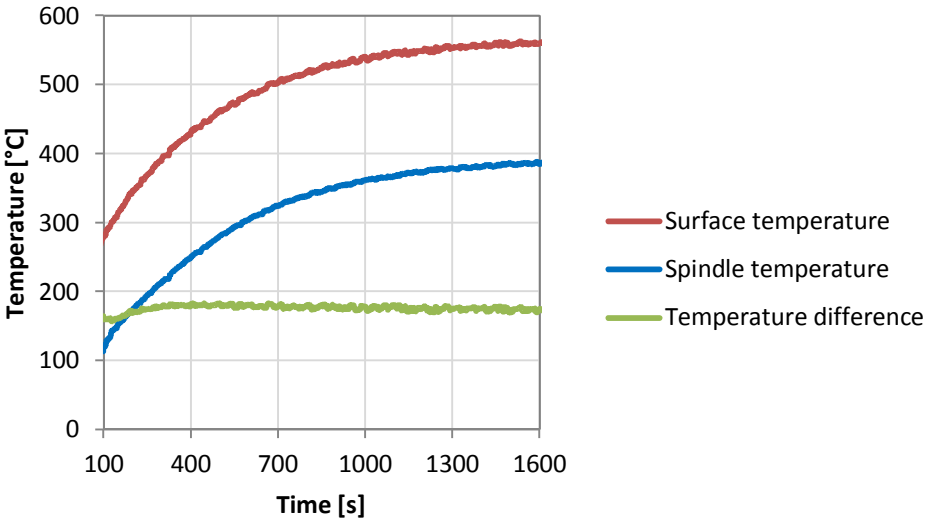

Figure 3.12: Experimental surface temperature and shaft temperature.

Chapter 4. Analytical and numerical modelling of heat transfer phenomena

The scheduled inverse analysis requires a consistent mathematical description of the phenomena occurring in the experimental configuration. In order to achieve solutions by inverse analysis in reasonable computational time through effective models, an approximation of a three-dimensional time-dependent analytical solution for the temperature distribution calculation is developed to mimic the specific testing configuration.

4.1. Statement of the thermal problem

Given the testing procedure and the temperature measurement methodology, the present mathematical model solved the heat conduction problem in cylindrical coordinates, whereby the contact heat flux is evaluated by focusing on the surface temperature variation in the cold disc, namely in a hollow cylindrical body. The mathematical solution has to be outlined by taking into account the heat transfer due to conduction, convection and radiation (at the present high test temperatures the last contribution cannot be neglected). In particular, the external surface undergoes concentrated thermal flux due to contact with the hot disc on a narrow surface arc segment and radiation from the hot disc, according to the so-called view factor (namely, the fraction of the radiation which leaves a surface and strikes another surface), as well as cooling in the air by convection and radiation. The internal surface of the cold disk is subjected only to heat exchange with the driven spindle by conduction.

In order to achieve effective models that allow for solutions by inverse analysis in a reasonable computational time, an analytical solution has been specifically developed. The real three-dimensional problem can be greatly simplified, based on the assumption that the sample can be considered as infinitely long (two-dimensional approximation). So, a two-dimensional time-dependent solution for the heat conduction problem applied to a rotating hollow cylinder subjected to concentrated heat fluxes is derived here.

4.2. State of the art on the analytical modelling

Many tribological test conditions and industrial applications involve rotating disks subjected to concentrated heating and/or convective cooling over their surfaces. The arising temperature distribution is targeted for the solution of the associated heat problem. Main reference information on the fundamentals of the treatment of heat transfer phenomena is accessible in several books, for instance, concerning specifically the developments under target here, in [1], [45] and [98].

In the literature, it is possible to find two main tackling approaches: the first one provides an analytical transient solution for a hollow cylinder heated and cooled uniformly along its boundaries (time dependent axis symmetric solution that is not dependent on the angular coordinate), see [19], [24] and [45]; the second one derives an analytical quasi steady-state solution for a rotating disk heated by a stationary concentrated heat source (time independent solution that depends on the angular coordinate), see [3], [8], [29], [37], [38], [39], [46], [59], [71], [72] and [104].

A general solution for the transient temperature distribution produced in an infinite hollow cylinder subjected to convective (non-homogeneous) boundary conditions on both sides can be reached by applying and extending the main approach outlined in [45]. This solution is comparable to that presented in [19] and confirmed in [24]. Nevertheless, this approach does not

allow for predicting the effect of a concentrated heat source, typical of industrial and tribological systems.

During the last decades, the heat distribution in systems with rotating disks and a stationary concentrated heat source has been the subject of great scientific interest. Since the earlier pioneering works [6] and [53] concerning semi-infinite solids, which often were assumed to be adiabatic outside the region heated by a moving heat source, numerous other works have been developed. In particular, the effect of surface cooling by convection heat exchange was presented, most-likely for the first time, in [29] and it has been further developed in [37] and [72]. The same authors provided also an extension of their solution to the hollow cylinder geometry in [38] and [39]. These studies have shown that the evolution of the so-called 'flash temperature' [15], namely the hottest temperature that arises within the contact zone is described in terms of principal dimensionless characteristic parameters, i.e. the Peclet and Biot numbers. In the last years, in order to analyze the distribution of heat generated by friction, analytical solutions of thermal coupling between two solids in contact have been presented in further works, namely in [3], [8], [71] and [104].

However, all the quoted solutions basically follow a steady-state approach, while on the contrary it appears that no one has developed a relevant complete time transient solution for this kind of problem. On the other hand, a very simple approach to deal with a problem pertaining to a rotating cylinder subjected to a localized heating on its periphery is presented in [37]. In the present work, that approach is further developed and systematically extended to arrive at a full transient analytical solution of the tribological problem under target. This analytical solution of the heat conduction problem in a cylinder allows to simulate the evolution surface temperature during a long-run test in a very short time, whereas a FEM solution would require a huge amount of time. Hence, the analytical model appears more suitable for its use in an inverse analysis algorithm designed to solve iteratively the inverse problem.

4.3. Analytical solution of the thermal contact problem in rotating cylinders

The analytical solution is achieved in two steps. Firstly, the solution for a solid cylinder is introduced. Secondly, the previous solution is extended to the case of a hollow cylinder that is geometrically closer to the real sample geometry at the tribometer scale.

4.3.1. Solid cylinder

An infinitely long circular solid cylinder of radius ρ, with constant thermal conductivity k, rotating with constant angular velocity ω, is exposed to a convection heat transfer, with convection heat transfer coefficient h and ambient fluid temperature u_∞. Moreover, it is subjected to a constant concentrated heat flux q_e entering the solid on a circular arc with narrow opening angle $2\varphi_0$ (Figure 4), where, in principle, no convection takes place (for further details about the boundary conditions see Appendix B.3). Thus, the cylinder is heated on its peripheral surface by two different heat sources, while there is no internal thermal energy generation.

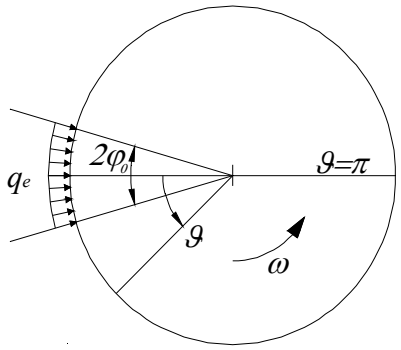

Figure 4.1: Rotating solid cylinder under concentrated heat conduction source and surrounding convection.

Heat conduction in the reference angular variable ϑ is considered with all terms, namely by accounting also for the direct temperature variation term in time. This gives rise to the following differential problem in the unknown temperature field $u(r,\vartheta,t)$ (see [45] and Appendix B.2.2):

$$\frac{1}{r}\frac{\partial}{\partial r}\left(r\frac{\partial u}{\partial r}\right)+\frac{1}{r^2}\frac{\partial^2 u}{\partial \vartheta^2}=\frac{1}{\alpha}\frac{\partial u}{\partial t}, \qquad 0\le r\le \rho,\ \ t\ge 0,\ \ 0\le \vartheta\le 2\pi \tag{4.1}$$

under conditions:

BC1: $$\left.\frac{\partial u}{\partial r}\right|_{r=\rho} = \begin{cases} Q_e = q_e/k, & -\varphi_0 \le \vartheta + \omega t \le \varphi_0 \\ -H\left(u|_{r=\rho} - u_\infty\right), & \varphi_0 \le \vartheta + \omega t \le 2\pi - \varphi_0 \end{cases}$$

BC2: $$\left.\frac{\partial u}{\partial r}\right|_{r=0} = 0$$

BC3: $$\lim_{r\to 0} u(r) \neq \pm\infty$$

BC4 (periodicity): $$\left.\frac{\partial u}{\partial \vartheta}\right|_{\vartheta=0} = \left.\frac{\partial u}{\partial \vartheta}\right|_{\vartheta=2\pi}, \qquad 0 \le r \le \rho$$
$$u|_{\vartheta=0} = u|_{\vartheta=2\pi}$$

Hereafter, the following current angular coordinate θ linked to the reference angular position ϑ and the angular rotation ω is defined:

$$\theta = \vartheta + \omega t \tag{4.2}$$

It incorporates the time dependence of the present steady-state solution. Indeed, given new variable θ, the derivatives of u with respect to t and ϑ become:

$$\frac{\partial}{\partial t}u(r,\theta,t) = \frac{\partial u}{\partial r}\frac{\partial r}{\partial t} + \frac{\partial u}{\partial \theta}\frac{\partial \theta}{\partial t} + \frac{\partial u}{\partial t}\frac{\partial t}{\partial t} = \frac{\partial u}{\partial r}0 + \frac{\partial u}{\partial \theta}\omega + \frac{\partial u}{\partial t}1 = \frac{\partial u}{\partial \theta}\omega + \frac{\partial u}{\partial t} \tag{4.3}$$

$$\frac{\partial}{\partial \vartheta}u(r,\theta,t) = \frac{\partial u}{\partial r}\frac{\partial r}{\partial \vartheta} + \frac{\partial u}{\partial \theta}\frac{\partial \theta}{\partial \vartheta} + \frac{\partial u}{\partial t}\frac{\partial t}{\partial \vartheta} = \frac{\partial u}{\partial r}0 + \frac{\partial u}{\partial \theta}1 + \frac{\partial u}{\partial t}0 = \frac{\partial u}{\partial \theta} \tag{4.4}$$

Instead, the derivative of u with respect to r remains unchanged.

Then, heat conduction Eq. (4.1) in new angular variable θ becomes:

$$\frac{1}{r}\frac{\partial u}{\partial r} + \frac{\partial^2 u}{\partial r^2} + \frac{1}{r^2}\frac{\partial^2 u}{\partial \theta^2} = \frac{\omega}{\alpha}\frac{\partial u}{\partial \theta} + \frac{1}{\alpha}\frac{\partial u}{\partial t} \tag{4.5}$$

under conditions:

IC: $$u(t=0) = f(r,\theta)$$

BC1: $$\left.\frac{\partial u}{\partial r}\right|_{r=\rho} = \begin{cases} Q_e = q_e/k, & -\varphi_0 \le \theta \le \varphi_0 \\ -H\left(u|_{r=\rho} - u_\infty\right), & \varphi_0 \le \theta \le 2\pi - \varphi_0 \end{cases}$$

BC2: $$\left.\frac{\partial u}{\partial r}\right|_{r=0} = 0$$

BC3: $$\lim_{r\to 0} u(r) \neq \pm\infty$$

BC4 (periodicity): $$\left.\frac{\partial u}{\partial \theta}\right|_{\theta=0} = \left.\frac{\partial u}{\partial \theta}\right|_{\theta=2\pi}, \qquad 0 \le r \le \rho$$
$$u|_{\theta=0} = u|_{\theta=2\pi}$$

Due to the non-homogeneous boundary condition BC1, the solution of the present problem will be given by the superposition of the steady-state solution with a non-homogeneous boundary condition $u_{nh}(r,\theta)$ and of the transient solution of the associated homogeneous problem $u_h(r,\theta,t)$ [45]. Hence:

$$u(r,\theta,t) = u_{nh}(r,\theta) + u_h(r,\theta,t) \quad (4.6)$$

4.3.1.1. Solution of the steady-state problem (non-homogeneous boundary condition)

The mathematical formulation of the steady-state problem is given as:

$$\frac{1}{r}\frac{\partial u_{nh}}{\partial r} + \frac{\partial^2 u_{nh}}{\partial r^2} + \frac{1}{r^2}\frac{\partial^2 u_{nh}}{\partial \theta^2} = \frac{\omega}{\alpha}\frac{\partial u_{nh}}{\partial \theta} \quad (4.7)$$

under conditions:

BC1: $$\left.\frac{\partial u_{nh}}{\partial r}\right|_{r=\rho} = \begin{cases} Q_e = q_e/k, & -\varphi_0 \le \theta \le \varphi_0 \\ -H\left(u_{nh}|_{r=\rho} - u_\infty\right), & \varphi_0 \le \theta \le 2\pi - \varphi_0 \end{cases}$$

BC2: $$\left.\frac{\partial u_{nh}}{\partial r}\right|_{r=0} = 0$$

BC3: $$\lim_{r\to 0} u_{nh}(r) \neq \pm\infty$$

BC4 (periodicity): $$\left.\frac{\partial u_{nh}}{\partial \theta}\right|_{\theta=0} = \left.\frac{\partial u_{nh}}{\partial \theta}\right|_{\theta=2\pi}, \qquad 0 \le r \le \rho$$

$$u|_{\theta=0} = u|_{\theta=2\pi}$$

Using the following integral Fourier transform [10, 24]:

$$\tilde{u}_{nh}(r,n) = \int_{-\pi}^{\pi} u_{nh}(r,\theta) e^{-jn\theta} d\theta \quad (4.8)$$

where j is the imaginary unit and n is an integer, given the properties of Fourier transforms and by taking into account the periodicity conditions, Eq. (4.7) becomes:

$$\frac{\partial^2 \tilde{u}_{nh}}{\partial r^2} + \frac{1}{r}\frac{\partial \tilde{u}_{nh}}{\partial r} + \left(-jn\frac{\omega}{\alpha} - \frac{n^2}{r^2}\right)\tilde{u}_{nh} = 0 \quad (4.9)$$

which can be rewritten as:

$$r^2\frac{\partial^2 \tilde{u}_{nh}}{\partial r^2} + r\frac{\partial \tilde{u}_{nh}}{\partial r} + \left(-j\frac{n\omega}{\alpha}r^2 - n^2\right)\tilde{u}_{nh} = 0 \quad (4.10)$$

Eq. (4.10) (or, equivalently, Eq. (4.9)) represents a particular case of the Bessel equation. Its solution is a Bessel function of order n with imaginary argument, equivalent to a Kelvin function, [1] and [98].

By defining:

$$\epsilon_n = \sqrt{-j\frac{n\omega}{\alpha}} \tag{4.11}$$

the solution of Eq. (4.10) is the following:

$$\tilde{u}_{nh}(r,n) = D_n J_n(\epsilon_n r) \tag{4.12}$$

where D_n is a constant and, due to the third boundary condition (BC3), Bessel function of the second kind $Y_n(r\epsilon_n)$ is omitted.

Eq. (4.12) displays the following derivative (see Appendix D):

$$\frac{\partial}{\partial r}\,\tilde{u}_{nh}(r,n) = D_n \frac{\partial}{\partial r} J_n(r\epsilon_n) = D_n\left[\frac{n}{r}J_n(r\epsilon_n) - \epsilon_n J_{n+1}(r\epsilon_n)\right] \tag{4.13}$$

Applying the integral Fourier transform to the boundary conditions BC1 of Eq. (4.7), one obtains [10]:

$$\frac{\partial}{\partial r}\,\tilde{u}_{nh}(\rho,n) = \int_{-\varphi_0}^{\varphi_0} Q_e e^{-jn\theta}\,d\theta - \int_{\varphi_0}^{2\pi-\varphi_0} H\left(u|_{r=\rho} - u_\infty\right)e^{-jn\theta}\,d\theta \tag{4.14}$$

As shown in [8] and [36], and commonly done in the literature, to solve this type of problem, given the narrow opening of the arc where the conduction heat source takes place, it is possible to consider that the convection boundary condition in BC1 can be applied to the entire range $-\pi \le \theta \le \pi$, namely to all the circumferential border, without this affecting considerably the solution. Thus, it is possible to rewrite BC1 as follows:

$$\frac{\partial}{\partial r}\,\tilde{u}_{nh}(\rho,n) = -H\tilde{u}_{nh}|_{r=\rho} + \tilde{K}_n \tag{4.15}$$

where:

$$\tilde{K}_n = H\int_{-\pi}^{\pi} u_\infty e^{-jn\theta}d\theta + \int_{-\varphi_0}^{\varphi_0} Q_e e^{-jn\theta}\,d\theta \tag{4.16}$$

In order to determine constant D_n, Eq. (4.12) and Eq. (4.13) should be substituted in boundary condition (4.15):

$$-HD_nJ_n(\rho\epsilon_n) + \widetilde{K}_n + \tilde{Q}_n = D_n\left[\frac{n}{\rho}J_n(\rho\epsilon_n) - \epsilon_n J_{n+1}(\rho\epsilon_n)\right] \quad (4.17)$$

$$D_n\left[\left(\frac{n}{\rho} + H\right)J_n(\rho\epsilon_n) - \epsilon_n J_{n+1}(\rho\epsilon_n)\right] = \widetilde{K}_n + \tilde{Q}_n \quad (4.18)$$

$$D_n\frac{1}{\rho}[(n + H\rho)J_n(\rho\epsilon_n) - \epsilon_n\rho J_{n+1}(\rho\epsilon_n)] = \widetilde{K}_n + \tilde{Q}_n \quad (4.19)$$

$$D_n = \frac{\rho\widetilde{K}_n}{(n + H\rho)J_n(\rho\epsilon_n) - \epsilon_n\rho J_{n+1}(\rho\epsilon_n)} \quad (4.20)$$

Then, Eq. (4.12) becomes:

$$\tilde{u}_{nh}(r,n) = \frac{\rho\widetilde{K}_n}{(n + H\rho)J_n(\rho\epsilon_n) - \epsilon_n\rho J_{n+1}(\rho\epsilon_n)}J_n(\epsilon_n r) \quad (4.21)$$

Finally, by applying the Inverse Fourier Transform, it is possible to determine the sought quasi steady-state solution [71] and [104]:

$$u_{nh}(r,\theta) = \frac{1}{2\pi}\sum_{n=0}^{\infty}\delta_n\, Re\left[\frac{\rho\widetilde{K}_n}{(n + H\rho)J_n(\rho\epsilon_n) - \epsilon_n\rho J_{n+1}(\rho\epsilon_n)}J_n(\epsilon_n r)e^{jn\theta}\right] \quad (4.22)$$

where $\delta_n = \begin{cases}1 & n = 0\\ 2 & n \neq 0\end{cases}$.

It is worth mentioning that for $n = 0$:

$$\widetilde{K}_0 = H\int_{-\pi}^{\pi}u_\infty e^{-j0\theta}d\theta = 2\pi H u_\infty \quad (4.23)$$

$$\tilde{Q}_0 = \int_{-\varphi_0}^{\varphi_0}Q_e e^{-j0\theta}\,d\theta = 2\varphi_0 Q_e \quad (4.24)$$

$$\tilde{u}(r,0) = \frac{2(\pi H u_\infty + \varphi_0 Q_e)}{HJ_0(\rho\epsilon_0) - \epsilon_0 J_1(\rho\epsilon_0)}J_0(\epsilon_0 r) = \frac{2(\pi H u_\infty + \varphi_0 Q_e)}{H} \quad (4.25)$$

being $\epsilon_0 = \sqrt{-\mathrm{j}\frac{0\omega}{\alpha}} = 0$. By applying the Inverse Fourier Transform, it is in fact possible to obtain:

$$u_{nh_0}(r,\theta) = \frac{Hu_\infty + \frac{\varphi_0}{\pi}Q_e}{H} = u_\infty + \frac{\varphi_0}{\pi}\frac{Q_e}{H} \quad (4.26)$$

which is the solution of the solid cylinder one-dimensional steady-state problem. So, for *n*=0, Eq. (4.21) provides the solution of a one-dimensional steady-state problem, whereby the concentrated heat flux (Q_e) referring to a narrow opening of the arc segment ($2\varphi_0$) where the conduction heat source takes place, is considered spread over the entire angular range

$-\pi \leq \theta \leq \pi$, namely to all the circumferential border, so that the dependence on the angular coordinate disappears.

Finally, the quasi steady-state solution can be rewritten as follows:

$$u(r,\theta) = u_\infty + \frac{\varphi_0}{\pi}\frac{Q_e}{H} + \frac{1}{\pi}\sum_{n=1}^{\infty} Re\left[\frac{\rho\left(\tilde{K}_n + \tilde{Q}_n\right)}{(n+H\rho)J_n(\epsilon_n\rho) - \epsilon_n\rho J_{n+1}(\epsilon_n\rho)} J_n(\epsilon_n r)e^{jn\theta}\right] \quad (4.27)$$

4.3.1.2. Solution of the transient problem (homogeneous boundary condition)

The mathematical formulation of the transient problem is given as:

$$\frac{1}{r}\frac{\partial u_h}{\partial r} + \frac{\partial^2 u_h}{\partial r^2} + \frac{1}{r^2}\frac{\partial^2 u_h}{\partial \theta^2} = \frac{\omega}{\alpha}\frac{\partial u_h}{\partial \theta} + \frac{1}{\alpha}\frac{\partial u_h}{\partial t} \quad (4.28)$$

under conditions:

IC: $u_h(t=0) = f_h(r,\theta) = f(r,\theta) - u_{nh}(r,\theta)$

BC1: $\left.\frac{\partial u_h}{\partial r}\right|_{r=\rho} = \begin{cases} 0, & -\varphi_0 \leq \theta \leq \varphi_0 \\ -Hu_h|_{r=\rho}, & \varphi_0 \leq \theta \leq 2\pi - \varphi_0 \end{cases}$

BC2: $\left.\frac{\partial u_h}{\partial r}\right|_{r=0} = 0$

BC3: $\lim_{r\to 0} u_h(r) \neq \pm\infty$

BC4 (periodicity): $\left.\frac{\partial u_h}{\partial \theta}\right|_{\theta=0} = \left.\frac{\partial u_h}{\partial \theta}\right|_{\theta=2\pi}, \quad 0 \leq r \leq \rho$

$u_h|_{\theta=0} = u_h|_{\theta=2\pi},$

By applying a separation of variables in the form:

$$u_h(r,\theta,t) = v(r,\theta)T(t) \quad (4.29)$$

Eq. (4.28) becomes:

$$\frac{T}{r}\frac{\partial v}{\partial r} + T\frac{\partial^2 v}{\partial r^2} + \frac{T}{r^2}\frac{\partial^2 v}{\partial \theta^2} - \frac{\omega T}{\alpha}\frac{\partial v}{\partial \theta} = \frac{v}{\alpha}\frac{dT}{dt} \quad (4.30)$$

Such equality can hold only if both hand sides of the equation, one dependent on r and θ, the other on t, are set equal to the same constant value, said separation constant. Hence, the only way to satisfy this equality is to equate each group of functions to an arbitrary quantity $-\lambda^2$. Eq. (4.30) leads then to two separate differential equations. The first one is time dependent only:

$$\frac{dT}{dt} + \alpha\lambda^2 T = 0 \qquad (4.31)$$

and the second one is space dependent only:

$$r\frac{\partial v}{\partial r} + r^2\frac{\partial^2 v}{\partial r^2} + \frac{\partial^2 v}{\partial \theta^2} - \frac{\omega r^2}{\alpha}\frac{\partial v}{\partial \theta} + (\lambda r)^2 v = 0 \qquad (4.32)$$

under boundary conditions:

BC1: $$\left.\frac{\partial v}{\partial r}\right|_{r=\rho} = \begin{cases} 0, & -\varphi_0 \le \theta \le \varphi_0 \\ -Hu_h|_{r=\rho}, & \varphi_0 \le \theta \le 2\pi - \varphi_0 \end{cases}$$

BC2: $$\left.\frac{\partial v}{\partial r}\right|_{r=0} = 0$$

BC3: $$\lim_{r\to 0} v(r) \neq \pm\infty$$

BC4 (periodicity): $$\left.\frac{\partial u_h}{\partial \theta}\right|_{\theta=0} = \left.\frac{\partial u_h}{\partial \theta}\right|_{\theta=2\pi}, \quad 0 \le r \le \rho$$

$$u_h|_{\theta=0} = u_h|_{\theta=2\pi},$$

Eq. (4.31) displays the general solution:

$$T(t) = Be^{-\alpha\lambda^2 t} \qquad (4.33)$$

To find a solution of Eq. (4.32), the following integral Fourier transform can be used:

$$\tilde{v}(r,n) = \int_{-\pi}^{\pi} v(r,\theta)e^{-jn\theta}d\theta \qquad (4.34)$$

Given the properties of Fourier transforms and by taking into account the periodicity conditions, Eq. (4.32) becomes:

$$r\frac{\partial \tilde{v}}{\partial r} + r^2\frac{\partial^2 \tilde{v}}{\partial r^2} - n^2\tilde{v} - j\frac{n\omega r^2}{\alpha}\tilde{v} + (\lambda r)^2\tilde{v} = 0 \qquad (4.35)$$

which can be rewritten as:

$$r\frac{\partial \tilde{v}}{\partial r} + r^2\frac{\partial^2 \tilde{v}}{\partial r^2} + \left(\left(\lambda^2 - j\frac{n\omega}{\alpha}\right)r^2 - n^2\right)\tilde{v} = 0 \qquad (4.36)$$

under boundary conditions:

BC1: $$\left.\frac{\partial \tilde{v}}{\partial r}\right|_{r=\rho} = -H\int_{-\pi}^{\pi}\tilde{v}|_{r=\rho}e^{-jn\theta}d\theta = -H\tilde{v}(\rho,n)$$

BC2: $$\left.\frac{\partial \tilde{v}}{\partial r}\right|_{r=0} = 0$$

BC3: $$\lim_{r\to 0}\tilde{v}(r) \neq \pm\infty$$

Eq. (4.36) (or, equivalently, Eq. (4.35)) represents a particular case of the Bessel equation. Its solution is a Bessel function of order n with argument characterized by an imaginary quantity. By defining:

$$\Lambda = \sqrt{\lambda^2 - j\frac{n\omega}{\alpha}} \qquad (4.37)$$

the solution of Eq. (4.36) is the following:

$$\tilde{v}\big(r, \Lambda(n,\lambda)\big) = B_n J_n(r\Lambda) \qquad (4.38)$$

where B_n is a constant and, due to the third boundary condition (BC3), Bessel function of the second kind $Y_n(r\epsilon_n)$ is omitted.

The application of the Fourier transform allowed to split the problem into *n* sub-problems, each characterized by a specific frequency. Then, the solution of the problem comes from the solutions of each sub-problem. This means that for each value of n, there is a unique set of eigenvalues $\lambda_1, \lambda_2, \ldots, \lambda_m$, due to Bessel function's oscillatory behavior. So, Eq. (4.37) can be rewritten as:

$$\Lambda_{mn} = \sqrt{\lambda_{mn}^2 - j\frac{n\omega}{\alpha}} \qquad (4.39)$$

where index m spans the eigenvalues in the Bessel expansion and index n spans the frequencies in the Fourier expansion.

To solve each sub-problem, a solution procedure might be detected by analyzing the simplest case, namely that relating to the null frequency $n = 0$. In that case, the mathematical formulation of the homogeneous problem is given as:

$$\frac{\partial^2 \tilde{v}_0}{\partial r^2} + \frac{1}{r}\frac{\partial \tilde{v}_0}{\partial r} + \lambda_{m0}^2 \tilde{v}_0 = 0 \qquad (4.40)$$

under conditions:

BC1: $\left.\frac{\partial \tilde{v}_0}{\partial r}\right|_{r=\rho} + H\tilde{v}_0|_{r=\rho} = 0$

BC2: $\left.\frac{\partial \tilde{v}_0}{\partial r}\right|_{r=0} = 0$

BC3: $\lim_{r\to 0} \tilde{v}_0(r, \lambda_{m0}) \neq \pm\infty$

Eq. (4.40) represents a Bessel equation of order zero. Its solution is:

$$\tilde{v}_0(r) = B_0 J_0(\lambda r) \qquad (4.41)$$

where, due to the third boundary condition, the Bessel function of the second kind of order zero (i.e. $Y_0(\lambda r)$) is omitted. The eigenvalues λ_m of Eq. (4.41) can be determined by the following trascendental equation, achieved through the boundary conditions (see Appendix D):

$$HJ_0(\lambda_m \rho) = \lambda_m J_1(\lambda_m \rho) \qquad (4.42)$$

and the general solution is then formed by the summation over all products:

$$\tilde{v}_0(r,0) = \sum_{m=1}^{\infty} B_{m0} J_0(\lambda_m r) \qquad (4.43)$$

The case with $n > 0$ now follows. It is possible to rewrite Eq. (4.36) as follows:

$$r\frac{\partial}{\partial r}\tilde{v}_n + r^2\frac{\partial^2}{\partial r^2}\tilde{v}_n + \left(\left({\lambda_{mn}}^2 - j\frac{n\omega}{\kappa}\right)r^2 - n^2\right)\tilde{v}_n = 0 \qquad (4.44)$$

with boundary condition:

$$\frac{\partial}{\partial r}\tilde{v}_n(\rho) + H_e\tilde{v}_n(\rho) = 0 \qquad (4.45)$$

The eigenvalues λ_{mn} are the roots of the following equation, with Λ_{mn} given by Eq. (4.39):

$$\left(\frac{n}{\rho} + H_e\right)J_n(\rho\Lambda_{mn}) = \Lambda_{mn}J_{n+1}(\rho\Lambda_{mn}) \qquad (4.46)$$

Then, the general solution is formed by the summation over all boundary value problem solutions:

$$\tilde{v}(r,n) = \sum_{m=1}^{\infty} B_{mn} J_n(r\Lambda_{mn}) \qquad (4.47)$$

Therefore, each solution of the *n* sub-problems ($\tilde{v}(r,n)$) in which the problem has been split has been determined.

To go back to the original variable v, the inverse integral Fourier transform must be applied. That allows to get the solution for the radial and angular dependent problem:

$$v(r,\theta) = \frac{1}{2\pi}\sum_{n=0}^{\infty}\delta_n Re\left[\tilde{v}(r,n)e^{jn\theta}\right] = \frac{1}{2\pi}\sum_{n=0}^{\infty}\delta_n Re\left[\sum_{m=1}^{\infty} B_{mn}J_n(r\Lambda)\right]e^{jn\theta} \qquad (4.48)$$

where $\delta_n = \begin{cases} 1 & n = 0 \\ 2 & n \neq 0 \end{cases}$.

Next, the complete solution is obtained by multiplying the solution independent on time with the one dependent on time, hence:

$$u_h(r,\theta,t) = \frac{1}{2\pi}\sum_{n=0}^{\infty}\delta_n Re\left[\sum_{m=1}^{\infty} A_{mn}J_n(r\Lambda)\, e^{jn\theta} e^{-\alpha\lambda_{mn}{}^2 t}\right] \quad (4.49)$$

where:

$$A_{mn} = C_{mn}B_{mn} \quad (4.50)$$

To determine the A_{mn} values, the initial condition must be applied. However, given the non-homogeneity of the boundary conditions, the steady-state solution $u_{nh}(r,\theta)$ must be subtracted from the initial condition $f(r,\theta)$, namely:

$$f_h(r,\theta) = f(r,\theta) - u_{nh}(r,\theta) \quad (4.51)$$

So, by applying the initial condition $f_h(r,\theta)$ to the found complete solution, it follows that (see Appendix C):

$$f_h(r,\theta) = \frac{1}{2\pi}\sum_{n=0}^{\infty}\delta_n Re\left[\sum_{m=1}^{\infty} A_{mn}J_n(r\Lambda)\right] e^{jn\theta} \quad (4.52)$$

The previous formula can be considered as a Fourier series, so, for the properties of Fourier series, the unknown coefficients A_{mn} can be evaluated as:

$$\frac{1}{2\pi}\int_{-\pi}^{\pi} f_h e^{-jn\theta}\, d\theta = \frac{1}{2\pi} Re\left[\sum_{m=1}^{\infty} A_{mn}J_n(r\Lambda)\right] \quad (4.53)$$

For the property of Fourier-Bessel series, multiplying both sides by $\int_0^{\rho} rJ_n(r\Lambda)\, dr$, the previous formula can be further reduced to:

$$\int_0^{\rho}\left(\int_{-\pi}^{\pi} f_h e^{-jn\theta}\, d\theta\right) rJ_n(r\Lambda)dr = \int_0^{\rho} Re\left[\sum_{m=1}^{\infty} A_{mn}J_n(r\Lambda)\right] rJ_n(r\Lambda)\, dr \quad (4.54)$$

$$\int_0^{\rho}\left(\int_{-\pi}^{\pi} f_h e^{-jn\theta}\, d\theta\right) rJ_n(r\Lambda)dr = A_{mn} Re\left[\int_0^{\rho} rJ_n(r\Lambda)^2 dr\right] \quad (4.55)$$

$$A_{mn} = \frac{\int_0^{\rho}\left(\int_{-\pi}^{\pi} f_h e^{-jn\theta}\, d\theta\right) rJ_n(r\Lambda)dr}{Re\left[\int_0^{\rho} rJ_n(r\Lambda)^2 dr\right]} \quad (4.56)$$

Using the Bessel function integral properties, the denominator can be evaluated as:

$$N_n(\Lambda_{mn}) = \frac{\rho^2}{2}[J_n(\Lambda_{mn}\rho)^2 - J_{n+1}(\Lambda_{mn}\rho)J_{n-1}(\Lambda_{mn}\rho)] = \frac{\rho^2}{2}[J_n(\Lambda_{mn}\rho)^2 + J_{n+1}(\Lambda_{mn}\rho)^2] \quad (4.57)$$

Instead, the integral at the numerator can be evaluated numerically, as:

$$\begin{aligned}\int_0^\rho \left(\int_{-\pi}^{\pi} f_h(r,\theta)e^{-jn\theta}d\theta\right) rJ_n(r\Lambda)dr \\ = \int_0^\rho \left(\int_{-\pi}^{\pi} \big(f(r,\theta) - u_{nh}(r,\theta)\big)e^{-jn\theta}d\theta\right) rJ_n(r\Lambda)dr \\ = \int_0^\rho \left(\int_{-\pi}^{\pi} f(r,\theta)e^{-jn\theta}d\theta \right. \\ \left. - \int_{-\pi}^{\pi} u_{nh}(r,\theta)e^{-jn\theta}d\theta\right) rJ_n(r\Lambda)dr\end{aligned} \quad (4.58)$$

being:

$$\tilde{u}_{nh}(r,n) = \int_{-\pi}^{\pi} u_{nh}(r,\theta)e^{-jn\theta}d\theta \quad (4.59)$$

Eq. (4.58) can be rewritten as:

$$\int_0^\rho \left[\left(\int_{-\pi}^{\pi} f(r,\theta)e^{-jn\theta}d\theta\right) - \tilde{u}_{nh}(r,n)\right] rJ_0(r\Lambda)dr \quad (4.60)$$

For the particular case $f(r,\theta) = f_0 = \text{const}$ or $f(r,\theta) = f_0(r)$, the integral at the numerator becomes, for $n = 0$:

$$\begin{aligned}\int_0^\rho \left(\int_{-\pi}^{\pi} f(r,\theta)e^{-jn\theta}d\theta - \tilde{u}_{nh}(r,0)\right) rJ_0(r\Lambda)dr \\ = \int_0^\rho \big(2\pi f_0(r) - \tilde{u}_{nh}(r,0)\big) rJ_0(r\Lambda)dr\end{aligned} \quad (4.61)$$

$$A_{m0} = \frac{\int_0^\rho \big(2\pi f_0(r) - \tilde{u}_{nh}(r,0)\big) rJ_0(r\Lambda)dr}{\rho\Lambda[J_0(\Lambda_{mn}\rho)^2 + J_1(\Lambda_{mn}\rho)^2]} \quad (4.62)$$

Otherwise, for $n > 0$:

$$\int_{-\pi}^{\pi} f_n(r)e^{-jn\theta}d\theta = f_n(r)\int_{-\pi}^{\pi} e^{-jn\theta}d\theta = 0 \quad (4.63)$$

being $e^{-jn\theta}$ a periodic function such as $\int_{-\pi}^{\pi} e^{-jn\theta}d\theta = 0$.

Remembering that $\tilde{u}_{nh}(r,n) = D_n J_n(\epsilon_n r)$, so:

$$\int_0^\rho \tilde{u}_{nh}(r,n) rJ_n(r\Lambda)dr = D_n \int_0^\rho J_n(r\epsilon_n) rJ_n(r\Lambda_{mn})rdr \quad (4.64)$$

thus:

$$A_{mn} = \frac{2D_n \int_0^{\rho} J_n(r\epsilon_n) r J_n(r\Lambda_{mn}) r dr}{Re(\rho^2[J_n(\Lambda_{mn}\rho)^2 + J_{n+1}(\Lambda_{mn}\rho)^2])} \tag{4.65}$$

The problem exact solution is given, hence, by the following equation:

$$\begin{aligned} u(r,\theta,t) &= u_{nh}(r,\theta) + u_h(r,\theta,t) \\ &= \frac{1}{2\pi}\sum_{n=0}^{\infty} \delta_n \, Re\left[\frac{\rho \widetilde{K}_n}{(n+H\rho)J_n(\rho\epsilon_n) - \epsilon_n \rho J_{n+1}(\rho\epsilon_n)} J_n(\epsilon_n r) e^{jn\theta}\right] \\ &+ \frac{1}{2\pi}\sum_{n=0}^{\infty} \delta_n Re\left[\sum_{m=1}^{\infty} A_{mn} J_n(r\Lambda)\, e^{jn\theta} e^{-\alpha {\lambda_{mn}}^2 t}\right] \end{aligned} \tag{4.66}$$

4.3.2. Hollow cylinder

Considering a long hollow cylinder of external radius ρ_e and internal radius ρ_i, rotating with constant angular velocity ω, the angular dependence of the temperature distribution is investigated, as done earlier for the solid cylinder. Although most of most crucial steps have been already exposed for that case, the derivation is repeated here and adopted, in all steps, for the ease of the reader.

At $r = \rho_e$, the external boundary is exposed to a convection heat transfer, with convection heat transfer coefficient h_e and ambient fluid temperature $u_{\infty,e}$; at $r = \rho_i$, it is exposed to a different convection heat transfer, with convection heat transfer coefficient h_i and ambient fluid temperature $u_{\infty,i}$. Moreover, the cylinder is subjected to an external constant heat flux source concentrated on a circular arc with narrow opening angle $2\varphi_0$ (Figure 4.2). Thus, at $r = \rho_e$ the cylinder is heated on its peripheral surface by two different heat sources.

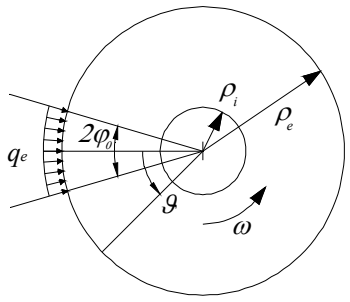

Figure 4.2: Rotating hollow cylinder under external heat conduction source and surrounding external and internal convection.

Then, the heat conduction problem for a hollow cylinder in the current angular coordinate $\theta = \vartheta + \omega t$ takes the following form (see Appendix B):

$$\frac{1}{r}\frac{\partial u}{\partial r} + \frac{\partial^2 u}{\partial r^2} + \frac{1}{r^2}\frac{\partial^2 u}{\partial \theta^2} = \frac{\omega}{\alpha}\frac{\partial u}{\partial \theta} + \frac{1}{\alpha}\frac{\partial u}{\partial t} \qquad (4.67)$$

under conditions:

IC: $u(t=0) = f(r,\theta)$

BC1: $\left.\frac{\partial u}{\partial r}\right|_{r=\rho} = \begin{cases} Q_e = q_e/k, & -\varphi_0 \le \theta \le \varphi_0 \\ -H_e\left(u|_{r=\rho_e} - u_{\infty,e}\right), & \varphi_0 \le \theta \le -\varphi_0 \end{cases}$

BC2: $\left.\frac{\partial u}{\partial r}\right|_{r=0} = -H_i\left(u|_{r=\rho_i} - u_{\infty,i}\right)$

BC3 (periodicity): $\left.\frac{\partial u}{\partial \vartheta}\right|_{\theta=0} = \left.\frac{\partial u}{\partial \vartheta}\right|_{\theta=2\pi}, \quad \rho_i \le r \le \rho_e$

$u|_{\theta=0} = u|_{\theta=2\pi},$

Due to non-homogeneous boundary conditions BC1 and BC2, the solution of the present problem will be given by the superposition of the steady-state solution with non-homogeneous boundary condition $u_{nh}(r,\theta)$ and of the transient solution of the associated homogeneous problem $u_h(r,\theta,t)$ [45]. Hence:

$$u(r,\theta,t) = u_{nh}(r,\theta) + u_h(r,\theta,t) \qquad (4.68)$$

4.3.2.1. Solution of the steady-state problem (non-homogeneous boundary condition)

From Eq. (4.67), being $u_{nh} = u(r,\vartheta)$ the unknown temperature distribution, the mathematical formulation of the problem becomes:

$$\frac{\partial^2 u_{nh}}{\partial r^2} + \frac{1}{r}\frac{\partial u_{nh}}{\partial r} + \frac{1}{r^2}\frac{\partial^2 u_{nh}}{\partial \theta^2} = \frac{\omega}{\alpha}\frac{\partial u_{nh}}{\partial \theta} \qquad (4.69)$$

under conditions:

BC1: $\left.\frac{\partial u_{nh}}{\partial r}\right|_{r=\rho_e} = \begin{cases} Q_e = q_e/k, & -\varphi_0 \le \theta \le \varphi_0 \\ -H_e\left(u_{nh}|_{r=\rho_e} - u_{\infty,e}\right), & \varphi_0 \le \theta \le 2\pi - \varphi_0 \end{cases}$

BC2: $\left.\frac{\partial u_{nh}}{\partial r}\right|_{r=\rho_i} = -H_i\left(u_{nh}|_{r=\rho_i} - u_{\infty,i}\right)$

BC3 (periodicity):

$$\left.\frac{\partial u_{nh}}{\partial \vartheta}\right|_{\vartheta=0} = \left.\frac{\partial u_{nh}}{\partial \vartheta}\right|_{\vartheta=2\pi}, \qquad \rho_i \le r \le \rho_e$$
$$u_{nh}|_{\vartheta=0} = u_{nh}|_{\vartheta=2\pi},$$

Notice again that in Eq. (4.69) the dependence on the time variable t is incorporated through the current rotating angle θ. So, in this treatment, the problem is considered in a quasi steady-state formulation, in apparent variables *r* and θ.

Using the following integral Fourier transform:

$$\tilde{u}_{nh}(r,n) = \int_{-\pi}^{\pi} u_{nh}(r,\theta) e^{-jn\theta} d\theta \qquad (4.70)$$

and taking into account the periodicity conditions, Eq. (4.69) becomes:

$$r^2 \frac{d^2\tilde{u}_{nh}}{dr^2} + r\frac{d\tilde{u}_{nh}}{dr} + \left(-j\frac{n\omega}{\alpha}r^2 - n^2\right)\tilde{u}_{nh} = 0 \qquad (4.71)$$

Eq. (4.71) represents a particular case of the Bessel equation. By defining:

$$\epsilon_n = \sqrt{-j\frac{n\omega}{\alpha}} \qquad (4.72)$$

the solution of Eq. (4.71) is the following:

$$\tilde{u}_{nh}(r,n) = D_n J_n(\epsilon_n r) + E_n Y_n(\epsilon_n r) \qquad (4.73)$$

Eq. (4.73) has the following radial derivative [1] (see also Appendix D):

$$\begin{aligned}\frac{d}{dr}\tilde{u}_{nh}(r,n) &= D_n \frac{d}{dr}J_n(\epsilon_n r) + E_n \frac{d}{dr}Y_n(\epsilon_n r) \\ &= D_n\left[\frac{n}{r}J_n(\epsilon_n r) - \epsilon_n J_{n+1}(\epsilon_n r)\right] \\ &+ E_n\left[\frac{n}{r}Y_n(\epsilon_n r) - \epsilon_n Y_{n+1}(\epsilon_n r)\right]\end{aligned} \qquad (4.74)$$

By applying the integral Fourier transform to boundary condition BC1 of Eq. (4.69), one obtains:

$$\frac{d}{dr}\tilde{u}_{nh}(\rho_e,n) = \int_{-\varphi_0}^{\varphi_0} e^{-jn\theta} Q_e \, d\theta - \int_{\varphi_0}^{2\pi-\varphi_0} e^{-jn\theta} H_e\left(\tilde{u}(\rho_e,n) - u_{\infty,e}\right) d\theta \qquad (4.75)$$

As done previously, the convection boundary condition in BC1 is applied to the entire range $-\pi \le \theta \le \pi$, namely to all the external circumferential border, without affecting considerably the solution, if the concentrated heat flux acts on an arc with narrow opening. Thus, it is possible to rewrite BC1 as follows:

$$\frac{d}{dr}\,\tilde{u}_{nh}(\rho_e,n) = -H_e\tilde{u}_{nh}(\rho_e,n) + \widetilde{K}_{e,n} \tag{4.76}$$

where

$$\widetilde{K}_{e,n} = H_e\int_{-\pi}^{\pi} u_{\infty,e}e^{-jn\theta}d\theta + \int_{-\varphi_0}^{\varphi_0} e^{-jn\theta}Q_e\,d\theta \tag{4.77}$$

Similarly, by applying the integral Fourier transform to boundary conditions BC2 of Eq. (4.69), one obtains:

$$\frac{d}{dr}\,\tilde{u}_{nh}(\rho_i,n) = -\int_{-\pi}^{\pi} e^{-jn\theta}H_i\big(\tilde{u}(\rho_i,n) - u_{\infty,i}\big)\,d\theta = -H_i\tilde{u}_{nh}(\rho_i,n) + \widetilde{K}_{i,n} \tag{4.78}$$

where

$$\widetilde{K}_{i,n} = H_i\int_{-\pi}^{\pi} u_{\infty,i}e^{-jn\theta}d\theta \tag{4.79}$$

In order to determine constants D_n and E_n, BC1 and BC2 are rewritten in light of Eq. (4.73) and Eq. (4.74). Then, it follows that:

$$\begin{aligned} D_n\left[\frac{n}{\rho_e}J_n(\epsilon_n\rho_e) - \epsilon_n J_{n+1}(\epsilon_n\rho_e)\right] + E_n\left[\frac{n}{\rho_e}Y_n(\epsilon_n\rho_e) - \epsilon_n Y_{n+1}(\epsilon_n\rho_e)\right] = \\ = -H_e\big(D_nJ_n(\epsilon_n\rho_e) + E_nY_n(\epsilon_n\rho_e)\big) + \widetilde{K}_{e,n} \end{aligned} \tag{4.80}$$

$$\begin{aligned} D_n\left[\frac{n}{\rho_i}J_n(\epsilon_n\rho_i) - \epsilon_n J_{n+1}(\epsilon_n\rho_i)\right] + E_n\left[\frac{n}{\rho_i}Y_n(\epsilon_n\rho_i) - \epsilon_n Y_{n+1}(\epsilon_n\rho_i)\right] = \\ = -H_i\big(D_nJ_n(\epsilon_n\rho_i) + E_nY_n(\epsilon_n\rho_i)\big) + \widetilde{K}_{i,n} \end{aligned} \tag{4.81}$$

These can be rewritten as:

$$D_nI_n(\epsilon_n\rho_e,H_e) + E_nY_n(\epsilon_n\rho_e,H_e) = \widetilde{K}_{e,n} \tag{4.82}$$

$$D_nI_n(\epsilon_n\rho_i,H_i) + E_nY_n(\epsilon_n\rho_i,H_i) = \widetilde{K}_{i,n} \tag{4.83}$$

where:

$$I_n(\epsilon_n r,H) = \left(\frac{n}{r} + H\right)J_n(\epsilon_n r) - \epsilon_n J_{n+1}(\epsilon_n r) \tag{4.84}$$

$$Y_n(\epsilon_n r,H) = \left(\frac{n}{r} + H\right)Y_n(\epsilon_n r) - \epsilon_n Y_{n+1}(\epsilon_n r) \tag{4.85}$$

From straight-forward mathematical manipulations of Eq. (4.82) and Eq. (4.83), constants D_n and E_n can be solved as:

$$D_n = \frac{\widetilde{K}_{e_n}Y_n(\epsilon_n\rho_i,H_i) - \widetilde{K}_{i_n}Y_n(\epsilon_n\rho_e,H_e)}{I_n(\epsilon_n\rho_e,H_e)Y_n(\epsilon_n\rho_i,H_i) - I_n(\epsilon_n\rho_i,H_i)Y_n(\epsilon_n\rho_e,H_e)} \tag{4.86}$$

$$E_n = \frac{\widetilde{K}_{e_n}I_n(\epsilon_n\rho_i,H_i) - \widetilde{K}_{i_n}I_n(\epsilon_n\rho_e,H_e)}{Y_n(\epsilon_n\rho_e,H_e)I_n(\epsilon_n\rho_i,H_i) - Y_n(\epsilon_n\rho_i,H_i)I_n(\epsilon_n\rho_e,H_e)} \tag{4.87}$$

Therefore, Eq. (4.73) becomes:

$$\begin{aligned}\tilde{u}_{nh}(r,n) &= D_n J_n(\epsilon_n r) + E_n Y_n(r\epsilon_n r) \\ &= \frac{\widetilde{K}_{e_n} Y_n(\epsilon_n \rho_i, H_i) - \widetilde{K}_{i_n} Y_n(\epsilon_n \rho_e, H_e)}{I_n(\epsilon_n \rho_e, H_e) Y_n(\epsilon_n \rho_i, H_i) - I_n(\epsilon_n \rho_i, H_i) Y_n(\epsilon_n \rho_e, H_e)} J_n(\epsilon_n r) \\ &+ \frac{\widetilde{K}_{e_n} I_n(\epsilon_n \rho_i, H_i) - \widetilde{K}_{i_n} I_n(\epsilon_n \rho_e, H_e)}{Y_n(\epsilon_n \rho_e, H_e) I_n(\epsilon_n \rho_i, H_i) - Y_n(\epsilon_n \rho_i, H_i) I_n(\epsilon_n \rho_e, H_e)} Y_n(\epsilon_n r)\end{aligned} \tag{4.88}$$

Finally, by applying the Inverse Fourier Transform, it is possible to determine the sought quasi steady-state solution in the following discrete representation:

$$\begin{aligned}\tilde{u}_{nh}(r,\theta) &= \frac{1}{2\pi} \sum_{n=0}^{\infty} \delta_n \, Re\left[\tilde{u}(r,n)\, e^{jn\theta}\right] \\ &= \frac{1}{2\pi} \sum_{n=0}^{\infty} \delta_n \, Re\left[\left(D_n J_n(\epsilon_n r) + E_n Y_n(r\epsilon_n r)\right) e^{jn\theta}\right]\end{aligned} \tag{4.89}$$

where $\delta_n = \begin{cases} 1 & n = 0 \\ 2 & n \neq 0 \end{cases}$.

Since for $n = 0$

$$Y_0(0,H) = \left(\frac{0}{r} + H\right) Y_0(0) - 0 Y_{n+1}(0) = H \cdot (-\infty) - 0 \cdot (-\infty) \tag{4.90}$$

is undetermined, the solution in this case will be achieved by solving Eq. (4.71) for $n = 0$

$$\frac{\partial^2 \tilde{u}_{nh}}{\partial r^2} + \frac{1}{r} \frac{\partial \tilde{u}_{nh}}{\partial r} = 0 \tag{4.91}$$

under the following boundary conditions:

$$\frac{d}{dr}\, \tilde{u}_{nh}(\rho_e, 0) + H_e \tilde{u}_{nh}(\rho_e, 0) = \widetilde{K}_{e,0} \tag{4.92}$$

$$\frac{d}{dr}\, \tilde{u}_{nh}(\rho_i, 0) + H_i \tilde{u}_{nh}(\rho_i, 0) = \widetilde{K}_{i,0} \tag{4.93}$$

Basically, the problem to be solved is an ODE, and its solution takes the following form [19]:

$$\tilde{u}_{nh}(r,0) = \tilde{\beta}\, ln\, r + \tilde{\gamma} \tag{4.94}$$

By imposing the boundary conditions, the solution becomes:

$$\tilde{\beta} = \frac{\rho_e \rho_i \left(\widetilde{K}_{e,0} H_i - \widetilde{K}_{i,0} H_e\right)}{\rho_i H_i (1 + H_e \rho_e ln\, \rho_e) - \rho_e H_e (1 + H_i \rho_i ln\, \rho_i)} \tag{4.95}$$

$$\tilde{\gamma} = \frac{\rho_i \widetilde{K}_{i,0} (1 + H_e \rho_e ln\, \rho_e) - \rho_e \widetilde{K}_{e,0} (1 + H_i \rho_i ln\, \rho_i)}{\rho_i H_i (1 + H_e \rho_e ln\, \rho_e) - \rho_e H_e (1 + H_i \rho_i ln\, \rho_i)} \tag{4.96}$$

Hence:

$$\tilde{u}(r,0) = \frac{\rho_e\rho_i\left(\widetilde{K}_{e,0}H_i - \widetilde{K}_{i,0}H_e\right)}{\rho_i H_i(1+H_e\rho_e ln\,\rho_e) - \rho_e H_e(1+H_i\rho_i ln\,\rho_i)} ln\, r + \frac{\rho_i\widetilde{K}_{i,0}(1+H_e\rho_e ln\,\rho_e) - \rho_e\widetilde{K}_{e,0}(1+H_i\rho_i ln\,\rho_i)}{\rho_i H_i(1+H_e\rho_e ln\,\rho_e) - \rho_e H_e(1+H_i\rho_i ln\,\rho_i)} \quad (4.97)$$

Appling the Inverse Fourier Transform and remembering that for $n = 0$:

$$\widetilde{K}_{e,0} = 2\pi H_e u_{\infty,e} + 2\varphi_0 Q_e \quad (4.98)$$

$$\widetilde{K}_{i,0} = 2\pi H_i u_{\infty,i} \quad (4.99)$$

The quasi steady-state solution in a discrete representation can be rewritten as follows:

$$u_{nh}(r,\theta) = \frac{1}{2\pi}\sum_{n=1}^{\infty}\delta_n Re\left[\tilde{u}_{nh}(r,n)\, e^{jn\theta}\right] = \beta\, ln\, r + \gamma + \frac{1}{\pi}\sum_{n=1}^{\infty} Re\left[\left(D_n J_n(\epsilon_n r) + E_n Y_n(r\epsilon_n r)\right) e^{jn\theta}\right] \quad (4.100)$$

where $\delta_n = \begin{cases} 1 & n = 0 \\ 2 & n \neq 0 \end{cases}$ and:

$$\beta = \frac{\tilde{\beta}}{2\pi}\, e^0 = \frac{\rho_e\rho_i H_i\left(\left(H_e u_{\infty,e} + \frac{\varphi_0}{\pi}Q_e\right) - H_e u_{\infty,i}\right)}{\rho_i H_i(1+H_e\rho_e ln\,\rho_e) - \rho_e H_e(1+H_i\rho_i ln\,\rho_i)} \quad (4.101)$$

$$\gamma = \frac{\tilde{\gamma}}{2\pi}\, e^0 = \frac{\rho_i H_i u_{\infty,i}(1+H_e\rho_e ln\,\rho_e) - \rho_e\left(H_e u_{\infty,e} + \frac{\varphi_0}{\pi}Q_e\right)(1+H_i\rho_i ln\,\rho_i)}{\rho_i H_i(1+H_e\rho_e ln\,\rho_e) - \rho_e H_e(1+H_i\rho_i ln\,\rho_i)} \quad (4.102)$$

4.3.2.2. Solution of the transient problem (homogeneous boundary condition)

The mathematical formulation of the transient problem is given as:

$$\frac{1}{r}\frac{\partial u_h}{\partial r} + \frac{\partial^2 u_h}{\partial r^2} + \frac{1}{r^2}\frac{\partial^2 u_h}{\partial\theta^2} = \frac{\omega}{\alpha}\frac{\partial u_h}{\partial\theta} + \frac{1}{\alpha}\frac{\partial u_h}{\partial t} \quad (4.103)$$

under conditions:

IC: $u_h(t=0) = f_h(r,\theta) = f(r,\theta) - u_{nh}(r,\theta)$

BC1: $\left.\frac{\partial u_h}{\partial r}\right|_{r=\rho} = \begin{cases} 0, & -\varphi_0 \le \theta \le \varphi_0 \\ -Hu_h|_{r=\rho_e}, & \varphi_0 \le \theta \le 2\pi - \varphi_0 \end{cases}$

BC2: $\left.\frac{\partial u_h}{\partial r}\right|_{r=0} = -Hu_h|_{r=\rho_i}$

BC4 (periodicity): $\left.\frac{\partial u_h}{\partial\theta}\right|_{\theta=0} = \left.\frac{\partial u_h}{\partial\theta}\right|_{\theta=2\pi}, \quad \rho_i \le r \le \rho_e$

$u_h|_{\theta=0} = u_h|_{\theta=2\pi},$

By applying a separation of variables in the form:

$$u_h(r,\theta,t) = v(r,\theta)T(t) \tag{4.104}$$

Eq. (4.104) becomes:

$$\frac{T}{r}\frac{\partial v}{\partial r} + T\frac{\partial^2 v}{\partial r^2} + \frac{T}{r^2}\frac{\partial^2 v}{\partial \theta^2} - \frac{\omega T}{\alpha}\frac{\partial v}{\partial \theta} = \frac{v}{\alpha}\frac{dT}{dt} \tag{4.105}$$

As stated earlier, the only way to satisfy this equality is to equate each group of functions to an arbitrary separation constant $-\lambda^2$. Eq. (4.105) leads then to two separate differential equations. The first one is time dependent only:

$$\frac{dT}{dt} + \alpha\lambda^2 T = 0 \tag{4.106}$$

and the second one is space dependent only:

$$r\frac{\partial v}{\partial r} + r^2\frac{\partial^2 v}{\partial r^2} + \frac{\partial^2 v}{\partial \theta^2} - \frac{\omega r^2}{\alpha}\frac{\partial v}{\partial \theta} + (\lambda r)^2 v = 0 \tag{4.107}$$

under boundary conditions:

BC1: $$\left.\frac{\partial v}{\partial r}\right|_{r=\rho} = \begin{cases} 0, & -\varphi_0 \le \theta \le \varphi_0 \\ -Hu_h|_{r=\rho_e}, & \varphi_0 \le \theta \le 2\pi - \varphi_0 \end{cases}$$

BC2: $$\left.\frac{\partial v}{\partial r}\right|_{r=0} = -Hu_h|_{r=\rho_i}$$

BC3: $$\lim_{r\to 0} v(r) \neq \pm\infty$$

BC4 (periodicity): $$\left.\frac{\partial u_h}{\partial \theta}\right|_{\theta=0} = \left.\frac{\partial u_h}{\partial \theta}\right|_{\theta=2\pi}, \quad \rho_i \le r \le \rho_e$$

$$u_h|_{\theta=0} = u_h|_{\theta=2\pi},$$

Eq. (4.106) displays the general solution:

$$T(t) = Ae^{-\alpha\lambda^2 t} \tag{4.108}$$

To find a solution of Eq. (4.107), the following integral Fourier transform can be used:

$$\tilde{v}(r,n) = \int_{-\pi}^{\pi} v(r,\theta)e^{-jn\theta}d\theta \tag{4.109}$$

Given the properties of Fourier transforms and by taking into account the periodicity conditions, Eq. (4.107) becomes:

$$r\frac{\partial \tilde{v}}{\partial r} + r^2\frac{\partial^2 \tilde{v}}{\partial r^2} + \left(\left(\lambda^2 - j\frac{n\omega}{\alpha}\right)r^2 - n^2\right)\tilde{v} = 0 \tag{4.110}$$

under boundary conditions:

BC1: $$\left.\frac{\partial \tilde{v}}{\partial r}\right|_{r=\rho} = -H_e \int_{-\pi}^{\pi} \tilde{v}|_{r=\rho_e} e^{-jn\theta} d\theta = -H_e \tilde{v}(\rho_e, n)$$

BC2: $$\left.\frac{\partial \tilde{v}}{\partial r}\right|_{r=0} = -H_i \int_{-\pi}^{\pi} \tilde{v}|_{r=\rho_i} e^{-jn\theta} d\theta = -H_i \tilde{v}(\rho_i, n)$$

BC3: $$\lim_{r \to 0} \tilde{v}(r) \neq \pm\infty$$

Eq. (4.110) represents a particular case of the Bessel equation. Its solution is a Bessel function of order n with argument characterized by an imaginary quantity. By defining:

$$\Lambda = \sqrt{\lambda^2 - j\frac{n\omega}{\alpha}} \qquad (4.111)$$

the solution of Eq. (4.110) is the following:

$$\tilde{v}\big(r, \Lambda(n,\lambda)\big) = B_n J_n(r\Lambda) + C_n Y_n(r\Lambda) \qquad (4.112)$$

where B_n and C_n are constants.

The application of the Fourier transform allowed to split the problem into *n* subproblems, each one characterized by a specific frequency. Then, the solution of the problem comes from the solutions of each subproblem. This means that for each value of n, there is a unique set of eigenvalues $\lambda_1, \lambda_2, \ldots, \lambda_m$, due to Bessel function's oscillatory behavior. So, Eq. (4.111) can be rewritten as:

$$\Lambda_{mn} = \sqrt{\lambda_{mn}^2 - j\frac{n\omega}{\alpha}} \qquad (4.113)$$

where index m spans the eigenvalues in the Bessel expansion and index n spans the frequencies in the Fourier expansion.

To solve each subproblem, a solution procedure might be detected by analyzing the simplest case, namely that relating to the null frequency $n = 0$. In that case, the mathematical formulation of the homogeneous problem is given as:

$$\frac{\partial^2 \tilde{v}_0}{\partial r^2} + \frac{1}{r}\frac{\partial \tilde{v}_0}{\partial r} + \lambda_{m0}^2 \tilde{v}_0 = 0 \qquad (4.114)$$

under conditions:

BC1: $$\left.\frac{\partial \tilde{v}_0}{\partial r}\right|_{r=\rho_e} + H_e \tilde{v}_0|_{r=\rho_e} = 0$$

BC2: $$\left.\frac{\partial \tilde{v}_0}{\partial r}\right|_{r=\rho_i} + H_e \tilde{v}_0|_{r=\rho_i} = 0$$

Eq. (4.114) represents a Bessel equation of order zero. Its solution is:

$$\tilde{v}_0(r) = B_0 J_0(\lambda r) + C_0 Y_0(\lambda r) \tag{4.115}$$

where B_0 and C_0 are known unless for a proportionality factor. In light of Bessel function derivative rules (see Appendix D) and substituting Eq. (4.115) into the boundary conditions, one obtains the following 2×2 homogeneous system of equations in the unknowns B_0 and C_0:

$$\begin{aligned}\begin{bmatrix} A_{11} & A_{12} \\ A_{21} & A_{22} \end{bmatrix}\begin{bmatrix} B_0 \\ C_0 \end{bmatrix} &= \begin{bmatrix} H_e J_0(\lambda\rho_e) - \lambda J_1(\lambda\rho_e) & H_e Y_0(\lambda\rho_e) - \lambda Y_1(\lambda\rho_e) \\ H_i J_0(\lambda\rho_i) - \lambda J_1(\lambda\rho_i) & H_i Y_0(\lambda\rho_i) - \lambda Y_1(\lambda\rho_i) \end{bmatrix}\begin{bmatrix} B_0 \\ C_0 \end{bmatrix} \\ &= \begin{bmatrix} 0 \\ 0 \end{bmatrix}\end{aligned} \tag{4.116}$$

By the singularity of the 2×2 matrix in Eq. (4.116), the eigenvalues λ_m of solution representation (4.115) may be obtained for non-trivial solutions $B_0 \neq 0$, $C_0 \neq 0$ as:

$$\begin{aligned}&\big(H_e Y_0(\lambda\rho_e) - \lambda Y_1(\lambda\rho_e)\big)\big(H_i J_0(\lambda\rho_i) - \lambda J_1(\lambda\rho_i)\big) \\ &\quad - \big(H_i Y_0(\lambda\rho_i) - \lambda Y_1(\lambda\rho_i)\big)\big(H_e J_0(\lambda\rho_e) - \lambda J_1(\lambda\rho_e)\big) = 0\end{aligned} \tag{4.117}$$

which generates eigenvalues λ_m, with $m = 1, 2, 3, \ldots$.

Thus, the sought solution $R(\lambda_m r)$ becomes a function also of the eigenvalues λ_m. To determine its expression, it is possible to proceed as follows. From Eq. (4.116), when Eq. (4.117) holds, the solution in terms of the ratio C_0/B_0 can be obtained as:

$$\begin{aligned}\frac{C_0}{B_0} &= -\frac{H_e J_0(\lambda_m\rho_e) - \lambda_m J_1(\lambda_m\rho_e)}{H_e Y_0(\lambda_m\rho_e) - \lambda_m Y_1(\lambda_m\rho_e)} = -\frac{H_i J_0(\lambda_m\rho_i) - \lambda_m J_1(\lambda_m\rho_i)}{H_i Y_0(\lambda_m\rho_i) - \lambda_m Y_1(\lambda_m\rho_i)} \\ &= -\frac{A_{21}+A_{11}}{A_{22}+A_{12}}\end{aligned} \tag{4.118}$$

from which it is possible to rewrite the solution $R(\lambda_m r)$ in the following form [64]:

$$\begin{aligned}R(\lambda_m r) &= [A_{22}+A_{12}]J_0(\lambda_m r) - [A_{21}+A_{11}]Y_0(\lambda_m r) = \\ &= [H_i Y_0(\lambda\rho_i) - \lambda Y_1(\lambda\rho_i) + H_e Y_0(\lambda\rho_e) - \lambda Y_1(\lambda\rho_e)]J_0(\lambda_m r) \\ &\quad - [H_i J_0(\lambda\rho_i) - \lambda J_1(\lambda\rho_i) + H_e J_0(\lambda\rho_e) - \lambda J_1(\lambda\rho_e)]Y_0(\lambda_m r)\end{aligned} \tag{4.119}$$

$$\tilde{v}_0(r, 0) = \sum_{m=1}^{\infty} B_{m0} J_0(\lambda_m r) + C_{m0} Y_0(\lambda_m r) \tag{4.120}$$

The case with $n > 0$ now follows. It is possible to rewrite Eq. (4.110) as follows:

$$r\frac{\partial}{\partial r}\tilde{v}_n + r^2\frac{\partial^2}{\partial r^2}\tilde{v}_n + \left(\left({\lambda_{mn}}^2 - j\frac{n\omega}{\kappa}\right)r^2 - n^2\right)\tilde{v}_n = 0 \tag{4.121}$$

or:

$$r\frac{\partial}{\partial r}\tilde{v}_n + r^2\frac{\partial^2}{\partial r^2}\tilde{v}_n + \left(\Lambda_{mn}{}^2 r^2 - n^2\right)\tilde{v}_n = 0 \tag{4.122}$$

with boundary conditions:

$$\frac{\partial}{\partial r}\tilde{v}_n(\rho_e) + H_e\tilde{v}_n(\rho_e) = 0 \tag{4.123}$$

$$\frac{\partial}{\partial r}\tilde{v}_n(\rho_i) + H_i\tilde{v}_n(\rho_i) = 0 \tag{4.124}$$

The eigenvalues λ_{mn} are the roots of the following equation, with Λ_{mn} given by Eq. (4.113):

$$\begin{aligned}\left(H_e Y_n(\Lambda\rho_e) - \lambda Y_{n+1}(\Lambda\rho_e)\right)\left(H_i J_n(\Lambda\rho_i) - \lambda J_{n+1}(\Lambda\rho_i)\right)\\ - \left(H_i Y_n(\Lambda\rho_i) - \lambda Y_{n+1}(\Lambda\rho_i)\right)\left(H_e J_n(\Lambda\rho_e) - \lambda J_{n+1}(\Lambda\rho_e)\right) = 0\end{aligned} \tag{4.125}$$

Then, the general solution is formed by the summation over all boundary value problem solutions:

$$\tilde{v}(r,n) = \sum_{m=1}^{\infty} B_{mn}J_n(\Lambda_{mn}r) + C_{mn}Y_n(\Lambda_{mn}r) \tag{4.126}$$

Therefore, each solution of the n subproblems ($\tilde{v}(r,n)$) in which the problem was split has been determined.

To go back to the original variable v, the inverse integral Fourier transform must be applied. That allows to get the solution for the radial and angular dependent problem:

$$\begin{aligned}v(r,\theta) &= \frac{1}{2\pi}\sum_{n=0}^{\infty}\delta_n Re\left[\tilde{v}(r,n)e^{jn\theta}\right]\\ &= \frac{1}{2\pi}\sum_{n=0}^{\infty}\delta_n\sum_{m=1}^{\infty}Re\left([B_{mn}J_n(\Lambda_{mn}r) + C_{mn}Y_n(\Lambda_{mn}r)]e^{jn\theta}\right)\end{aligned} \tag{4.127}$$

where $\delta_n = \begin{cases}1 & n = 0\\ 2 & n \neq 0\end{cases}$.

Next, the complete solution is obtained by multiplying the solution independent on time with the one dependent on time, hence:

$$u_h(r,\theta,t) = \frac{1}{2\pi}\sum_{n=0}^{\infty}\delta_n\sum_{m=1}^{\infty}Re\left(R_{mn}(\Lambda_{mn}r)e^{jn\theta}\right)A_{mn}e^{-\alpha\lambda_{mn}{}^2 t} \tag{4.128}$$

where:

$$R_{mn}(\Lambda_{mn}r) = B_{mn}J_n(\Lambda_{mn}r) + C_{mn}Y_n(\Lambda_{mn}r) \tag{4.129}$$

To determine the A_{mn} values, the initial condition must be applied (see Appendix C). However, since the boundary conditions are non-homogeneous, the steady-state solution $u_{nh}(r,\theta)$ must be subtracted from the initial condition $f(r,\theta)$, namely:

$$f_h(r,\theta) = f(r,\theta) - u_{nh}(r,\theta) \tag{4.130}$$

So, by applying the initial condition $f_h(r,\theta)$ to the found complete solution, it follows that:

$$f_h(r,\theta) = \frac{1}{2\pi}\sum_{n=0}^{\infty}\delta_n \sum_{m=1}^{\infty} Re\left(R_{mn}(\Lambda_{mn}r)e^{jn\theta}\right)A_{mn} \tag{4.131}$$

The previous formula can be considered as a Fourier series, so, for the properties of Fourier series, the unknown coefficients A_{mn} can be evaluated as:

$$\frac{1}{2\pi}\int_{-\pi}^{\pi} f_h e^{-jn\theta}\,d\theta = \frac{1}{2\pi}\sum_{m=1}^{\infty} Re\left(R_{mn}(\Lambda_{mn}r)e^{jn\theta}\right)A_{mn} \tag{4.132}$$

For the properties of Fourier-Bessel series, multiplying both sides by $\int_{\rho_i}^{\rho_e} rR_{mn}(r\Lambda_{mn})\,dr$, the previous formula can be further reduced to:

$$\begin{aligned}\int_{\rho_i}^{\rho_e}\left(\int_{-\pi}^{\pi} f_h e^{-jn\theta}\,d\theta\right) rR_{mn}(\Lambda_{mn}r)dr \\ = \int_{\rho_i}^{\rho_e}\left[\sum_{m=1}^{\infty} Re\left(R_{mn}(\Lambda_{mn}r)e^{jn\theta}\right)A_{mn}\right] rR_{mn}(\Lambda_{mn}r)\,dr\end{aligned} \tag{4.133}$$

$$\int_{\rho_i}^{\rho_e}\left(\int_{-\pi}^{\pi} f_h e^{-jn\theta}\,d\theta\right) rR_{mn}(\Lambda_{mn}r)dr = A_{mn}\left[\int_{\rho_i}^{\rho_e} r\left[Re\left(R_{mn}(\Lambda_{mn}r)\right)\right]^2 dr\right] \tag{4.134}$$

$$A_{mn} = \frac{\int_{\rho_i}^{\rho_e}\left(\int_{-\pi}^{\pi} f_h e^{-jn\theta}\,d\theta\right) rR_{mn}(\Lambda_{mn}r)dr}{\int_{\rho_i}^{\rho_e} r\left[Re\left(R_{mn}(\Lambda_{mn}r)\right)\right]^2 dr} \tag{4.135}$$

The integral at the numerator can be evaluated numerically, as:

$$\begin{aligned}&\int_{\rho_i}^{\rho_e}\left(\int_{-\pi}^{\pi} f_h(r,\theta)e^{-jn\theta}\,d\theta\right) rR_{mn}(\Lambda_{mn}r)dr \\ &= \int_{\rho_i}^{\rho_e}\left(\int_{-\pi}^{\pi}\left(f(r,\theta) - u_{nh}(r,\theta)\right)e^{-jn\theta}\,d\theta\right) rR_{mn}(\Lambda_{mn}r)dr \\ &= \int_{\rho_i}^{\rho_e}\left(\int_{-\pi}^{\pi} f(r,\theta)e^{-jn\theta}\,d\theta\right. \\ &\left. - \int_{-\pi}^{\pi} u_{nh}(r,\theta)e^{-jn\theta}\,d\theta\right) rR_{mn}(\Lambda_{mn}r)dr\end{aligned} \tag{4.136}$$

Being:

$$\tilde{u}_{nh}(r,n) = \int_{-\pi}^{\pi} u_{nh}(r,\theta) e^{-jn\theta} d\theta \tag{4.137}$$

Eq. (4.137) can be rewritten as:

$$\int_{\rho_i}^{\rho_e} \left[\left(\int_{-\pi}^{\pi} f(r,\theta) e^{-jn\theta} d\theta \right) - \tilde{u}_{nh}(r,n) \right] r R_{mn}(\Lambda_{mn} r) dr \tag{4.138}$$

For the particular case $f(r,\theta) = f_0 = const$ or $f(r,\theta) = f_0(r)$, the integral at the numerator becomes for $n = 0$:

$$\begin{aligned} &\int_{\rho_i}^{\rho_e} \left[\left(\int_{-\pi}^{\pi} f(r,\theta) e^{-jn\theta} d\theta \right) - \tilde{u}_{nh}(r,n) \right] r R_{m0}(\lambda_m r) dr \\ &\qquad = \int_{\rho_i}^{\rho_e} \big(2\pi f_0(r) - \tilde{u}_{nh}(r,0) \big) r R_{m0}(\lambda_m r) dr \end{aligned} \tag{4.139}$$

$$A_{m0} = \frac{\int_{\rho_i}^{\rho_e} \big(2\pi f_0(r) - \tilde{u}(r,0) \big) r R_{m0}(\lambda_m r) dr}{\int_{\rho_i}^{\rho_e} r \big(R_{m0}(\lambda_m r) \big)^2 dr} \tag{4.140}$$

Otherwise, for $n > 0$:

$$\int_{-\pi}^{\pi} f_n(r) e^{-jn\theta} d\theta = f_n(r) \int_{-\pi}^{\pi} e^{-jn\theta} d\theta = 0 \tag{4.141}$$

being $e^{-jn\theta}$ a periodic function such as $\int_{-\pi}^{\pi} e^{-jn\theta} d\theta = 0$. Thus:

$$A_{mn} = \frac{\int_{\rho_i}^{\rho_e} \big(\tilde{u}(r,0) \big) r R_{mn}(\lambda_m r) dr}{\int_{\rho_i}^{\rho_e} r \big[Re\big(R_{mn}(\Lambda_{mn} r) \big) \big]^2 dr} \tag{4.142}$$

The problem exact solution is given, hence, by the following equation:

$$\begin{aligned} u(r,\theta,t) &= u_{nh}(r,\theta) + u_h(r,\theta,t) \\ &= \beta \ln r + \gamma + \frac{1}{\pi} \sum_{n=1}^{\infty} Re\big[\big(D_n J_n(\epsilon_n r) + E_n Y_n(r\epsilon_n r) \big) e^{jn\theta} \big] \\ &\quad + \frac{1}{2\pi} \sum_{n=0}^{\infty} \delta_n \sum_{m=1}^{\infty} Re\big(R_{mn}(\Lambda_{mn} r) e^{jn\theta} \big) A_{mn} e^{-\alpha \lambda_{mn}{}^2 t} \end{aligned} \tag{4.143}$$

4.4. Approximate analytical solution

Even though the achieved solutions of the heat conduction problem are exact (except for approximations by truncation), they cannot be used effectively for the following inverse analysis. This mainly because the computational time required by both Eqs. (4.66) and (4.143) is excessive for any iterative inverse analysis algorithm. Secondly, this solution was attained for an idealized problem under conditions a bit far from real ones. For these reasons, the solution is first approximated to assure a tolerable computational time. Then, it is adapted to mimic the real testing conditions.

4.4.1. Analytical model approximation for the ring-on-ring tribometer context

As done before, the solution is approximated first for the case of a solid cylinder and, then, the approximation is extended to the hollow cylinder case.

4.4.1.1. Solid cylinder

In a ring-on-ring tribometer test, it is worth mentioning that the contact zone between the rings, namely the opening arc where the conduction heat transfer takes place, is very narrow and the flash temperature effect arising in such a contact zone is very localized. Therefore, the steady-state solution with $n = 0$ given by Eq. (4.26) could be considered as representative of the mean value of the temperature along the circumferential border of the rings:

$$u_{nh}(r)|_{n=0} \approx \frac{1}{2\pi}\frac{\rho\left(\tilde{K}_n + \tilde{Q}_n\right)}{(n+H\rho)J_n(\rho\epsilon_n) - \epsilon_n\rho J_{n+1}(\rho\epsilon_n)}J_n(\epsilon_n r) = \frac{Hu_\infty + \frac{\varphi_0}{\pi}Q_e}{H} = u_\infty + \frac{\varphi_0}{\pi}\frac{Q_e}{H} \quad (4.144)$$

Such assumption allows to simplify the solution of the problem. In fact, if the steady-state solution is dependent only on the radius of the cylinder, the initial condition to be applied to the homogeneous associated problem becomes:

$$f_h(r) = f_0(r) - u_{nh}(r)|_{n=0} \quad (4.145)$$

and the constants:

$$A_{mn} = \frac{\int_0^{\rho}\left(\int_{-\pi}^{\pi} f_h e^{-jn\theta} d\theta\right) r J_n(r\Lambda) dr}{Re\left[\int_0^{\rho} r J_n(r\Lambda)^2 dr\right]} \tag{4.146}$$

could be determined by the formulas below. For $n = 0$:

$$\int_0^{\rho}\left(\int_{-\pi}^{\pi} f_0(r)e^{-jn\theta} - u_{nh}(r)|_{n=0} d\theta\right) r J_0(r\Lambda) dr = \int_0^{\rho} 2\pi (f_0(r) - u_{nh}(r)|_{n=0}) r J_0(r\Lambda) dr \tag{4.147}$$

$$A_{m0} = \frac{\int_0^{\rho} 2\pi (f_0(r) - u_{nh}(r)|_{n=0}) r J_0(r\Lambda) dr}{\rho\Lambda[J_0(\Lambda_{mn}\rho)^2 + J_1(\Lambda_{mn}\rho)^2]} \tag{4.148}$$

and for $n > 0$:

$$\int_{-\pi}^{\pi} f_0(r)e^{-jn\theta} d\theta = f_0(r)\int_{-\pi}^{\pi} e^{-jn\theta} d\theta = 0 \tag{4.149}$$

$$\int_{-\pi}^{\pi} u_{nh}(r)e^{-jn\theta} d\theta = u_{nh}(r)\int_{-\pi}^{\pi} e^{-jn\theta} d\theta = 0 \tag{4.150}$$

being $e^{-jn\theta}$ a periodic function such as $\int_{-\pi}^{\pi} e^{-jn\theta} d\theta = 0$.

One obtains:

$$\int_0^{\rho}\left(\int_{-\pi}^{\pi} f_0(r)e^{-jn\theta} d\theta - u_{nh}(r)|_{n=0}\right) r J_0(r\Lambda) dr = 0 \tag{4.151}$$

and, finally:

$$A_{mn} = \frac{\int_0^{\rho}\left(\int_{-\pi}^{\pi} f_h e^{-jn\theta} d\theta\right) r J_n(r\Lambda) dr}{Re\left[\int_0^{\rho} r J_n(r\Lambda)^2 dr\right]} = 0 \tag{4.152}$$

The complete solution is hence composed by the quasi steady-state solution and the transient solution for a steady-state condition uniformly distributed along the border:

$$u(r,\theta,t) = u_{nh}(r,\theta) + u_h(r,\theta,t) = \frac{1}{2\pi}\sum_{n=0}^{\infty}\gamma_n Re\left[E_n J_n(r\Lambda_{0n})e^{jn\theta}\right] + \sum_{m=1}^{\infty}\left[A_{m0}J_0(r\Lambda)e^{-\lambda_{m0}{}^2\kappa t}\right] \tag{4.153}$$

This is rewritable as:

$$u(r,\theta,t) = u_{\infty} + \frac{\varphi_0}{\pi}\frac{Q_e}{H} \tag{4.154}$$

$$+\frac{1}{\pi}\sum_{n=1}^{\infty} Re\left[\frac{\rho\left(\overline{K}_{e_n}+\overline{Q_{e_n}}\right)}{[(n\Lambda_{0n}+H_e\rho)J_n(\rho\Lambda_{0n})-\rho\Lambda_{0n}J_{n+1}(\rho\Lambda_{0n})]}J_n(r\Lambda_{0n})e^{jn\theta}\right]$$

$$+\sum_{m=1}^{\infty}\left[\frac{2[f_0(r)-u_{nh}(r)|_{n=0}]\frac{\rho}{\Lambda}J_1(\rho\Lambda)}{\rho^2[J_0(\Lambda_{mn}\rho)^2+J_1(\Lambda_{mn}\rho)^2]}J_0(r\Lambda)e^{-\alpha\lambda_{mn}{}^2t}\right]$$

A comparison between exact Eq. (4.66) and approximate Eq. (4.154) solutions can be appreciated in Figure 4.3 and Table 4-1. The picture shows a very good agreement between the two solutions, and the table indicates that the required time is three orders of magnitude lower for the approximate solution. This simplification allows for a considerable saving in computational time.

Time required for 1 s of test simulation	
Exact solution	***Approximate solution***
4.55 *s*	0.05 *s*

Table 4-1: Comparison between required computational times.

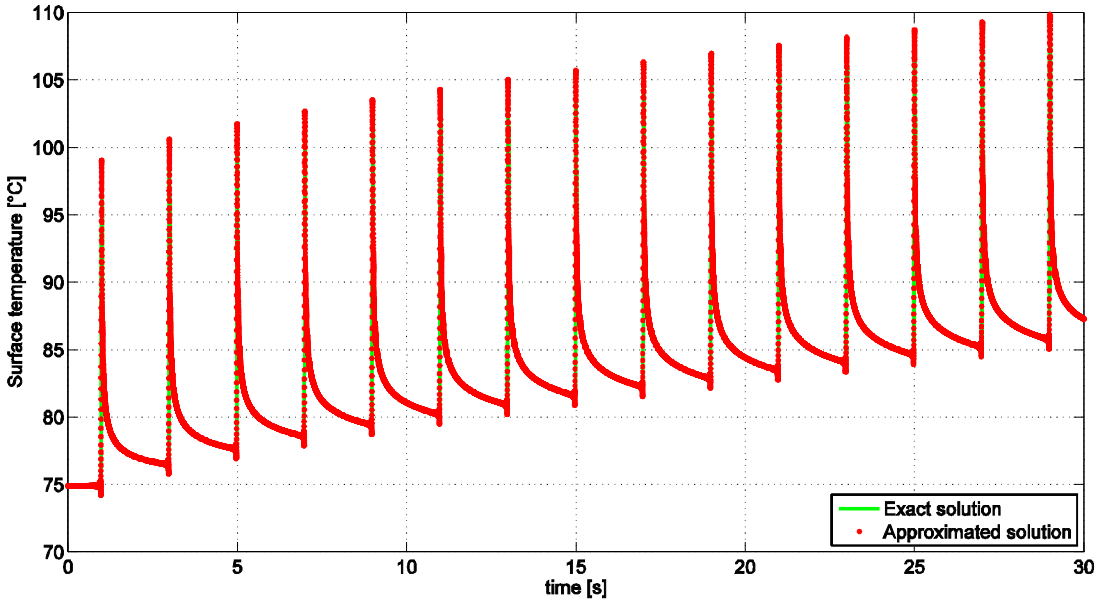

Figure 4.3: Comparison between exact solution and approximate solution.

4.4.1.2. Hollow cylinder

As done for the solid cylinder problem, due to the non-homogeneous boundary conditions BC1 and BC2, the solution of the present problem can be obtained by superposition of the steady-state solution with non-homogeneous boundary condition $u_{nh}(r,\theta)$ and of the transient solution of the associated homogeneous problem $u_h(r,\theta,t)$ [45].

Since also in this case the contact zone is very narrow and differences between the flash temperature and the temperature of the external circumferential border are expected to be low, the same approximation introduced for the solid cylinder problem can be applied. This approximation allows to compute the temperature evolution simply by superimposing the quasi steady-state solution of the nonhomogeneous problem, to the transient solution of the (previously found) one-dimensional homogeneous problem, without significant loss of accuracy. Hence, the complete solution in simplified form can be represented as:

$$\begin{aligned} u(r,\theta,t) &= u_{nh}(r,\theta) + u_h(r,\theta,t) \\ &= \beta \ln r + \gamma + \frac{1}{\pi}\sum_{n=1}^{\infty} Re\left[\left(D_n J_n(\epsilon_n r) + E_n Y_n(\epsilon_n r)\right) e^{jn\theta}\right] \\ &+ \frac{1}{2\pi}\sum_{m=1}^{\infty} A_{m0}[D_{m0} J_0(\lambda_m r) + E_{m0} Y_0(\lambda_m r)] e^{-\alpha {\lambda_m}^2 t} \end{aligned} \qquad (4.155)$$

4.4.2. Analytical solution implementation

The analytical solution can be easily implemented through an appropriate environment for numerical computing. Indeed, typical numerical software allow to treat Bessel functions both with real arguments and with imaginary ones. For this work, the MATLAB environment was chosen for its reliability and flexibility and an original solution implementation was developed within it.

Even though the numerical implementation does not require a complex algorithm, quite a few troubles had to be solved. The main trouble consisted of finding the eigenvalues λ_m. These eigenvalues are the positive roots of the Bessel solution that satisfied the boundary conditions, namely a trascendental equation. However, the Bessel solution is an oscillating function because

is a composition of Bessel functions, which look roughly like oscillating sine or cosine functions that decay proportionally to $1/\sqrt{\epsilon r}$. Hence, once the first and the second roots were found, the other ones can be easily found by taking advantage of the solution oscillations, although their roots are not generally periodic, except asymptotically for a large ϵr. The first two roots can be found iteratively by means of the algorithms for minimization already available in the MATLAB environment.

Another trouble was due to the presence of two infinite sums in the analytical solution. Obviously, a series truncation is needed for the numerical implementation. For this reason, Eq. (4.154) becomes:

$$\begin{aligned} u(r,\theta,t) &= u_{nh}(r,\theta) + u_h(r,\theta,t) \\ &= \beta \ln r + \gamma + \frac{1}{\pi}\sum_{n=1}^{n_{max}} Re\left[\left(D_n J_n(\epsilon_n r) + E_n Y_n(r\epsilon_n r)\right) e^{jn\theta}\right] \\ &+ \frac{1}{2\pi}\sum_{m=1}^{m_{max}} A_{m0}[D_{m0}J_0(\lambda_m r) + E_{m0}Y_0(\lambda_m r)]e^{-\alpha{\lambda_m}^2 t} \end{aligned} \qquad (4.156)$$

Analysing the solution behavior at different truncation levels, for the first summation it was found that at least 200 elements are needed in order to reach a sufficiently smooth solution (Figure 4.4).

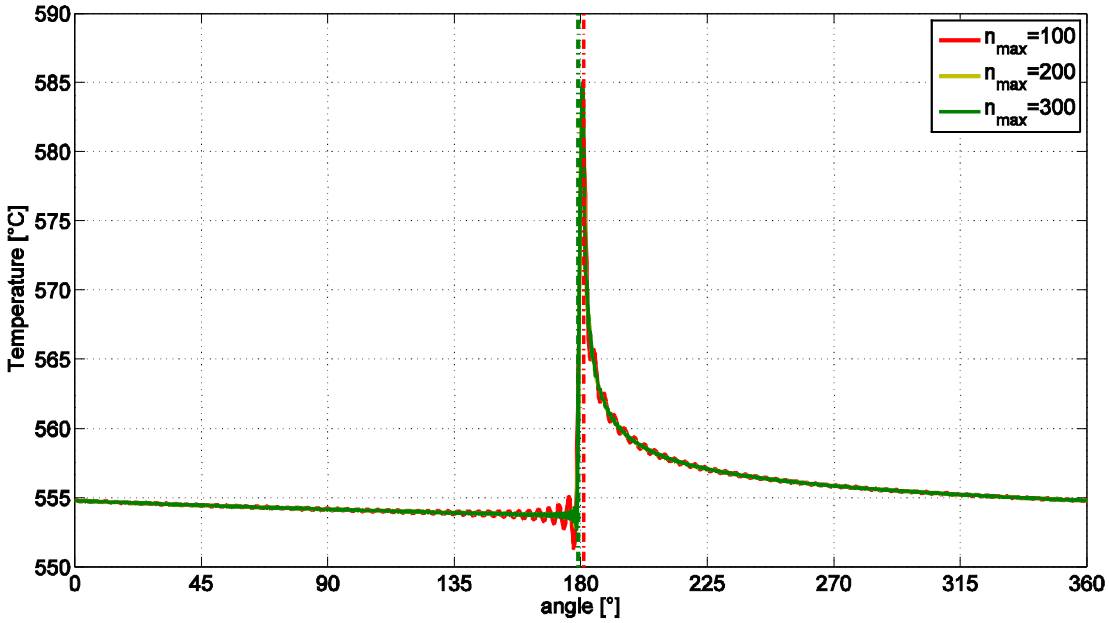

Figure 4.4: Quasi steady-state solution at different truncation levels.

Looking at Figure 4.5, it appears that for more than 200 elements only small improvements can be reached against the much more computational time required. This is confirmed by the fact that flash temperature estimation is only 1 °*C* more accurate moving from 200 elements to 300 elements.

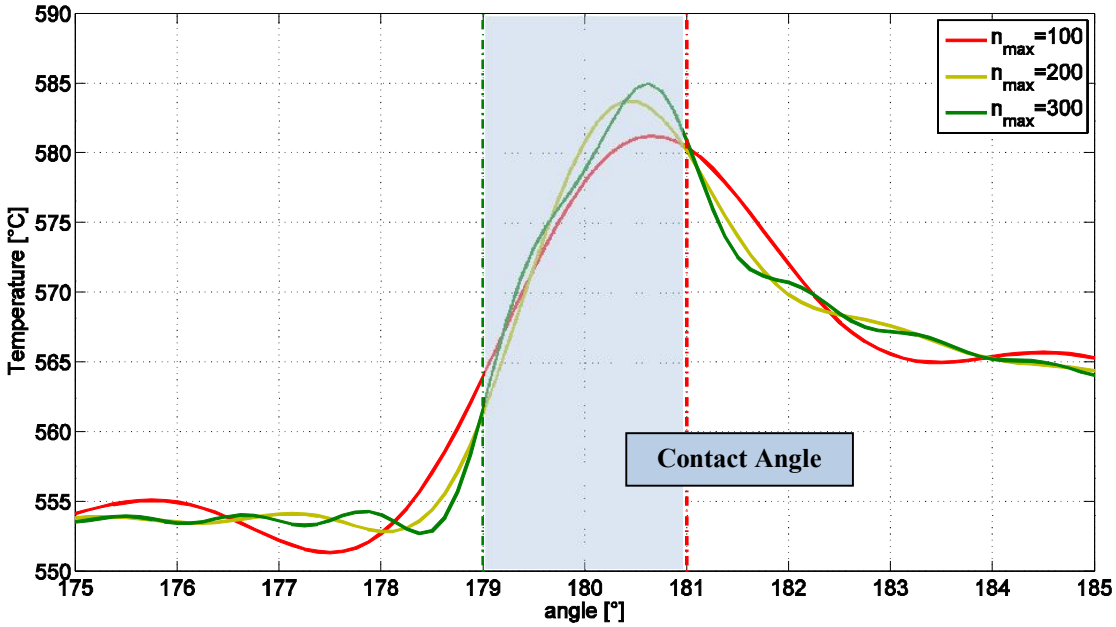

Figure 4.5: Detail of the flash temperature zone computed by the quasi steady-state solution at different truncation levels.

Instead, for the second summation, only three elements are sufficient. Plots in Figure 4.6 clearly show how, as the number of boundary value problem solutions considered in the summation increases, the truncation error decreases and the solution provides a better representation of the initial condition to be imposed. This is due to the present solving method, which uses the initial conditions to obtain generalized Fourier coefficients of the eigenfunction expansion (see Appendix C). However, by increasing the number of elements, very small improvement in the initial condition (less than 1 °C), but no improvement in the temperature evolution is detectable. Indeed, after the first seconds, solutions are completely overlapped.

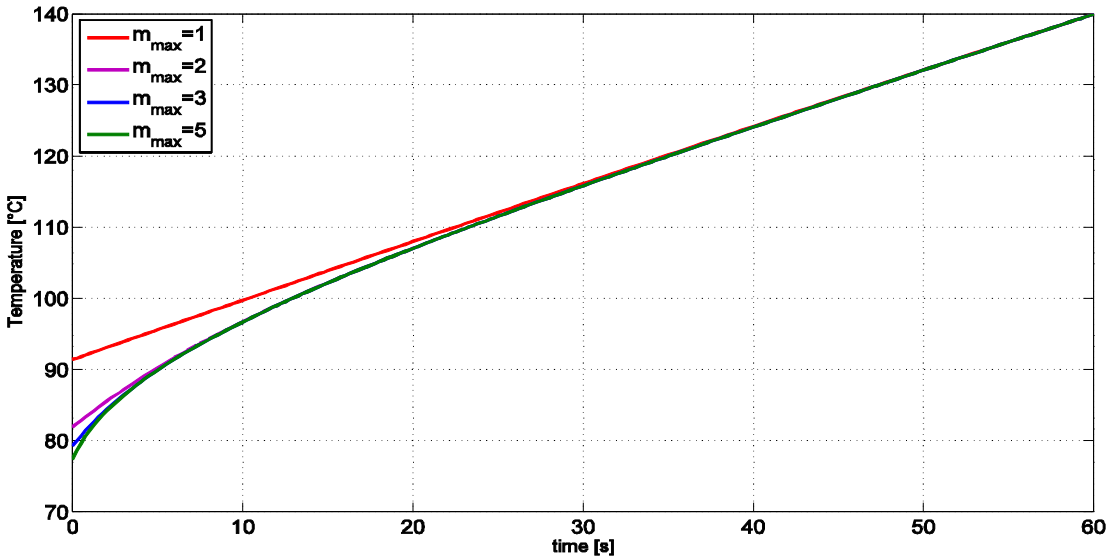

Figure 4.6: Transient solution at different truncation levels.

4.5. Numerical FEM solution and validation of the modelling approach

Analytical results were compared to the results coming from a Finite Element Method (FEM) solution, to verify the correctness and reliability of the derived solution. Moreover, the required computational time was detected, to evaluate the efficiency of the analytical solution.

4.5.1. FEM model implementation and simulations

A FEM model apt to solve the same heat transfer problem was developed within ABAQUS. A 2D model composed of a hollow disc whose geometrical dimensions are reported in Table 4-2, meshed with 7000 finite elements with 8 nodes was built to solve the same transient heat transfer problem. Material properties were considered constant along the simulation and equal to those of the analytical model. FEM model parameters are collected in Table 4-2. In the same way, initial and boundary conditions are the same as those applied to the analytical model. Internal and external convective boundary conditions were applied along all the circumferential border. Furthermore, a concentrated rotating heat flux was applied on the external arc segment.

This last boundary condition, which represents the heat exchanged by contact, has required a subroutine "DFLUX" implementation.

FEM model parameters				
Geometry	**Material**	**Initial Conditions**	**External b.c.**	**Internal b c.**
$\boldsymbol{\rho_e = 0.05\ m}$	$k = 45\ W/(°C\ m)$	$u_0 = 75\ °C.$	$u_e = 500\ °C$	$u_i = 50\ °C$
$\boldsymbol{\rho_i = 0.015\ m}$	$\rho = 7800\ kg/m^3$		$h_e = 1000\ W/(°C\ m^2)$	$h_i = 100\ W/(°C\ m^2)$
Contact angle $\boldsymbol{2\varphi_0 = 2°}$	$c = 450\ J/(°C\ kg)$		$q_e = 20\ MW/(m^2)$	

Table 4-2: FEM model parameters.

The ABAQUS solver is able to easily compute the temperature variation. However, it requires an appropriate selection of mesh size and time increment. In fact, the solution is strictly connected to these two parameters: if they are chosen in an unrefined way, the solution underestimates the temperature variation; if they are chosen in a too refined way, the solver requires an excessive time to compute the solution. In the present case, the mesh size and the time increment were chosen such that to guarantee an error on the temperature evolution of less than 1 °C and an error on the flash temperature estimation of less than 10% of the peak value.

Figure 4.7 shows a detail of the FEM solution. In particular, this picture shows the temperature variation in a disk sector where the concentrated heat flux applies on the external surface.

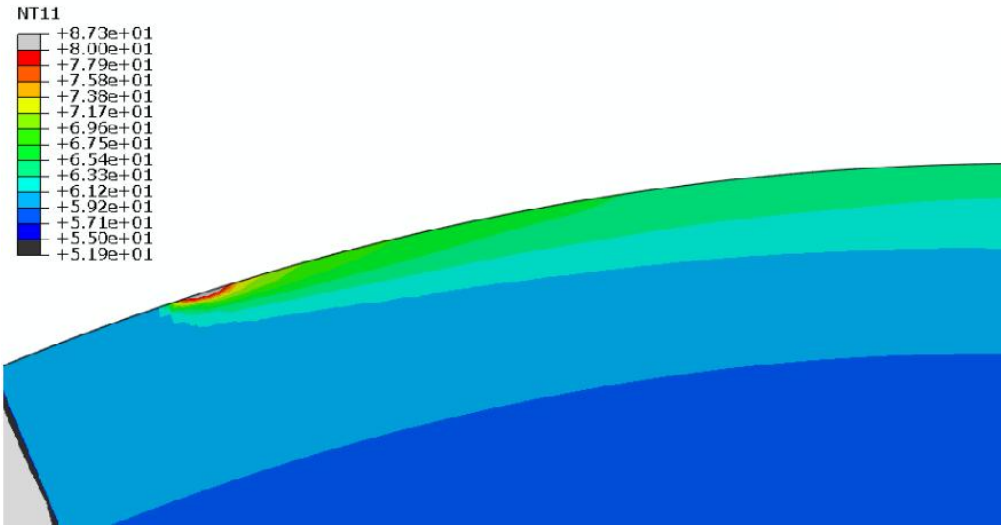

Figure 4.7: Detail of the temperature distribution [°C] in the FEM solution.

4.5.2. Comparison of modelling approaches

Before verifying the complete solution, a check on the transient solution (namely the one-dimensional solution, computed considering 20 eigenvalues: $m_{max} = 20$, many more than actually required, see Section 4.4.2) was carried out, just to verify the distributed heat flux accuracy, namely the heat contribution due to h_i and h_e. Comparison can be easily performed by simply looking at the external temperature calculated by the two models. Looking at Figure 4.8, it is evident that the two solutions match each other.

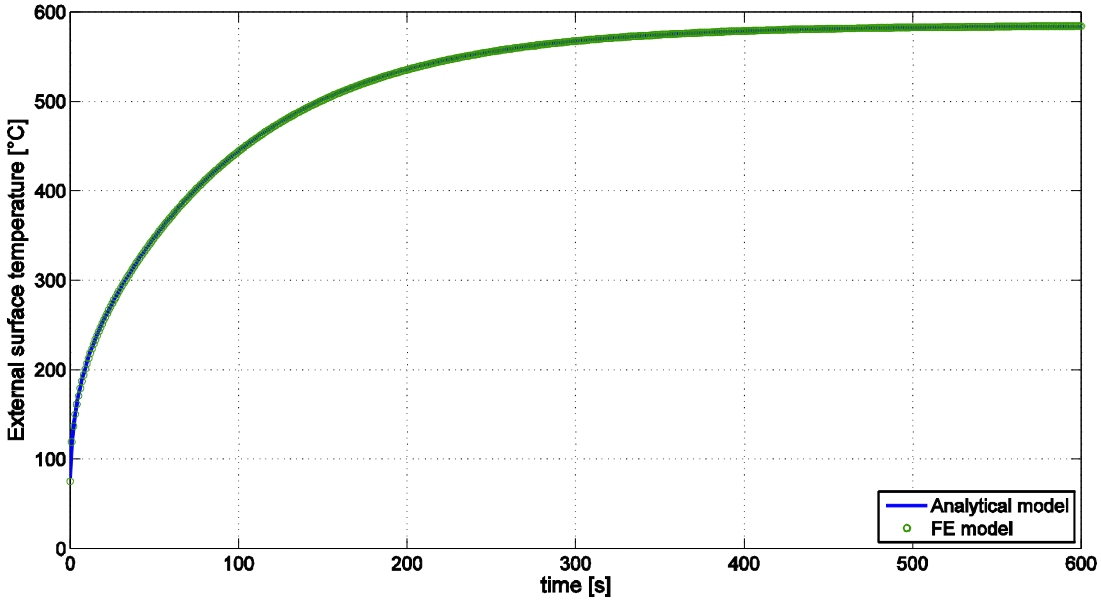

Figure 4.8: Comparison of FEM solution and analytical one for a one-dimensional problem.

Once the one-dimensional solution was assessed, the complete solution (namely that of the two-dimensional problem) reliability can be analyzed by means of a comparison between the external temperature calculated by the FEM model and by the analytical one (computed considering five eigenvalues: $m_{max} = 5$, and 250 frequencies: $n_{max} = 250$). Also in this case, the two solutions match very well, as Figure 4.9 shows. However, some little differences can be detected (Figure 4.9). Looking at the earliest time instants (Figure 4.10), a small difference in the analytical solution with respect to the FEM solution is visible. The analytical model overestimation is due to the truncation error introduced by the separation of variables method.

Moreover, looking at the flash temperature, it is possible to see that the FEM model computes a lower temperature than the analytical one. In this case, a very little underestimation is recorded by the FEM solution due to the imposed mesh size and time increment. In any case, the obtained analytical solution is capable to represent correctly the heat transfer phenomenon induced by a concentrated heat flux.

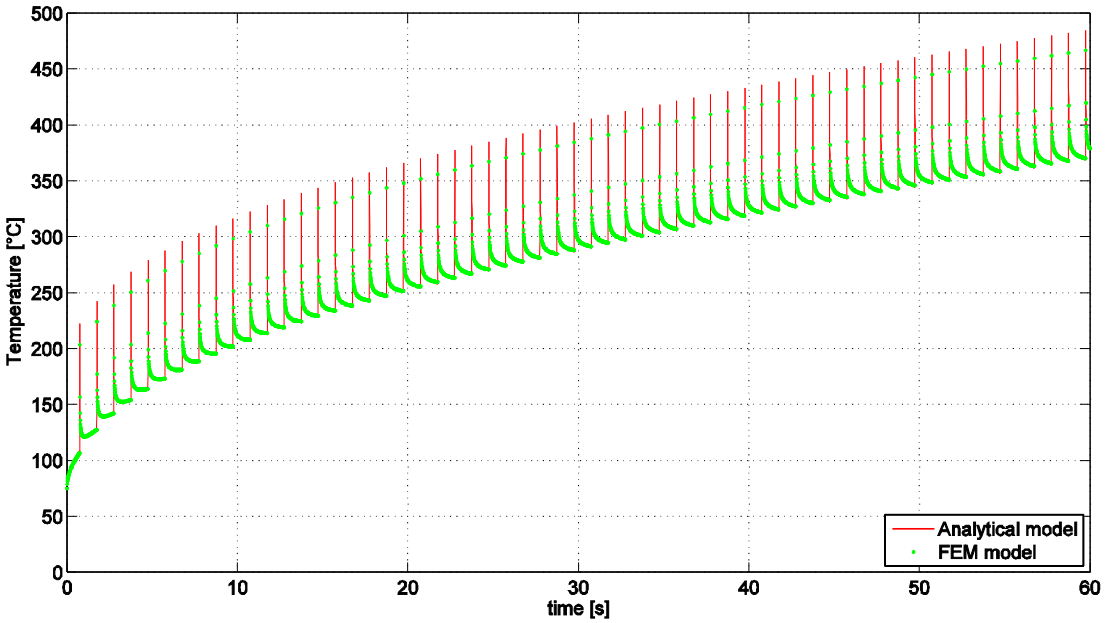

Figure 4.9: Comparison of FEM solution and approximate analytical one for the 2D problem.

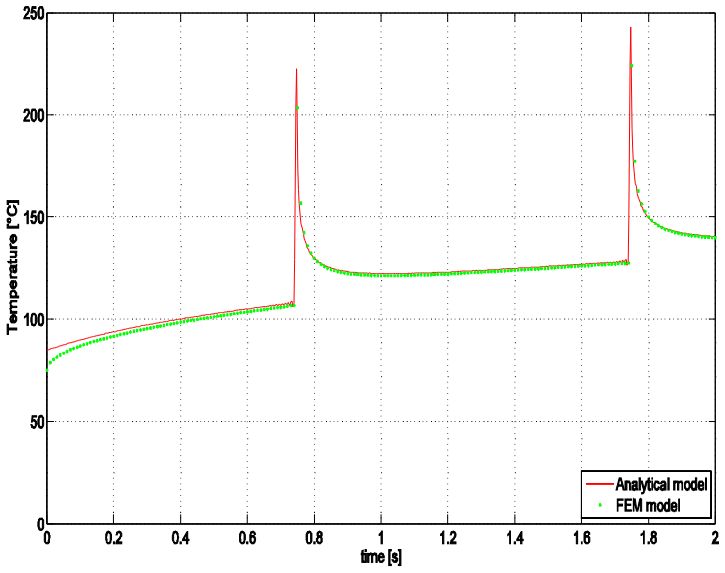

Figure 4.10: Detail of the comparison of FEM solution and approximate analytical one for the 2D problem.

Lastly, a comparison between the computational time required by the two solutions is targeted. From Table 4-3 it is evident that the analytical solution turns-out much faster. However, it must be pointed out that the time stated in the table is referred as follows. In the case of the FEM solution it represents the time needed to compute the solution for the whole model; instead, for the analytical solution, the time reported is referred only to the selected computation of the surface temperature. The possibility to select the point in which the solution is computed, for the purposes of this work, is another crucial aspect in favoring the analytical solution, especially in view of the subsequent inverse analysis under target.

Time required for 1 s of test simulation	
FEM model	***Analytical model***
17500 *s*	0.050 *s*

Table 4-3: Comparison between required computational times.

4.6. Specific application to the tribometer thermal problem

The real tribometer thermal problem shows a few small, but substantial, differences with respect to the theoretical problem, for which an analytical solution was previously achieved. Indeed, an analytical solution was achieved for a theoretical problem in which internal and external surfaces are subjected to a convective heat transfer and a constant concentrated heat flux on the external surface of on infinite rotating cylinder. In reality, taking into account the experimental set-up described in Section 3.2.2, only the internal surface is subjected to an unknown heat transfer; instead, the external surface is subjected to several heat fluxes, whose contribution shall be evaluated in a different way, as explained below.

In particular, the external surface was considered subjected to heat transfer by (Figure 4.11):

- Convection with air (q_a)
- Radiation with environment (q_{rR});
- Radiation with the hot disc (q_{rHD});
- Thermal contact conductance with the hot disc (q_c).

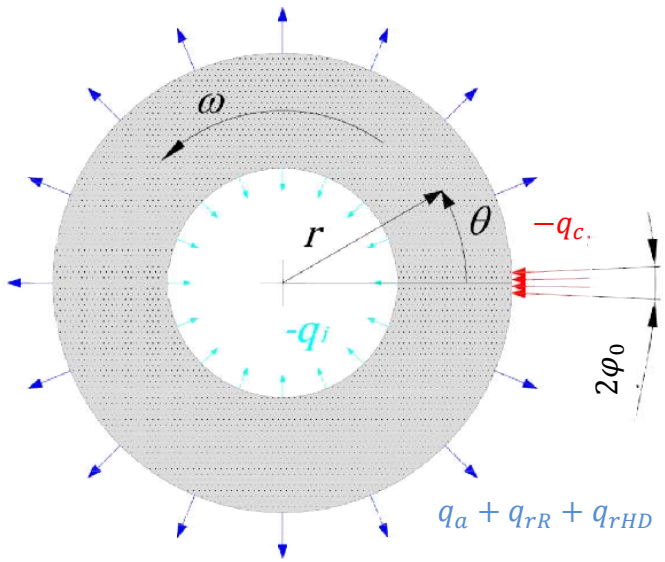

Figure 4.11: Rotating hollow cylinder under external heat conduction source and surrounding external and internal convection.

So, boundary conditions are now mathematically expressed by:

$$\textbf{BC1:} \quad -k\left.\frac{\partial u}{\partial r}\right|_{r=\rho_e} = \begin{cases} q_c, & -\varphi_0 \le \theta \le \varphi_0 \\ q_a + q_{rR} + q_{rHD}, & \varphi_0 \le \theta \le 2\pi - \varphi_0 \end{cases}$$

$$\textbf{BC2:} \quad -k\left.\frac{\partial u}{\partial r}\right|_{r=\rho_i} = -h\left(u|_{r=\rho_i} - u_{\infty,i}\right)$$

whereas the initial condition is

$$\textbf{IC:} \quad u(t=0) = f(r)$$

4.6.1. External convective cooling estimation

Heat transfer through a fluid occurs by convection in the presence of bulk fluid motion. In fact, a fluid flowing against a body at a different temperature forms a thin slowed-down layer called boundary layer. Heat is conducted into this layer, which sweeps away and mixes into the main flow. The process of carrying heat away by a moving fluid is called *convection* [50].

Although Newton may not have really written such an expression, to express the overall effect of convection Newton's law of cooling is commonly used:

$$Q_a = Aq_a = hA(u - u_\infty) \qquad (4.157)$$

here h is the film coefficient or heat transfer coefficient and u_∞ is the temperature of the oncoming fluid. Coefficient h is often considered in terms of an average value over the surface of heat transfer and not as a local value at a specific point of the surface.

For heat transfer at a surface within a fluid, the so-called *Nusselt number* (Nu) is the ratio of convective to conductive heat transfer across (normal to) the boundary, expressed by:

$$Nu = \frac{Lh}{k} \qquad (4.158)$$

where L is the characteristic length (equal to the diameter for a disc) and k is the thermal conductivity. Through the Nusselt number the heat transfer coefficient can be estimated.

In the literature, many empirical correlations were proposed to estimate this number under different geometrical and thermal conditions. As reported in [50], few correlations are available for the considered testing geometry and conditions. Among these, the following ones can be used:

Hilpert: $Nu_d = CRe_d^m Pr^{1/3}$

Zukauskas: $Nu_d = CRe_{d,max}^n Pr^{0.36}\left(\frac{Pr}{Pr_w}\right)^{1/4}$

Churchill and Bernstein: $Nu_d = 0.3 + \frac{0.62Re^{1/2}Pr^{1/3}}{[1+(0.4/Pr)^{2/3}]^{1/4}}\left[1+\left(\frac{Re}{282000}\right)^{5/8}\right]^{4/5}$

Whitaker: $Nu_d = \left(0.4Re^{1/2} + 0.06Re^{2/3}\right)Pr^{2/5}\left(\frac{\mu_\infty}{\mu_w}\right)^{1/4}$

where $Nu_d = \frac{2\rho_e h}{k}$ is the Nusselt number for cylinders, Re is the Reynolds number, Pr is the *Prandtl number*. Under experimental conditions all these correlations lead to an average value of $h \cong 10\,\frac{W}{°C\,m^2}$.

4.6.2. Radiative contribution

Heat transfer due to an electromagnetic radiation that propagated as a result of a temperature difference is called *thermal radiation*.

It was shown that an ideal thermal radiator, namely a "blackbody", will emit energy at a rate proportional to the fourth power of the absolute temperature u of the body and directly proportional to its surface area A. Thus, [50]:

$$q_r = \sigma A u^4 \tag{4.159}$$

where σ is a proportionality constant and is called the Stefan-Boltzmann constant with the value of $5.678 \cdot 10^{-8} \frac{W}{K^4 m^2}$. Eq. (4.159) is called the *Stefan-Boltzmann law* of thermal radiation, and applies only to blackbodies. Hence, the radiation heat exchange between two blackbodies' surfaces will be proportional to the difference in absolute temperature to the fourth power.

To take into account a non-ideal thermal radiator, namely a "gray-body", another factor, called emissivity ε, shall be introduced into Eq. (4.159). This parameter relates the radiation of a "gray" surface to that of an ideal black surface. Moreover, it must take into account the fact that not all the radiation leaving one surface will reach the other surface, since electromagnetic radiation travels in straight lines and some will be lost in the surroundings. So, a geometric view factor (F_G) shall be introduced as well into Eq. (4.159). Radiant heat exchanged between two gray-bodies is then represented as:

$$q_r = F_G \varepsilon \sigma A (u^4 - {u_r}^4) \tag{4.160}$$

In this case, the view factor F_G accounts for the fraction of radiation energy leaving the body at temperature u_r and reaching the considered surface.

Regarding the radiation with the hot body, this factor is computed according to the solution for an infinite parallel cylinder of different radius, as presented in [56]:

$$\begin{aligned} F_G = \frac{1}{2\pi}\Big\{ & \pi + [C^2 - (R+1)^2]^{1/2} - [C^2 - (R-1)^2]^{\frac{1}{2}} \\ & + (R-1)\cos^{-1}\left(\frac{R}{C} - \frac{1}{C}\right) - (R+1)\cos^{-1}\left(\frac{R}{C} + \frac{1}{C}\right)\Big\} \end{aligned} \tag{4.161}$$

where:

$$R = \frac{\rho_H}{\rho_e} \quad (4.162)$$

$$S = \frac{s}{\rho_e} \quad (4.163)$$

$$C = 1 + R + S \quad (4.164)$$

and ρ_H is the external radius of the hot disk and s is the distance between the two discs. Hence, for the considered problem geometry, in this work the view factor was taken equal to 0.26. The emissivity ε was set to a constant value of 0.75, after comparison with thermocouple measurements. Moreover, since the Stefan-Boltzmann law is clearly non-linear, the radiation law was linearized by introducing an equivalent convective coefficient h_r and an equivalent radiation temperature $u_r{}^*$, as suggested in [60], so that:

$$q_{rHD} = F_G A h_r{}^* (u - u_r{}^*) \quad (4.165)$$

In the considered cases, being the temperature range $[u_{min}, u_{max}]$ of the cold disc known while the hot disc temperature is constant during the contact step (see Section 3.3.2), it is possible to achieve a good estimation of the heat transfer by radiation. So, the equivalent coefficient and radiation temperature was defined by minimizing the discrepancy between the heat flux computed by means of the Stefan-Boltzmann law and the heat flux computed by a linearized radiation law, as shown in Figure 4.12. Mathematically, the problem can be written as:

$$\begin{aligned} [h_r{}^*, u_r{}^*] &= min[q_{HD} - q_{rHD}^*]_{u_{min}}^{u_{max}} \\ &= min[\varepsilon\sigma(u^4 - {u_{HD}}^4) - h_r{}^*(u - u_r{}^*)]_{u_{min}}^{u_{max}} \end{aligned} \quad (4.166)$$

where u_{HD} is the hot disk temperature.

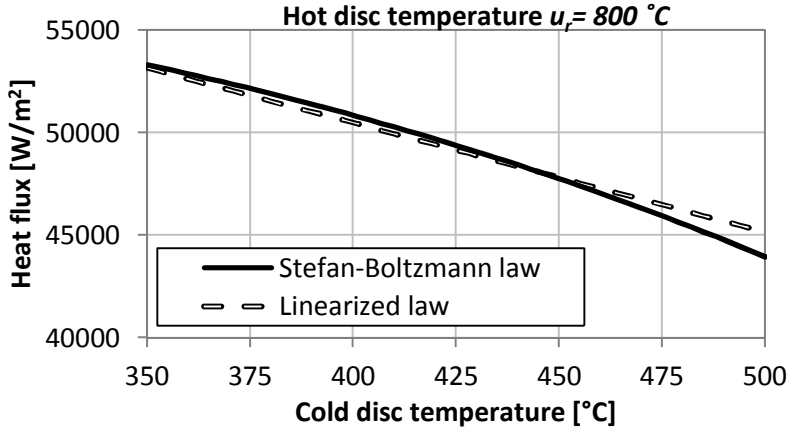

Figure 4.12: Stefan-Boltzmann law vs. linearized radiation law in the cold disc temperature range.

Radiation with the environment (q_{rR}) was treated in the same way. In this case, F_G can be considered equal to 1 since the whole external surface transfers heat by radiation with the environment.

4.6.3. Heat transfer by contact

As stated in Section 2.2.2., the use of a global Heat Transfer Coefficient (*htc*), that includes all thermal effects (namely thermal contact and gap conductance), appears to be a common practice in the modelling of industrial processes of hot metal forming. Since the aim of the present doctoral dissertation is to investigate heat exchange phenomena under hot rolling conditions, such kind of approach looks reasonable.

An exact mathematical approach for the contact heat transfer phenomenon would lead to solve the heat conduction problem under the following boundary condition:

BC1: $$\left.\frac{\partial u}{\partial r}\right|_{r=\rho_e} = \begin{cases} htc\ (u - u_{HD}), & -\varphi_0 \le \theta \le \varphi_0 \\ \dots, & \varphi_0 \le \theta \le 2\pi - \varphi_0 \end{cases}$$

The solution of this kind of boundary value problem involves the resolution of an integral equation of the Fredholm type, of the second kind [37]. Even though a solution in close form can be achieved, this is not convenient from the point of view of required computational time. Indeed, it is more suitable to solve the heat conduction problem by applying the following boundary condition:

BC1: $$\left.\frac{\partial u}{\partial r}\right|_{r=\rho_e} = \begin{cases} q_c & -\varphi_0 \le \theta \le \varphi_0 \\ \dots & \varphi_0 \le \theta \le 2\pi - \varphi_0 \end{cases}$$

where q_c is the heat flux at the contact arc, computed as follows:

$$q_c = htc\ (\bar{u} - u_{HD}) \qquad (4.167)$$

where $\bar{u}$ and htc are considered respectively as the mean surface temperature along the contact arc and the constant heat transfer coefficient. Basically, for the calculation of q_c, the punctual temperature u will not be taken into account, but an estimation of its mean value along the contact arc $\bar{u}$ will be considered. This approach allows to apply the previously found analytical solution directly to the present tribometer thermal problem.

In Eq. (4.169), $\bar{u}$ is approximated by superimposing a two-dimensional quasi steady-state solution for the angular temperature variation due to the concentrated heat flux and a one-dimensional solution, which evaluates the instantaneous evolution of the average surface temperature, as defined in Eq. (4.155). However, the surface temperature in the contact area is strongly influenced by the contact heat flux, which in turns depends on the surface temperature through Eq. (4.167). Anyway, the surface average temperature does not show a significant difference between a sample rotation and the following one, so q_c can be estimated with good approximation by considering as $\bar{u}$ the value that one computes at the previous rotation. Then, starting from the known initial condition, the heat flux by contact must be continuously upgraded, rotation after rotation.

4.6.4. Contact angle

Contact area plays a determinant role for an exact *htc* characterization. The contact arc segment of opening $2\varphi_0$ could be estimated through the Hertz theory, without taking into account any plastic material behavior. However, this leads to underestimating its value, especially for large loads, when plasticity may significantly affect the contact area. In order to identify the heat transfer coefficient without getting into coarse errors, a more accurate contact area estimation is needed. For this reason, a thermo-mechanical FEM model was implemented to assess the contact area, by considering the plastic behavior of both sample materials (see Section 6.2).

Nevertheless, since φ_0 is usually extremely small (less than 1°), the estimation of the *htc*, and its relative heat flux q_c by means of temperature measurements far from the contact zone, where the effect of the flash temperature is negligible, is almost entirely unaffected by any error in the determination of φ_0. The quasi steady-state solution for the temperature distribution along the disc circumference confirmed the validity of this basic assumption (Figure 4.13).

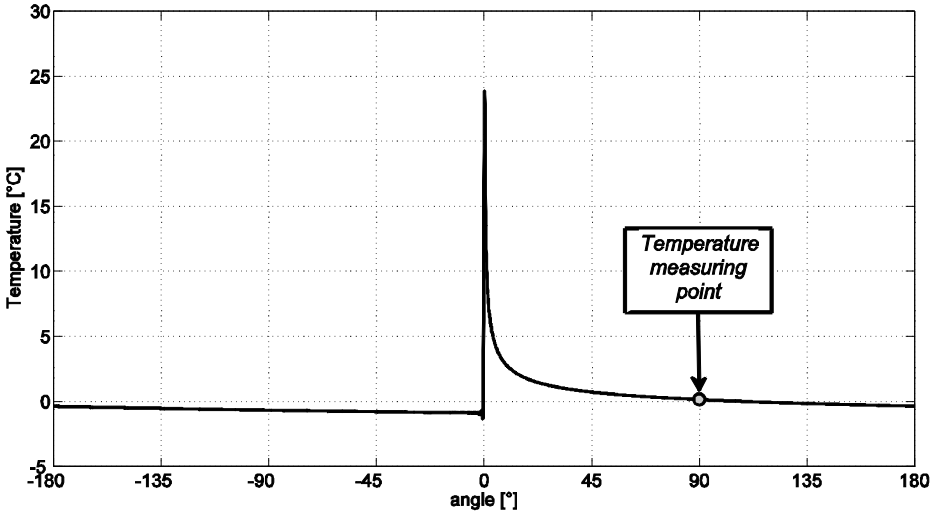

Figure 4.13: Example of calculated surface temperature along the cold disc circumference.

4.7. Flash temperature calculation

In order to reduce the required computational time to achieve the solution through the analytical model, another consideration shall be made regarding the computation of the flash temperature [15]. Taking advantage of the previously developed FEM model, it is easy to note how the flash temperature is actually insensitive to the heat transfer at the internal surface, as shown in Figure 4.14. Simply, by changing the order of magnitude of the internal heat transfer coefficient h_i namely by changing the order of magnitude of the resulting heat flux $q_i = h_i(u - u_i)$, it is easy to see that no changes appear for the computed flash temperature. This is due to the fact that the flash temperature phenomenon is very localized at the area and at the time in which thermal contact takes place (hence its name).

Thus, the model does not need to take into account the internal heat transfer for the calculation of the flash temperature and the internal heat transfer coefficient could be considered equal to 0. However, this does not allow to reach conspicuous savings in computational time. A better strategy is to consider a solid cylinder, instead of a hollow one, just for the flash temperature calculation. That means that the approximate solution presented in Eq. (4.155) can be further simplified by substituting the flash temperature solution for a hollow cylinder, namely the first summation term, with the solution achieved for a solid cylinder. So, the solution becomes:

$$u(r,\theta,t) = \beta \ln r + \gamma + \frac{1}{\pi}\sum_{n=1}^{\infty} Re\left[\left(D_n J_n(\epsilon_n r)\right) e^{jn\theta}\right] + \frac{1}{2\pi}\sum_{m=1}^{\infty} A_{m0} R_{m0}(\lambda_m r) e^{-\alpha {\lambda_m}^2 t} \quad (4.168)$$

In this flash temperature solution only a constant appears and it can be easily computed through Eq. (4.20), instead of the two complex constants of the hollow cylinder solution computable through Eqs. (4.86) and (4.87). This approximation allows to save more than 90% of the computational time required by the flash temperature solution, without appreciable loss of accuracy, as shown in Figure 4.15.

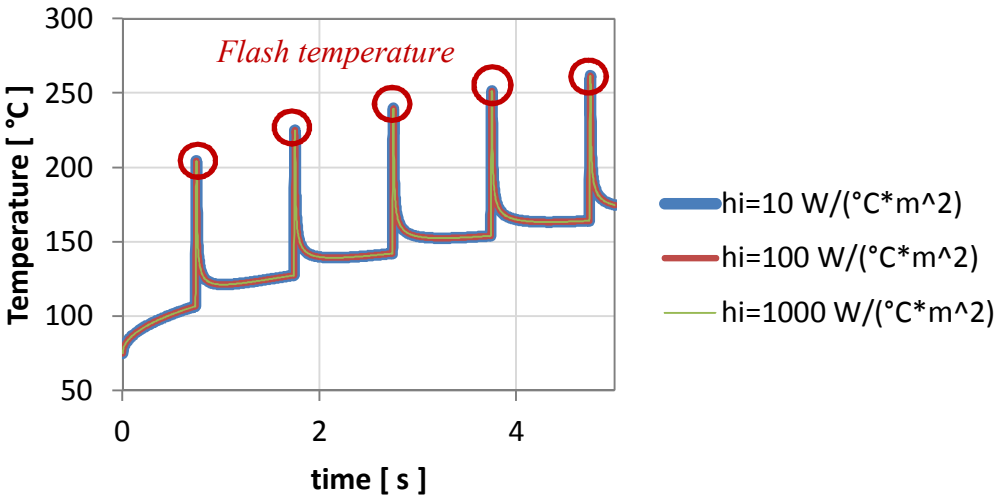

Figure 4.14: Flash temperature variation at different orders of magnitude of internal heat transfer.

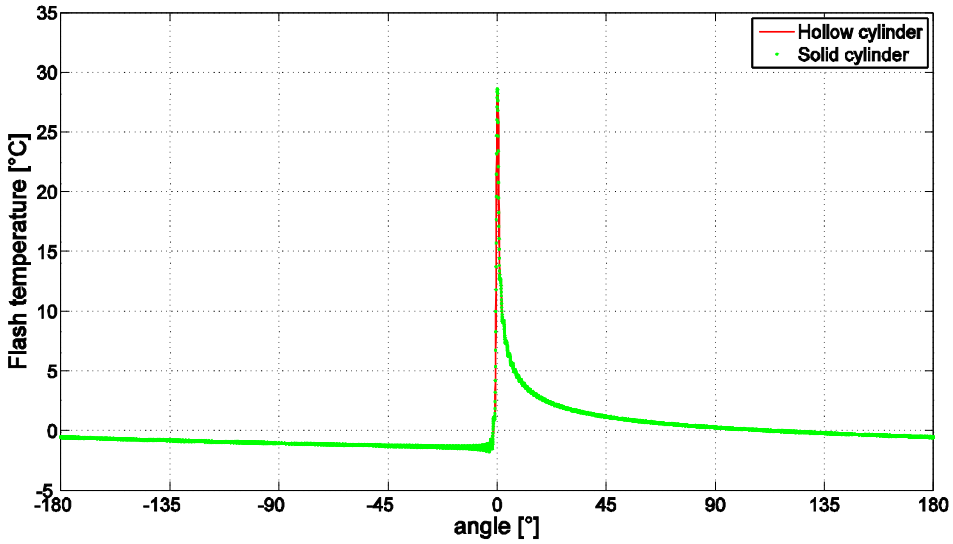

Figure 4.15: Comparison between hollow and solid flash temperature solution.

4.8. Model adaptation to the experimental conditions

Since a test starts when a constant external surface temperature, namely an initial steady-state condition, is achieved on the cold disc (see Section 3.2.2), the test mathematical description shall take this aspect into account. Hence, an initial temperature field shall be evaluated first and, then, applied to the test analytical model to assess the coefficients A_{m0} of the one-dimensional transient solution, namely the second summation of Eq. (4.168).

The initial temperature field $u_I(r)$ was evaluated, basically, as a solution of a steady-state problem. In particular, the initial condition shall be assessed solving a one-dimensional steady-state heat conduction problem applied to a hollow cylinder where the external surface is kept at a constant temperature (T_e) and the internal surface is subjected to an internal heat flux (q_i). Indeed, as explained in Section 3.2.2, tests start when sample has reached a steady-state condition, namely a thermal equilibrium. That implies that the target value of the external surface has been achieved and the other heat transfers, such as convective and radiative cooling and above all heat transfer with the spindle (q_i), have been stabilized to a constant value. As explained in Section 3.3.2.1, heat flux with the spindle can be considered constant for all test lenght; so, heat flux during tests is basically the same which affects the initial condition. However, this condition is unknown and can be evaluated only by means of an inverse analysis procedure of which it constitutes an unknown factor. Thus, through the inverse analysis it will be determined not only the heat transfer between sample and its spindle during the test, but also the initial temperature field.

The initial condition problem is mathematically expressed by:

$$r\frac{\partial u_I}{\partial r} + r^2\frac{\partial^2 u_I}{\partial r^2} = 0 \qquad (4.169)$$

under boundary conditions:

BC1: $u_I|_{r=\rho_e} = T_e$

BC2: $-k\left.\frac{\partial u_I}{\partial r}\right|_{r=\rho_i} = q_i$

The solution of ODE (4.169) takes the following form [9]:

$$u_I(r) = \beta_I \ln r + \gamma_I \qquad (4.170)$$

By imposing the first boundary condition, it follows that:

$$\beta_I = -\rho_i \frac{q_i}{k} \qquad (4.171)$$

and by applying the second boundary condition:

$$\gamma_I = T_e + \rho_i \frac{q_i}{k} \ln \rho_e \qquad (4.172)$$

Thus, the initial condition for the tribometer model is:

$$u(r, t = 0) = u_I(r) = T_e + \rho_i \frac{q_i}{k} (\ln \rho_e - \ln r) \qquad (4.173)$$

which shall be applied to the problem stated in Section 4.6.

Chapter 5. Inverse analysis procedure: theory and implementation

The implemented inverse analysis procedure may be referred to belonging to a particular class of inverse problems named *Inverse Heat Transfer Problems* (*IHTP*). IHTP are based on temperature or heat flux measurements for the estimation of unknown quantities appearing in the analysis of physical problems in thermal engineering. Therefore, while in the classical direct heat conduction problem the causes (boundary conditions, material thermal properties, etc.) are given and the effects (temperature field) is determined, the inverse problem involves the estimation of the causes above from the knowledge of the effects experienced in the observation of the heat transfer problem.

5.1. Inverse Heat Transfer Problem

In the last decades, the interest in the theory and application of Inverse Heat Transfer Problems has grown significantly. Nowadays, they are encountered in several branches of science and engineering related to thermal problems. Mechanical, nuclear, aerospace and chemical engineers, but also mathematicians and statisticians are often involved in the analysis of such problems. In situations in which well-established classical methods for the property estimation cannot provide a suitable degree of accuracy or may become inapplicable, IHTP techniques can be adopted.

The main goal of the direct thermal problem is the estimation of the temperature field $u(x,t)$ within a solid, when all characteristics (i.e., boundary conditions and attached parameters, initial condition, thermo-physical properties of the medium and energy generation

terms, if any) are specified. On the other hand, the objective of the inverse thermal problem is to estimate one or more of such unknown characteristics, from the knowledge of the measured temperature (the effect) at some specified location of the solid. Summarizing, in the direct problem the causes are given, the effect is determined; in the inverse problem, the effect is recorded, the causes are estimated.

Difficulties associated with the solution of IHTP were recognized. In fact, from a mathematical point of view, IHTPs belong to a class called Ill-posed problems ([2], [12], [13], [44], [90]), whereas standard heat transfer direct problems are Well-posed. The concept of a well-posed problem, originally introduced by Hadamard [44], requires that its solution should satisfy the following three conditions:

- The solution must exist;
- The solution must be unique;
- The solution must be stable under small changes of the input data.

The existence of a solution for an inverse heat transfer problem may be assured by a physical reasoning. For example, if there is a change in the values of the measured temperature in a transient problem, there exists a characteristic, as a boundary heat flux, to be estimated. On the other hand, the uniqueness of the solution of inverse problems can be mathematically proven only for some special cases [2], [13]. Also, above all, the inverse problem is very sensitive to random errors in the measured input data; thus, requiring special techniques for its solution, in order to satisfy the stability condition, namely the third condition above.

The temperature measurements provided by the sensors are incomplete in several aspects. First, these measurements are taken at discrete locations. Usually, there is only a finite number of sensors, sometimes only one. Hence, the spatial variation of the temperature is quite incompletely known. Moreover, the measurements obtained from any sensor are available only at discrete times, rather than continuously. So, since the accuracy of the solution obtained by an inverse analysis is affected by errors involved in the temperature measurements, it is instructive

to present the eight standard assumptions proposed by Beck [12],[13], regarding the statistical description of such errors. They are the following:

- Errors are additive, that is:

$$\hat{u}_i = u_i + \zeta_i \qquad (5.1)$$

where $\hat{u}_i$, is the measured temperature, u_i, is the actual temperature and ζ_i is the random error.

- Temperature errors ζ_i have a zero mean, namely:

$$E(\zeta_i) = 0 \qquad (5.2)$$

where $E(\zeta_i)$ is the expected value operator. Errors are then said to be unbiased.

- Errors have constant variance, that is:

$$\sigma_i^2 = E\{[\hat{u}_i - E(\hat{u}_i)]^2\} = \sigma^2 = const \qquad (5.3)$$

which means that the variance of $\hat{u}_i$ is independent of the measurements.

- Errors associated to different measurements are uncorrelated. Two measurement errors ζ_i and ζ_j, where $i \neq j$, are uncorrelated if the covariance of ζ_i and ζ_j is zero, namely:

$$cov(\zeta_i, \zeta_j) = E\{[\zeta_i - E(\zeta_j)][\zeta_i - E(\zeta_j)]\} = 0 \qquad (5.4)$$

This is the case if errors ζ_i and ζ_j have no effect or relationship to each other.

- Measurement errors have a normal (Gaussian) distribution. By taking into consideration the second, third and fourth assumptions above, the probability distribution function of ζ_i is given by:

$$f(\zeta_i) = \frac{1}{\sigma\sqrt{2\pi}} e^{-\frac{1}{2}\left(\frac{\zeta_i}{\sigma}\right)^2} \qquad (5.5)$$

- Statistical parameters describing ζ_i, such as σ, are known.

- The only variables that contain random errors are the measured temperatures. The measurement times, measurement positions, dimensions of the heated body, and all other quantities appearing in the formulation of the inverse problem are supposed to be accurately known.

- There is no prior information regarding the quantities to be estimated, which could be either parameters or functions. If such information exists, it can be utilized to obtain improved estimates.

All eight assumptions above rarely apply to actual experiments. For example, if the magnitudes of the measurement errors are quite unequal, the standard deviations σ_i are likely to be different. However, such assumptions are assumed to be valid throughout this work. This allow to verify the applicability of the inverse method, as well as of the stability of the inverse problem solution with respect to measurement errors. Moreover, as stated in [69], if the inverse heat transfer problem involves the estimation of only few unknown parameters, the use of ordinary least squares is allowed, since the solution is stable. Instead, if the inverse problem involves the estimation of a large number of parameters, excursions and oscillations of the solution may occur. The attempts to obtain the maximum amount of information from the experimental data imply small time steps of the experimental data acquisition, in order to maximize the included information. However, instabilities in the solution are frequently introduced by the use of small time steps [13] (notice that the condition of small time steps has the opposite effect in inverse problems than that that it has in the numerical solution of the direct problems). Hence, stability problems often can be corrected by choosing suitable time steps.

Generally, inverse problems are solved by minimizing an objective function with, in some cases, a stabilization technique used in the estimation procedure. If all eight statistical assumptions stated above hold, or can be assumed to be valid, the objective function ω, that provides the minimum variance estimates is the ordinary least squares sum [12] (i.e., the sum of the squared residuals) defined as:

$$\omega = (\hat{\boldsymbol{u}} - \boldsymbol{u})^T(\hat{\boldsymbol{u}} - \boldsymbol{u}) \qquad (5.6)$$

where $\hat{\boldsymbol{u}}$ and $\boldsymbol{u}$ are the vectors containing the measured and estimated temperatures respectively, and superscript T indicates transpose. The estimated temperatures are obtained from the solution of the direct problem with estimates for the unknown quantities. In particular, when the

transient readings $\hat{u}_i$ taken at times t_i, $i = 1, \dots, I$ of a single sensor are used in the inverse analysis, the transpose vector of the residuals, $(\hat{\boldsymbol{u}} - \boldsymbol{u})^T$, is given by:

$$(\hat{\boldsymbol{u}} - \boldsymbol{u})^T = (\hat{u}_1 - u_1, \hat{u}_2 - u_2, \dots, \hat{u}_I - u_I) \quad (5.7)$$

and the least squares norm, Eq. (5.7), can be written as:

$$\omega = (\hat{\boldsymbol{u}} - \boldsymbol{u})^T (\hat{\boldsymbol{u}} - \boldsymbol{u}) = \sum_{i=1}^{I} (\hat{u}_i - u_i)^2 \quad (5.8)$$

Referring to the present work, the use of the ordinary least squares norm given in Eq. (5.8) can be considered to be stable for different reasons. Among those, the considered IHTP involves the estimation of only two unknown parameters and this estimation was based on temperature measurements coming from long-run tests (1500 *s*), in order to maximize the available information and to minimize the impact of measurement errors. For the signal acquisition, a suitable time step (1 *s*) was chosen to avoid instabilities in the solution both of the inverse and of the direct problem. Moreover, signals were filtered using a moving average filter so as to reduce the influence given by signal scattering and to provide a smoother curve to the inverse analysis algorithm. This simplifies the comparison between the experimental curve with the theoretical one and restricts the local minima generation due to the signal noise.

5.2. Minimization algorithm

In the present thesis, the objective of the inverse analysis is the characterization of the boundary conditions applied to the analytical solution of the heat conduction problem in an infinite hollow cylinder. The optimum solution has been achieved through a minimization process, based on a least squares evaluation, of the mismatch between measured and computed temperatures. Different approaches are available in the literature; although the most commonly used is the Levenberg-Marquard method [69], the Trust-Region algorithm [87] has been chosen in order to achieve the solution in a quite limited number of iterations. This is due to the fact that this method employs linear algebra operations that do not require to store and/or to operate on full matrices. Moreover, Trust Region Methods are able to follow the negative curvature of the

objective function, whereas Levenberg-Marquardt algorithms seem unable to do so [92]. Thus, the latter approach could be much slower than the chosen one. In this paragraph, only a brief description of the applied optimization algorithm will be provided, referring to [10].

5.2.1. Quadratic models and Newton step

An effective method for the function minimization is based on the properties of a quadratic function $Q(\boldsymbol{x})$, such as:

$$Q(\boldsymbol{x}) = \frac{1}{2}\boldsymbol{x}^{\boldsymbol{T}}\boldsymbol{a}\boldsymbol{x} + \boldsymbol{b}^{\boldsymbol{T}}\boldsymbol{x} + c \qquad (5.9)$$

where $\boldsymbol{a}$ is a constant $n \times n$ matrix, $\boldsymbol{b}$ a constant n-vector and c a constant scalar. The gradient and the Hessian of $Q(x)$ are:

$$\nabla Q(\boldsymbol{x}) = \boldsymbol{a}\boldsymbol{x} + \boldsymbol{b} \qquad (5.10)$$

$$\nabla^2 Q(\boldsymbol{x}) = \boldsymbol{a} \qquad (5.11)$$

If $\boldsymbol{a}$ is non-singular, then the function in Eq. (5.9) displays a unique stationary point, which is found by solving the linear equations:

$$\boldsymbol{a}\boldsymbol{x} = -\boldsymbol{b} \qquad (5.12)$$

The solution will lead to a minimum if the Hessian matrix $\boldsymbol{a}$ is positive definite. On the other hand, it will lead to a maximum if $\boldsymbol{a}$ is negative definite or to a saddle point if $\boldsymbol{a}$ is indefinite.

These ideas can be applied also to a non-quadratic function $F(\boldsymbol{x})$. Supposing $\boldsymbol{x}_k$ to be an estimate of the minimum of $F(\boldsymbol{x})$ and knowing $\boldsymbol{g}_k = \nabla F(\boldsymbol{x}_k)$, $\boldsymbol{h}_k = \nabla^2 F(\boldsymbol{x}_k)$, F and ∇F can be approximated by truncated Taylor series:

$$F(\boldsymbol{x}_k + \boldsymbol{p}) \simeq Q(\boldsymbol{p}) = \frac{1}{2}\boldsymbol{p}^{\boldsymbol{T}}\boldsymbol{h}_k\boldsymbol{p} + \boldsymbol{p}^{\boldsymbol{T}}\boldsymbol{g}_k + F(\boldsymbol{x}_k) \qquad (5.13)$$

and

$$\nabla F(\boldsymbol{x}_k + \boldsymbol{p}) \simeq \nabla Q(\boldsymbol{p}) = \boldsymbol{h}_k\boldsymbol{p} + \boldsymbol{g}_k \qquad (5.14)$$

Therefore, if $\boldsymbol{h}_k$ is positive-definite, a first-order estimate of the search direction, $\boldsymbol{p}$ from $\boldsymbol{x}_k$ to the minimum of F is:

$$\boldsymbol{p} = -\boldsymbol{h}_k{}^{-1}\boldsymbol{g}_k \qquad (5.15)$$

This leads to the following solving algorithm:

- choose $\boldsymbol{x}_0$ as an initial estimate of the minimum of $F(\boldsymbol{x})$;
- repeat iteratively (for $k = 0,1,2,\ldots$) until $\|\nabla F(\boldsymbol{x}_{k+1})\|$ is sufficiently small as follows:
  - compute $\boldsymbol{g}_k = \nabla F(\boldsymbol{x}_k)$ and $\boldsymbol{h}_k = \nabla^2 F(\boldsymbol{x}_k)$;
  - if $\boldsymbol{h}_k$ is positive definite, then obtain $\boldsymbol{p_k}$ by solving (5.15), otherwise set $\boldsymbol{p_k} = -\boldsymbol{g}_k$;
  - find the step s so that $F(\boldsymbol{x}_k + s\,\boldsymbol{p_k}) - F(\boldsymbol{x}_k) \leq \eta s\,\boldsymbol{p_k}^T\boldsymbol{g_k}$ and $|F(\boldsymbol{x}_k + s\,\boldsymbol{p_k}) - F(\boldsymbol{x}_k) - s\,\boldsymbol{p_k}^T\boldsymbol{g_k}| \geq \eta|s\,\boldsymbol{p_k}^T\boldsymbol{g_k}|$ with $0 < \eta < 0.5$ (second and third Wolfe conditions);
  - Set $\boldsymbol{x}_{k+1} = \boldsymbol{x}_k + s\boldsymbol{p_k}$ and restart.

The vector $\boldsymbol{p}_k$ given by (5.15) is called the *Newton correction* and is based on regarding Q as a local quadratic model of F. Under favorable conditions, namely when the Hessian ($\boldsymbol{h}_k$) of F is positive definite, the Newton algorithm can be very efficient. If $\boldsymbol{h}_k$ is not positive definite, then the quadratic model displays a maximum or a saddle point rather than a minimum and then the Newton correction may become unsuitable. In this case, an alternative search direction is needed; as that provided for instance by the steepest descent method.

5.2.2. Trust-region reflective methods

The basic idea is to approximate $F(\boldsymbol{x}_k)$ with a simpler function $Q(\boldsymbol{x}_k)$, which reasonably reflects the behavior of function $F(\boldsymbol{x}_k)$ in a neighborhood $\mathcal{R}$ around the point $\boldsymbol{x}_k$, which can be referred to as *trust region*. The trust region $\mathcal{R}$ is the set of all points such that:

$$\mathcal{R} = \{\boldsymbol{x} \in \mathbb{R}^n | \|\boldsymbol{x} - \boldsymbol{x}_k\|_k \leq \Delta_k\} \qquad (5.16)$$

where Δ_k is called *trust-region radius* and $\|\cdot\|_k$ is an iteration-dependent norm [25]. A model function $Q(\boldsymbol{x}_k)$ is "trusted" only in the region where it provides a reasonable approximation. If an adequate model of the objective function is found within the trust region, then the region is expanded; conversely, if the approximation is poor, then the region is contracted. The fit is

evaluated by comparing the ratio of expected improvement from the model approximation with the actual improvement observed in the objective function.

Trust region methods are in some sense dual to line search methods: trust region methods first choose a step size (the size of the trust region) and then a step direction while line search methods first choose a step direction and then a step size.

Referring to Section 5.2.1, if $\boldsymbol{h}_k$ is not positive definite, a downhill search direction, can be achieved by solving:

$$(\lambda \boldsymbol{I} + \boldsymbol{h}_k)\boldsymbol{p}_k = \boldsymbol{g}_k \qquad (5.17)$$

for a "suitably large" value of positive scalar λ. This is because the eigenvalues of $\lambda \boldsymbol{I} + \boldsymbol{h}_k$ exceed those of $\boldsymbol{h}_k$ by λ and hence, when λ is big enough, $\lambda \boldsymbol{I} + \boldsymbol{h}_k$ may become positive definite.

Using a search direction given by Eq. (5.17) might seem as arbitrary as the matrix modification approaches outlined above. However, it turns out that Eq. (5.17) gives $\boldsymbol{p}_k$ as a solution of a subproblem in the form:

$$Minimize \quad Q(\boldsymbol{p}) = \frac{1}{2}\boldsymbol{p}^{\boldsymbol{T}}\boldsymbol{h}_k\boldsymbol{p} + \boldsymbol{p}^{\boldsymbol{T}}\boldsymbol{g}_k \quad for \ \|p\|_2 \leq \Delta_k \qquad (5.18)$$

In other words, $\boldsymbol{x}_k + \boldsymbol{p}_k$ minimizes a quadratic approximation of F subjected to an upper bound on the size of the move away from $\boldsymbol{x}_k$.

The problem in Eq. (5.18) has always a solution even when $\boldsymbol{h}_k$ is not positive definite. This is because it simply amounts to finding the smallest value of $Q(\boldsymbol{p})$ within a hyperspherical region around $\boldsymbol{x}_k$. Hence Eq. (5.18) provides a reasonable way of choosing a search direction when the Newton correction is not appropriate. Problem (5.18) is the basis for a class of minimization techniques known as trust-region methods, fully described in [25]. Most of the considered methods work by choosing a promising search direction first and then by determining a step size by a line search. Trust-region methods reverse this approach and decide on a suitable step size before calculating a direction to take.

Suppose, for instance, that there is a reason to trust that a local quadratic model of F will be reasonably accurate within a distance $\|\Delta_k\|$ from the current iterate $\boldsymbol{x}_k$. A new point $\boldsymbol{x}_{k+1} = \boldsymbol{x}_k + \boldsymbol{p}_k$ could then be obtained by solving Eq. (5.18), whether $\boldsymbol{h}_k$ is positive definite or not. The trust-region radius, Δ_k, can be adjusted from iteration to iteration. It is increased if the actual change $F(\boldsymbol{x}_{k+1}) - F(\boldsymbol{x}_k)$ agrees well with the predicted change in the quadratic model. Conversely, it is decreased if the actual and predicted changes are too inconsistent. Ultimately, the value of Δ_k becomes large enough for the subproblem in Eq. (5.18), to allow full Newton steps to be taken and hence to achieve quadratic convergence. One disadvantage of the trust-region approach is that Eq. (5.18) can be difficult and expensive to be solved accurately on each iteration. The relationship between the trust region radius Δ_k and the value of λ in Eq. (5.17) is highly nonlinear and this makes uneasy to obtain $\boldsymbol{p}_k$ to solve Eq. (5.18) via a single solution of Eq. (5.17).

Therefore, most implementations make use of an approximate solution of Eq. (5.17), which can be sought in the following way. Defining:

$$\mu = \lambda^{-1} \tag{5.19}$$

Eq. (5.17) is equivalent to:

$$(\boldsymbol{I} + \mu\boldsymbol{h})\boldsymbol{p} = -\mu\boldsymbol{g} \tag{5.20}$$

If λ is sufficiently large that the matrix $\mu\boldsymbol{h}$ is small as compared to $\boldsymbol{I}$ and this expansion can be used:

$$(\boldsymbol{I} + \mu\boldsymbol{h})^{-1} = \boldsymbol{I} - \mu^2\boldsymbol{h}^2 + \mu^3\boldsymbol{h}^3 + \boldsymbol{O}(\mu^4) \tag{5.21}$$

to obtain an approximate solution as:

$$\boldsymbol{p} = -\mu\boldsymbol{\xi}_o - \mu^2\boldsymbol{\xi}_1 + \mu^3\boldsymbol{\xi}_2 \tag{5.22}$$

where $\boldsymbol{\xi}_o = \boldsymbol{g}$ and $\boldsymbol{\xi}_k = \boldsymbol{h}^k$ for $k = 1,2, \ldots$

A suitable value for μ can be found by a trial-and-error process. For a sequence of values $\mu_1, \ldots, \mu_k$ with $0 < \mu_1 < \mu_2 < \cdots < \mu_k < \left\|\boldsymbol{h}^k\right\|^{-1}$, Eq. (5.22) can be used to obtain $\boldsymbol{p}_1, \ldots, \boldsymbol{p}_k$ as candidate directions (without any cost of matrix factorization). Then, the curvature of the objective function along each direction $\boldsymbol{p}_i$ can be evaluated as:

$$\kappa_i = \frac{\boldsymbol{p}_i{}^T \boldsymbol{h} \boldsymbol{p}_i}{\boldsymbol{p}_i{}^T \boldsymbol{p}_i} \quad (5.23)$$

If possible, a search direction $\boldsymbol{p}_i$ leading to the most negative value of κ_i should be taken into account. Otherwise, the one with the smallest positive value must be chosen. In either case, quite a large step is expected to be taken, which may cause the search to move rapidly away from the non-convex region, to one where $\boldsymbol{h}$ becomes positive definite.

The way chosen by the MATLAB solver for avoiding the cost of solving Eq. (5.18) is to reduce the trust-region subproblem to a 2-D subspace *S*. Once the subspace *S* has been computed, the amount of work necessary to solve Eq. (5.18) is low, even if full eigenvalue/eigenvector information is needed (since in the subspace, the problem is only two-dimensional). The dominant work has now shifted to the determination of the subspace. The two-dimensional subspace *S* is determined with the aid of a preconditioned conjugate gradient process. The solver defines *S* as the linear space spanned by $\boldsymbol{\psi}_1$ and $\boldsymbol{\psi}_2$, where $\boldsymbol{\psi}_1$ is in the direction of the gradient $\boldsymbol{g}_k$, and $\boldsymbol{\psi}_2$ is either an approximate Newton direction, i.e. a solution of:

$$-\boldsymbol{g}_k = \boldsymbol{h}_k \boldsymbol{\psi}_2 \quad (5.24)$$

or a direction of negative curvature, $\boldsymbol{v}$, such that:

$$\boldsymbol{v}^T \boldsymbol{h}_k \boldsymbol{v} < 0 \quad (5.25)$$

In other words, the negative gradient $-\boldsymbol{g}_k$ could be combined with the Newton direction $\boldsymbol{p}_k$ (even if this is uphill) [10]. This would mean seeking a new point $\boldsymbol{x}_{k+1} = \boldsymbol{x}_k - \boldsymbol{\psi}_1 \boldsymbol{g}_k + \boldsymbol{\psi}_2 \boldsymbol{p}_k$ that gives the least value of *F* in the plane $\boldsymbol{p}_k - \boldsymbol{g}_k$, subject to a restriction on stepsize. Better still, for the non-positive definite case, would be to determine a direction of negative curvature, $\boldsymbol{v}$, the minimum of *F* in a plane defined by $-\boldsymbol{g}_k$ and a negative curvature [106].

5.3. Algorithm implementation

The inverse analysis algorithm was developed starting from the procedure presented by Arizzi and Rizzi in [7]. The algorithm makes use of two sources of information: target experimental recorded results and numerical data that, depending on a number of modelling

parameters to be identified (here the following two parameters: internal heat flux and heat transfer coefficient), arise from analytical simulations of the test. The discrepancy among target experimental data and computed data is minimized, towards the identification of the heat fluxes allowing for most effective calibration. Such discrepancy minimization is measured in terms of an appropriate objective function, which quantifies, through an appropriate scalar measure, the difference between target and predicted data.

To allow confrontation among the various curves, the input/output information is compared on appropriate snapshots, representing a discrete number of temperature measurements assessed at specific test times. As explained in Section 5.1, to avoid instability of the solution, a suitable time step has been selected as 1 s. This and the test duration legitimate the use of the ordinary least square problem and, hence, the use of the trust region method for the solution of the inverse problem.

5.3.1. Objective function

The assumed objective function corresponds to a discrete non-negative, *non-dimensional* ordinary least-square discrepancy measure defined as follows:

$$\omega(\boldsymbol{q}) = \sum_{i=1}^{I} \left(\frac{\hat{u}_i - u_i(\boldsymbol{q})}{\hat{u}_{max}} \right)^2 \qquad (5.26)$$

where $\boldsymbol{q}$ is the vector of unknown optimization variables, namely the unknown heat fluxes, and the maximum measured temperature $\hat{u}_{max}$.

5.3.2. Outline of the computational algorithm

Once the objective function has been defined, the solution of the inverse problem, devoted to the best identification of the model parameters, is re-conducted to the determination of an absolute minimum of the objective function, within a selected range of optimization variables $\boldsymbol{q}$, by locating the corresponding optimum values of the material parameters.

A numerical algorithm is put in place within MATLAB, by taking as optimisation function the *lsqnonlin function* from the *Optimization Toolbox* [65]. A flow chart of the implemented algorithm is sketched in Figure 5.1. This is an adaptation to the present framework of an extensive implementation referring to the determination of material parameters in elasto-plastic indentation [7]. The *lsqnonlin function* in MATLAB requires as entries: the evaluation of the *objective function*; a start point $\boldsymbol{q}_0$ from which the search of the absolute minimum departs; lower and upper bounds for the optimisation variables. Then, it proceeds to an iterative search towards the absolute minimum, by varying the optimisation variables (here internal heat flux and heat transfer coefficient), evaluating through them the objective function and its *jacobian J*, at each iteration and checking convergence/stopping criteria, as reported below.

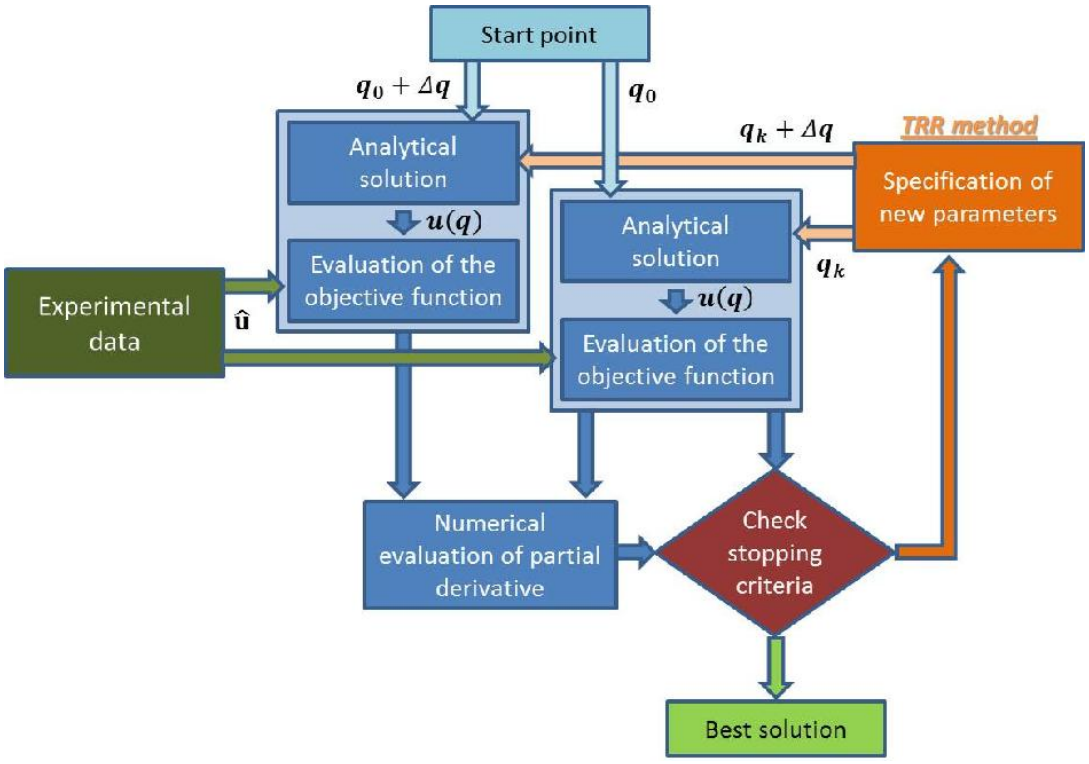

Figure 5.1: Inverse analysis algorithm.

The evaluation of the objective function is made by calculating *ω(x)* by comparing target experimental data $\hat{u}_i$, to simulated data from the analytical model function u_i, for each value of optimisation variables $\boldsymbol{q}$. The objective function can then be evaluated only after the activation of a function, which provides the solution of the direct problem, by producing the solution u_i,

for the unknown variables $\boldsymbol{q}$ of the inverse problem. The objective function assesses only $\omega(\boldsymbol{q})$; the jacobian *J* is calculated by finite difference approximations. When the *lsqnonlin* function is called, this automatically passes the *start point* $\boldsymbol{q}_0$ to the objective function, towards the evaluation of $\omega(\boldsymbol{q}_0)$; this, in turn, passes $\boldsymbol{q}_0$ to the *analytical solution function*, for the evaluation of $u_i(\boldsymbol{q}_0)$ and recalls target data $\hat{u}_i$. Afterwards, *lsqnonlin* calls the objective function two more times, by giving in input no longer the *start point*, but rather two points in its vicinity. The value of the objective function at these points is used to evaluate the jacobian $J\,\omega(\boldsymbol{q}_0)$. The same is repeated for each subsequent value of optimization parameters $\boldsymbol{q}$, in each iteration.

Then, the minimisation function checks convergence and stopping criteria, according to the following three main conditions:

- tolerance on objective function: $\omega(\boldsymbol{q}_k) < \Delta_\omega$, with $\Delta_\omega = 10^{-3}$;
- tolerance on gradient norm: $\|\nabla\omega(\boldsymbol{q}_k)\| < \Delta_g$, with $\Delta_g = 10^{0}$;
- tolerance on parameter norm: $\|\boldsymbol{q}_k - \boldsymbol{q}_{k-1}\| < \Delta_x$, with $\Delta_x = 10^{-4}$.

where $k = 0,1,\ldots$ is the iteration counter.

The criterion tests if the least square sum is sufficiently small, which is expected to be in the neighbourhood of the solution of the problem. Similarly, the second criterion checks if the norm of the gradient of $\omega(\boldsymbol{q}_k)$ is sufficiently small, since it is expected to vanish at the point where $\omega(\boldsymbol{q}_k)$ is minimum. The last criterion results from the fact that changes in the vector of parameters are very small when the method is converging. The use of a stopping criterion based on small changes of the least squares norm $\omega(\boldsymbol{q}_k)$ could be used, but with extreme caution. It may happen that the method stalls for a few iterations and then starts advancing faster to the minimum [69].

If none of the above control conditions is satisfied, *function lsqnonlin* proceeds to the definition of a new set of the unknown variables $\boldsymbol{q}$, through the *Trust Region-Reflective* method.

Iterations go on until when one convergence condition is satisfied. Then, the optimum solution of the inverse problem is considered to have been achieved.

Chapter 6. Quantitative assessment of the heat transfer coefficient

Mathematical tools developed in the previous two chapters are applied to the experimental results presented in Section 3.3.2, in order to characterize experimentally the heat transfer coefficient *htc*. The unknown coefficient is determined by means of the temperature increment on the cold disc, recorded during the contact step with a hot disc kept at a constant temperature, as explained in Section 3.2.2.

6.1. Inverse analysis aim

The inverse analysis procedure presented in previous Chapter 5 is based on an approximation of the heat conduction solution applied to an infinite hollow cylinder, as firstly discussed in Chapter 4. In turn, the analytical solution considered a considerable number of parameters which define both the material properties and the boundary conditions. Thermo-physical properties of the material were estimated through a commercial software [85] that allows to characterize the material properties as a function of temperature with good reliability. Regarding the boundary conditions, some of them can be defined through empirical correlations from the literature (see Section 4.6.1), others can be approximated from their theoretical phenomenological law (see Section 4.6.2), but the heat fluxes transfer by contact must be determined only through the previously-defined inverse analysis algorithm. Cold disc is subjected to two different heat transfers by contact: the first is on the external surface and it is caused by the contact with the hot disc, the second is on the internal surface, due to the contact by the sample's driveshaft. This last parameter is completely unknown and it is strictly

connected to the geometry of the contact between the sample and its shaft. For this reason, the internal flux q_i was taken as an inverse analysis variable, in the same way as for the *htc*.

6.2. Contact area estimation

Contact area plays a determinant role for an exact *htc* characterization. Indeed, to be able to accurately define the *htc* value, the thermal flow transferred by contact must be related to the temperature difference between the two bodies in contact and, above all, to the contact area. If the temperature difference can be estimated quite easily through experimental measures and numerical prediction, the contact area estimation looks more complex to be estimated, despite that the contact problem geometry is rather simple. Even though several experimental approaches are available, they are not applicable in the present work due to the presence of high temperature. Hence, a theoretical approach was chosen. However, the solution of the mechanical contact problem is still complex.

The presence of high temperatures and high normal loads do not allow to use the Hertz model [48], which considered only a linear elastic behaviour of the materials in contact. Indeed, in the considered cases, owing to high temperature, the first yield stress comes down quickly and, then, the plastic condition can be easily reached under the normal load applied during the test. For this reason, a FEM model able to consider all the thermo-mechanical phenomena was implemented.

6.2.1. Contact FEM model

Aim of the modelling was not that of simulating exactly all the contact phenomena that take place during the test, but that of reaching a good approximation of the real contact area extension. For this reason, some appropriate assumptions were made. Firstly, cylinders were considered infinitely long as in the Hertz solution; secondly, the rotation effects were not included in the model, since only the pure rotation condition was considered in experimental

activities; lastly, the thermal effects were considered in terms of average temperature over the external surfaces in contact (no flash temperature effect was taken into account). So, to evaluate the contact geometrical characteristics, a static bi-dimensional thermo-mechanical model was implemented.

The FEM model was developed with ABAQUS and it was composed by two elements that simplify the real problem geometry, whose characteristics are collected in Table 6-1. Indeed, the model was not constituted by two rings representing the cross-section of two infinite cylinders but only by two ring sections of these cylinders, as shown in Figure 6.1. The hot disc was discretized in about 5100 finite elements, mainly with 4 nodes, whereas the cold disc was mashed in 4800 finite elements, as displayed in Figure 6.1. Mesh size in the contact zone was chosen to achieve a refined enough contact arc estimation. In particular, it was found that mesh size of 5 μm looked suitable for that purpose, see Figure 6.2.

Problem geometry	
Hot disc	**Cold disc**
$\boldsymbol{\rho_e}$= 0.06 $\boldsymbol{m}$	ρ_e= 0.025 m
$\boldsymbol{\rho_i}$= 0.015 $\boldsymbol{m}$	ρ_i= 0.012 m

Table 6-1: Geometric characteristics of the problem.

All thermo-mechanical material proprieties were considered dependent on the material temperature and they were defined through a commercial software [85]. The contact phenomena simulation occurs in two different steps: the first is merely thermal; instead, the second is thermo-mechanical. Firstly, only thermal boundary conditions were applied to the two elements. Thermal boundary conditions consider a constant temperature (from experimental results) on the external surfaces and a constant flux (estimated) in the inner surfaces. When temperatures had reached a steady state condition, the two rings were put in contact and the normal load was increased up to the scheduled value for the test condition. When the normal load had arrived at its maximum value, the contact pressure and contact arc were recorded and put in the inverse analysis procedure. Different levels of temperatures and normal load were investigated, according to the experimental activities (see Table 3-1).

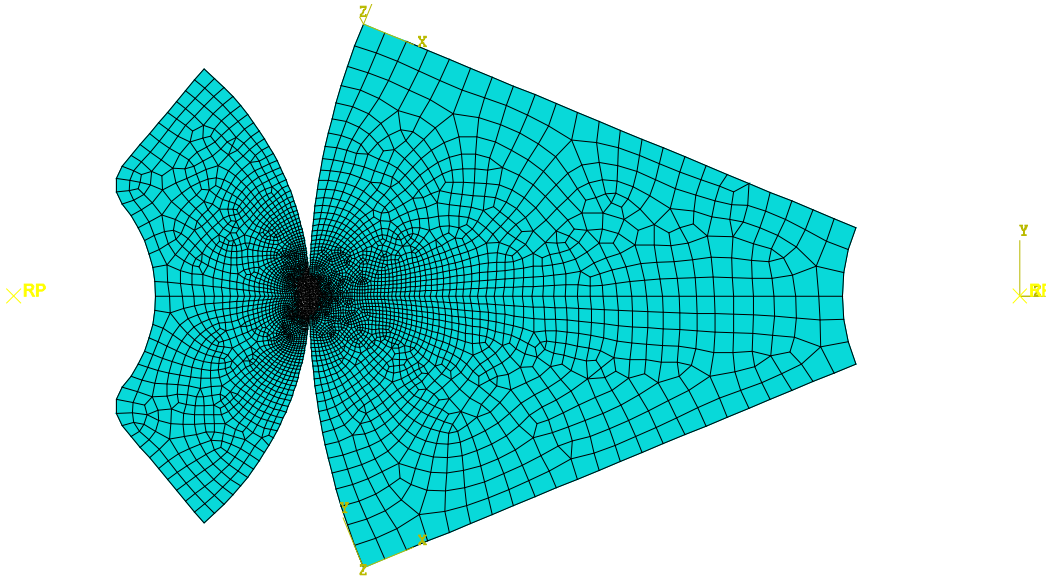

Figure 6.1: Contact problem discretization.

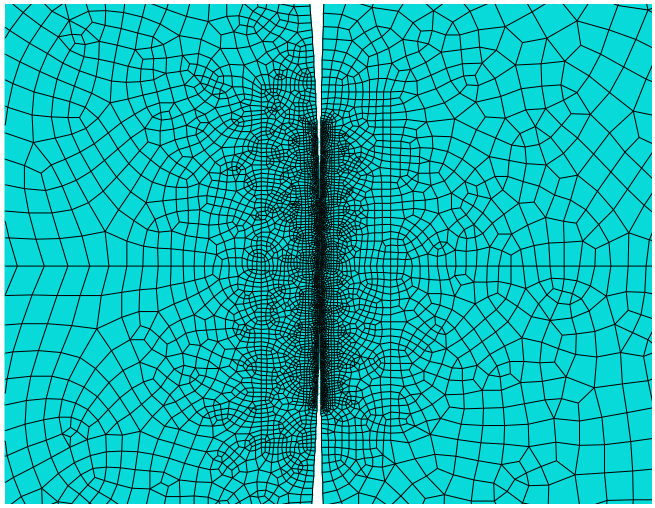

Figure 6.2: Detail of the discretization in the contact zone.

This model simplifies the real contact condition. However, it can be considered as a valid way to achieve a first but realistic estimation of the real contact area.

6.2.2. FEM results

FEM results clearly show how different is the mechanical response when the material reaches high temperatures. For the cases in which the hot disc temperature is 400 °C and 600 °C, Figure 6.3 shows an increase of the mean contact pressure, when the normal load increases, and the contact pressure value is similar in both cases. For the 800 °C cases, the contact pressure is markedly low and its relationship with the normal load is not so evident.

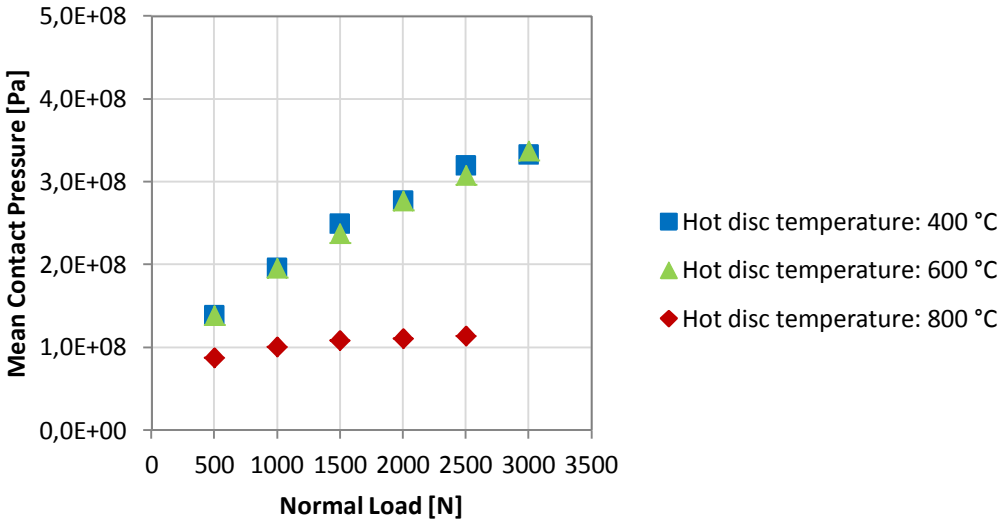

Figure 6.3: Mean contact pressure for different normal loads under different thermal conditions.

This is due to the achievement of a localized plastic condition, as shown in Figure 6.4. Interestingly, the plastic strain occurs on the hot disc where, due to the high temperature, the first yield strength is drastically lowered. So, even though stresses are lower in the hot disc, as shown in Figure 6.5, the lower yield stress is able to promote plastic deformation in the hot disc, determining such low values of contact pressure.

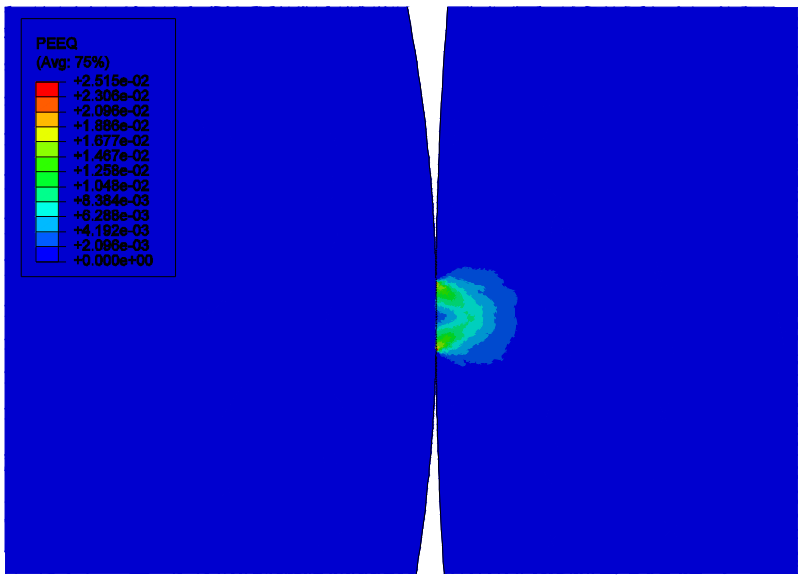

Figure 6.4: Effective plastic strain in the contact zone.

The maximum pressure trends shown in Figure 6.6 confirm the previous considerations. Indeed, the maximum contact pressure is still lower for the 800 °C cases. Additionally, the

maximum pressure trends show that, for the highest normal loads, even in the case of 600 °C plastic deformation was reached. Even though the mean contact pressure is about the same for all 400 °C and 600 °C cases, the lower maximum pressure detectable at the highest normal load denotes the attainment of an initial plastic deformation also in these cases.

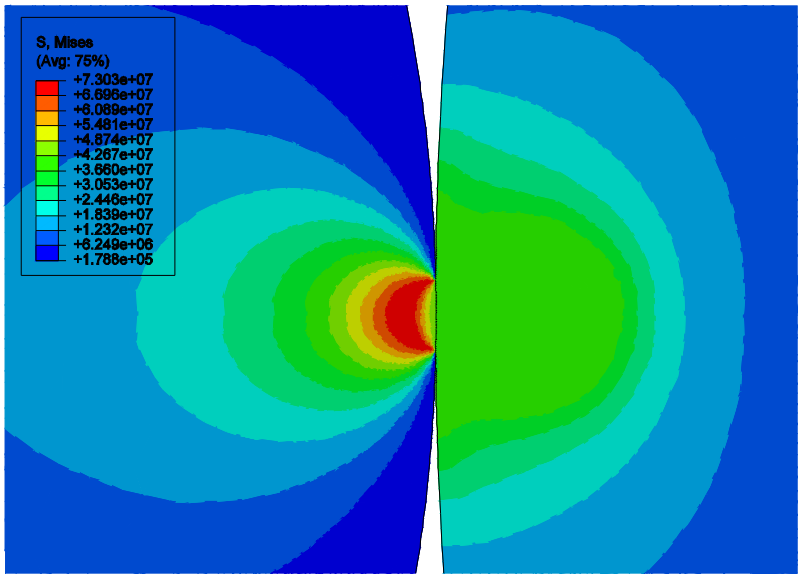

Figure 6.5: von Mises stress in in the contact zone (Pa).

In terms of contact angle, Figure 6.7 shows approximately the same value for both the 400 °C and 600 °C cases. Instead, when temperature rises up to 800 °C, the contact angle becomes such greater than for the previous cases, due to the occurring of localized plastic deformations.

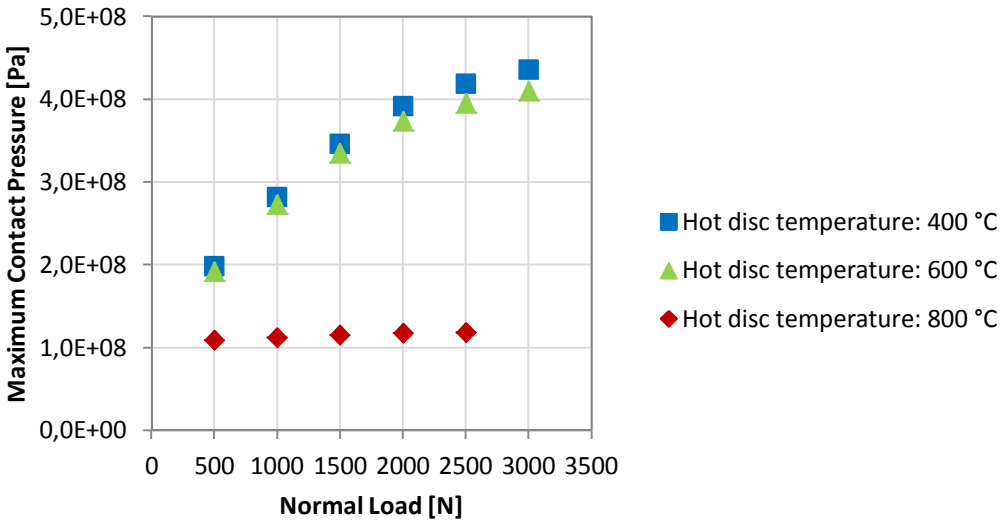

Figure 6.6: Maximum contact pressure for different normal loads under different thermal conditions.

Notice that outcomes for hot disc temperature 800 °C are always distinct from those at the other two temperatures of 400 °C and 600 °C due to a different material behavior. This is an interesting results of the present investigation and clearly states the role of high temperature in hot deformation processes.

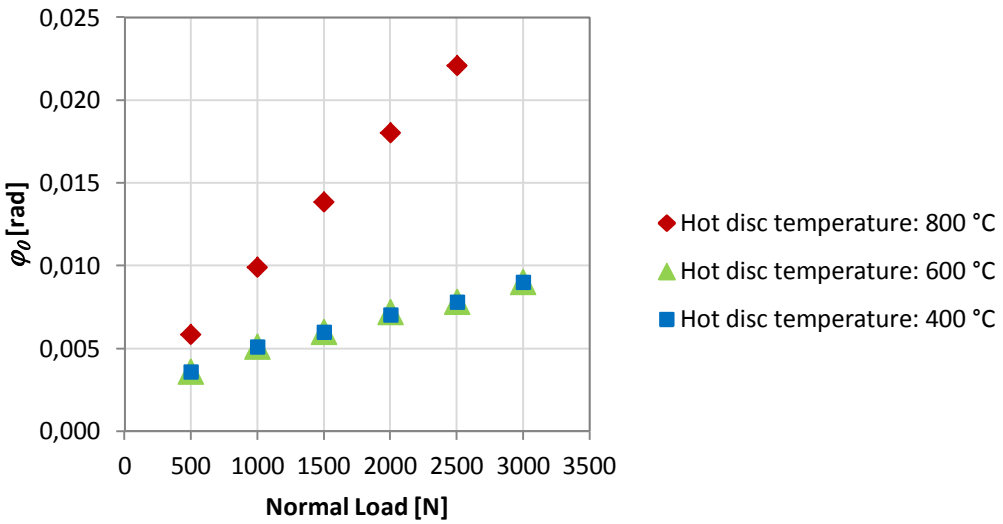

Figure 6.7: Semi-contact angle for different normal loads under different thermal conditions.

6.3. Inverse analysis results

All the experimental results presented in Section 3.3.2 were analyzed through the inverse analysis algorithm, in order to characterize the *htc* under different contact conditions.

Due to inability of the minimization algorithm to recognize the global minimum (see Section 5.2), four different inverse analyses were run for each experimental result, starting from four different start points. When all the analyses converge into the same minimum point, the found minimum can be considered as a global minimum for the inverse problem, i.e. a correct solution. Two different levels were chosen for each of the two unknown parameters as for the start point. The combination of these values supplies the four different start points positioned at the extremities of the parameter space taken into account. Initially, $0.2\ k\,W/(°C\ m^2)$ and $20\ k\,W/(°C\ m^2)$ for *htc*, whereas $0\,W$ and $25\,W$ were chosen for q_i. However, inverse analysis results display a very low value for the estimated internal heat flow, as suggested in

Section 3.3.2.1 and as shown by results in Figure 6.8 - Figure 6.10 related to the cases 3, 9 and 15 (see Table 3-1) which were chosen as examples.

Normal Load: 1500 N

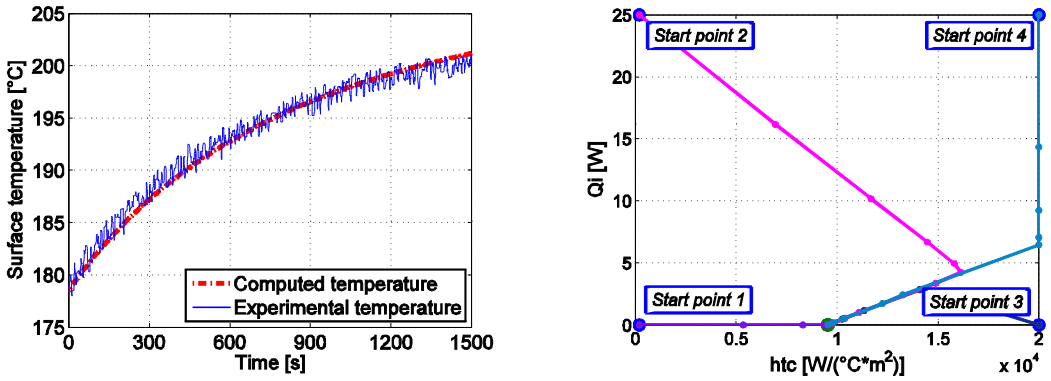

a) b)

Figure 6.8: Inverse analysis results for Case 3:
a) comparison between temperatures; b) convergence curves.

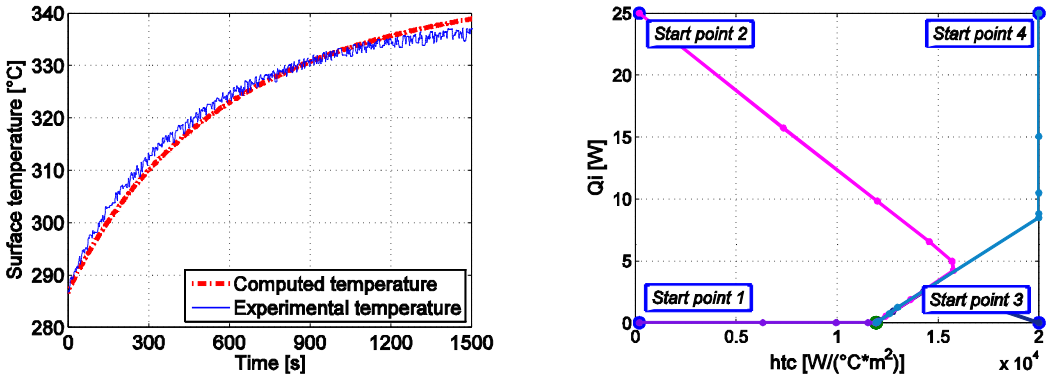

a) b)

Figure 6.9: Inverse analysis results for Case 9:
a) comparison between temperatures; b) convergence curves.

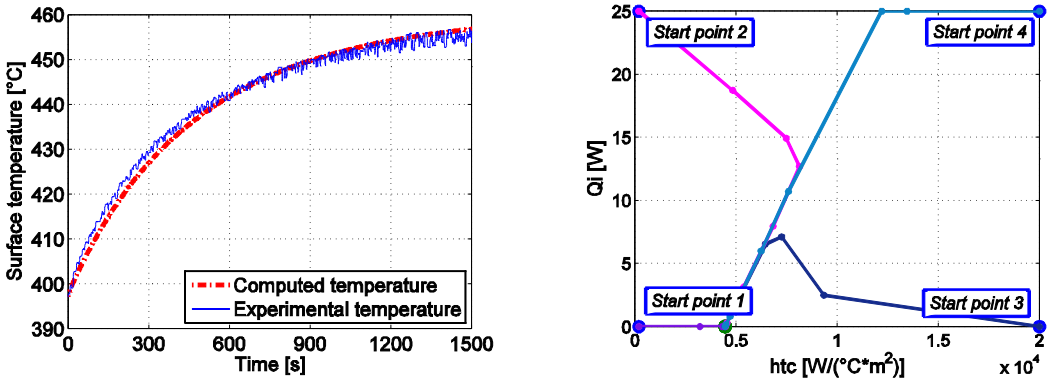

a) b)

Figure 6.10: Inverse analysis results for Case 15:
a) comparison between temperatures; b) convergence curves.

For this reason, the q_i value was sought in a reduced field nearby the 0 value. The maximum value of the internal flow was fixed, then, at $0.25\ W$. This allows to achieve a more refined q_i estimation and, above all, it allows to check the q_i influence on the *htc* characterization.

The inverse analysis algorithm relies on the contact area estimation presented in the previous sections, so the reliability of the inverse analysis results is strongly influenced by the reliability of the FEM solution. In any case, the aim of these activities is not that of supplying an exact value for the *htc*, but to show the applicability and the potentiality of the developed methodology for the *htc* evaluation. Nevertheless, for the reasons stated in the previous sections, the approximations introduced in the models are indeed small enough to be able to consider the obtained results as good approximations of the exact values.

6.3.1. Heat transfer coefficient

In this section, inverse analysis results are presented as gathered according to hot disc temperature. So, referring to the experimental campaign presented in Section 3.3.2, three clusters of results are introduced, for hot disc temperature of 400 °C, 600 °C and 800 °C.

6.3.1.1. Hot disc temperature of 400 °C

The inverse analysis results referring to the 400 °C cases are summarized in Table 6-2. For the first six cases presented in Table 3-1, equivalent to the cases presented in Table 6-2, the comparison between the experimental results and the inverse analysis solution are shown respectively in Figure 6.11a - Figure 6.16a. Instead, the four convergence curves starting from the extremities of the bi-dimensional parameter space are shown for each single case in Figure 6.11b - Figure 6.16b.

The comparisons between experimental and measured temperatures highlight the capability of the analytical solution to replicate the experimental temperature increase. However, the model cannot interpret perfectly the experimental data, due to the introduced approximations; in

particular, this holds true for the radiative heat fluxes estimation. This behavior tends to be more evident when the temperature increase of the cold disc becomes important. Results show how, in general, the implemented algorithm is able to identify a solution which can be considered as the global minimum of the inverse problem. Referring to the results, the found minima show a dependency for the *htc* on the normal load; instead, the algorithm found values for the q_i nearby 0 in almost all cases. In case 3 and 4, different minima were found (equivalent to different values of q_i) and this is probably caused by experimental data noise, as better discussed below. Anyway, no significant variation for the *htc* characterization is detectable in the results.

Hot disc temperature	Normal Load [N]	Case	Start point			Solution		Residual
			n.	htc [W/°C*m^2]	qi [W]	htc [W/°C*m^2]	qi [W]	
400 °C	500	1	1	200	0,0025	**6823**	0,0005	5,17E-02
			2	20000	0,0025	**6834**	0,0063	5,20E-02
			3	200	0,2500	**6828**	0,0031	5,18E-02
			4	20000	0,2500	**6895**	0,0397	5,35E-02
	1000	2	1	200	0,0025	**10033**	0,0001	9,87E-02
			2	20000	0,0025	**10193**	0,1008	1,04E-01
			3	200	0,2500	**10033**	0,0000	9,87E-02
			4	20000	0,2500	**10033**	0,0000	9,87E-02
	1500	3	1	200	0,0025	**9671**	0,0002	5,31E-02
			2	20000	0,0025	**9836**	0,1103	5,64E-02
			3	200	0,2500	**9712**	0,0275	5,39E-02
			4	20000	0,2500	**9671**	0,0000	5,31E-02
	2000	4	1	200	0,0025	**11995**	0,0011	4,75E-02
			2	20000	0,0025	**12242**	0,1737	4,69E-02
			3	200	0,2500	**12264**	0,1885	4,69E-02
			4	20000	0,2500	**12352**	0,2500	4,69E-02
	2500	5	1	200	0,0025	**15315**	0,0002	3,22E-01
			2	20000	0,0025	**15316**	0,0000	3,22E-01
			3	200	0,2500	**15346**	0,0190	3,23E-01
			4	20000	0,2500	**15316**	0,0002	3,22E-01
	3000	6	1	200	0,0025	**15430**	0,0003	2,14E-01
			2	20000	0,0025	**15489**	0,0370	2,15E-01
			3	200	0,2500	**15434**	0,0013	2,14E-01
			4	20000	0,2500	**15432**	0,0001	2,14E-01

Table 6-2: Inverse analysis results for 400 °C of hot disc temperature.

Hot disc temperature: 400 °C

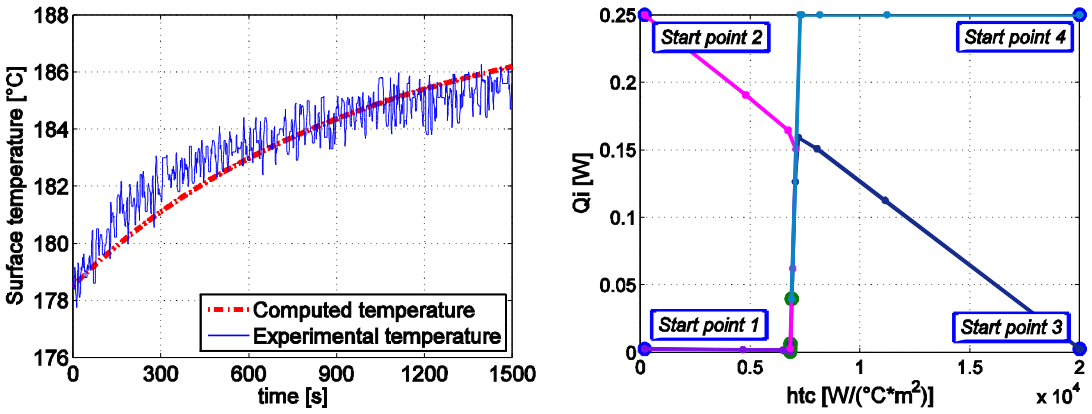

a) b)

Figure 6.11: Inverse analysis results for Case 1:
a) comparison between temperatures; b) convergence curves.

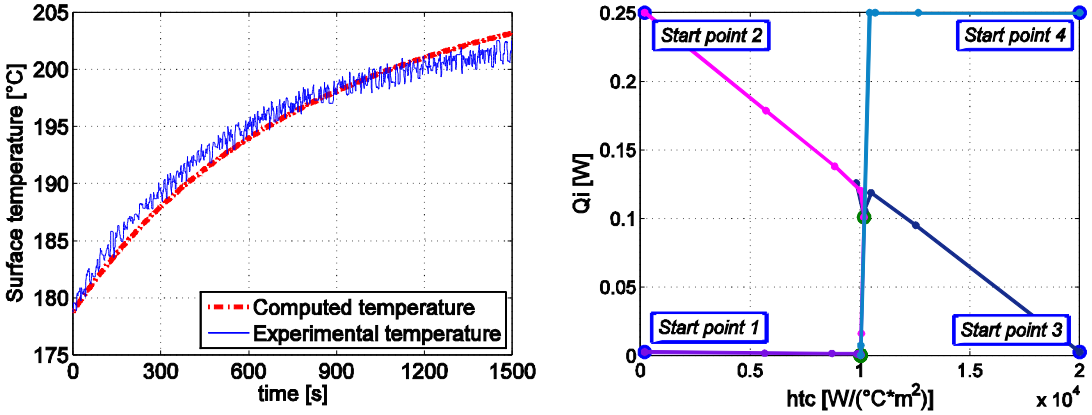

a) b)

Figure 6.12: Inverse analysis results for Case 2:
a) comparison between temperatures; b) convergence curves.

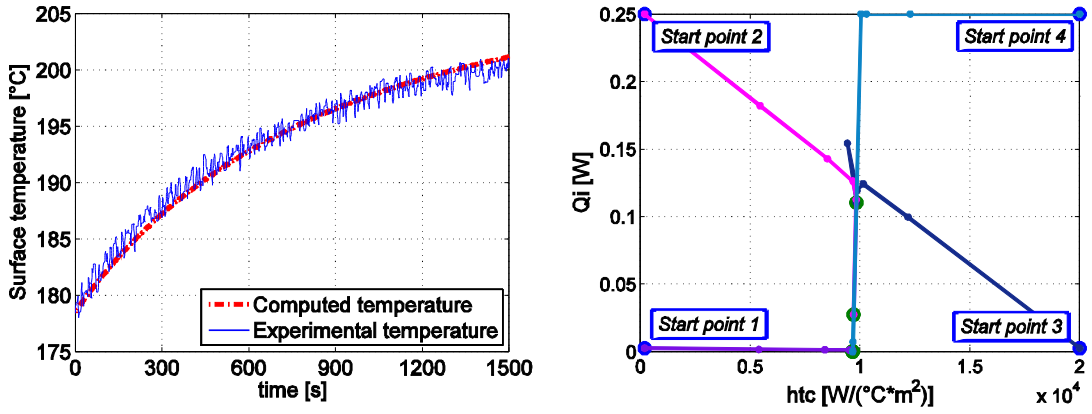

a) b)

Figure 6.13: Inverse analysis results for Case 3:
a) comparison between temperatures; b) convergence curves.

Hot disc temperature: 400 °C

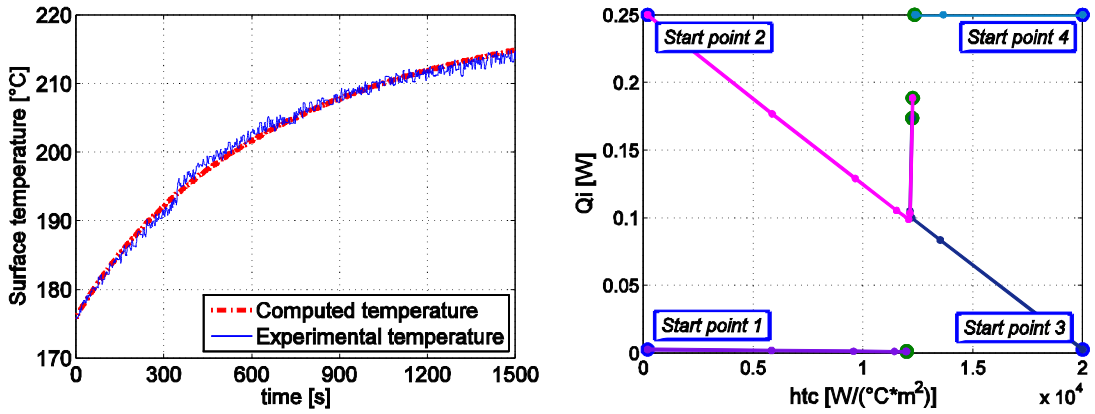

a) b)

Figure 6.14: Inverse analysis results for Case 4:
a) comparison between temperatures; b) convergence curves.

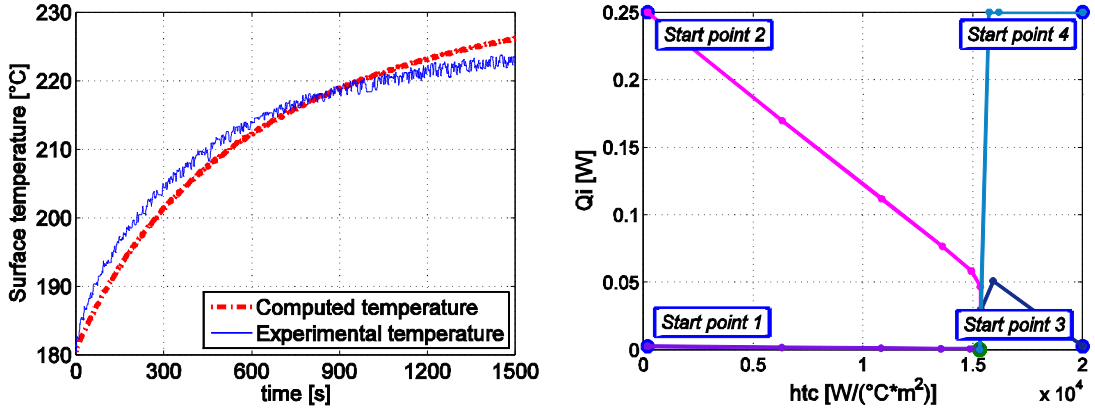

a) b)

Figure 6.15: Inverse analysis results for Case 5:
a) comparison between temperatures; b) convergence curves.

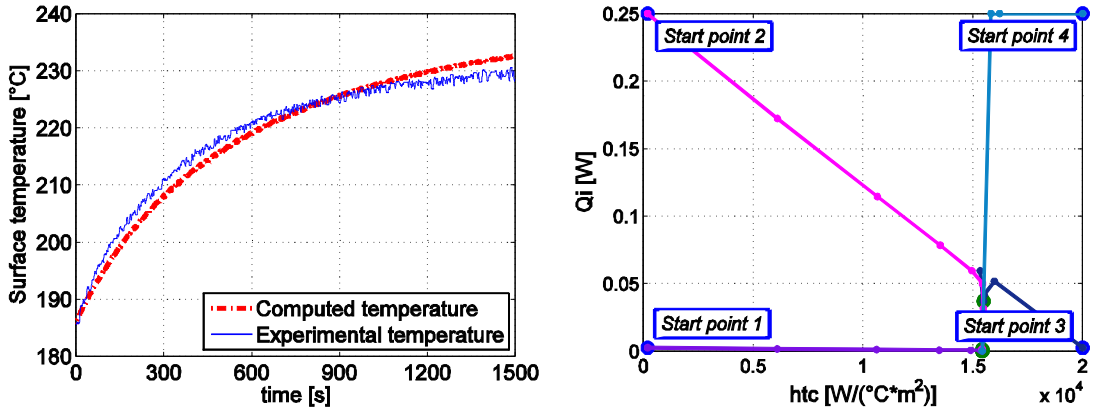

a) b)

Figure 6.16: Inverse analysis results for Case 6:
a) comparison between temperatures; b) convergence curves.

6.3.1.2. Hot disc temperature of 600 °C

The inverse analysis results referring to 600 °C cases are summarized in Table 6-3. For these cases, the comparison between the experimental results and the inverse analysis solution are shown respectively in Figure 6.17a - Figure 6.22a. Instead, the four convergence curves starting from the extremities of the bi-dimensional parameter space are shown for each case in Figure 6.17b - Figure 6.22b.

Considerations made for the previous cluster are valid also for the present test conditions.

Hot disc temperature	Normal Load [N]	Case	Start point			Solution		Residual
			n°	htc [W/°C*m^2]	qi [W]	htc [W/°C*m^2]	qi [W]	
600 °C	500	7	1	200	0,0025	**7809**	0,0008	3,31E-02
			2	20000	0,0025	**7815**	0,0062	3,31E-02
			3	200	0,2500	**7902**	0,0787	3,42E-02
			4	20000	0,2500	**8107**	0,2500	3,70E-02
	1000	8	1	200	0,0025	**8318**	0,0009	3,49E-02
			2	20000	0,0025	**8439**	0,1348	3,72E-02
			3	200	0,2500	**8401**	0,0930	3,65E-02
			4	20000	0,2500	**8544**	0,2500	3,94E-02
	1500	9	1	200	0,0025	**11925**	0,0003	8,14E-02
			2	20000	0,0025	**11926**	0,0002	8,14E-02
			3	200	0,2500	**11952**	0,0290	8,22E-02
			4	20000	0,2500	**11925**	0,0000	8,14E-02
	2000	10	1	200	0,0025	**12245**	0,0003	1,25E-01
			2	20000	0,0025	**12288**	0,0528	1,26E-01
			3	200	0,2500	**12274**	0,0360	1,26E-01
			4	20000	0,2500	**12245**	0,0000	1,25E-01
	2500	11	1	200	0,0025	**14007**	0,0001	2,80E-02
			2	20000	0,0025	**14050**	0,0538	2,84E-02
			3	200	0,2500	**14019**	0,0154	2,81E-02
			4	20000	0,2500	**14206**	0,2500	3,00E-02
	3000	12	1	200	0,0025	**16028**	0,0002	2,75E-01
			2	20000	0,0025	**16032**	0,0005	2,75E-01
			3	200	0,2500	**16030**	0,0006	2,75E-01
			4	20000	0,2500	**16030**	0,0001	2,75E-01

Table 6-3: Inverse analysis results for 600 °C of hot disc temperature.

Hot disc temperature: 600 °C

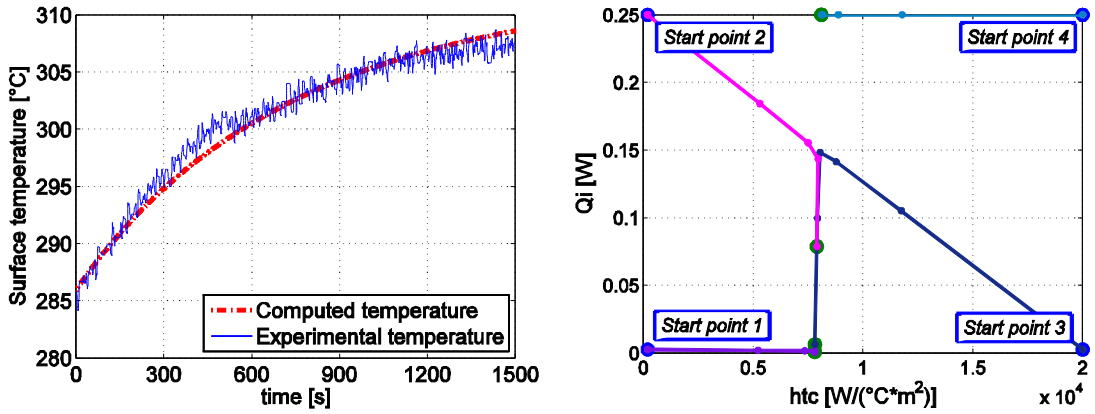

a) b)

Figure 6.17: Inverse analysis results for Case 7:
a) comparison between temperatures; b) convergence curves.

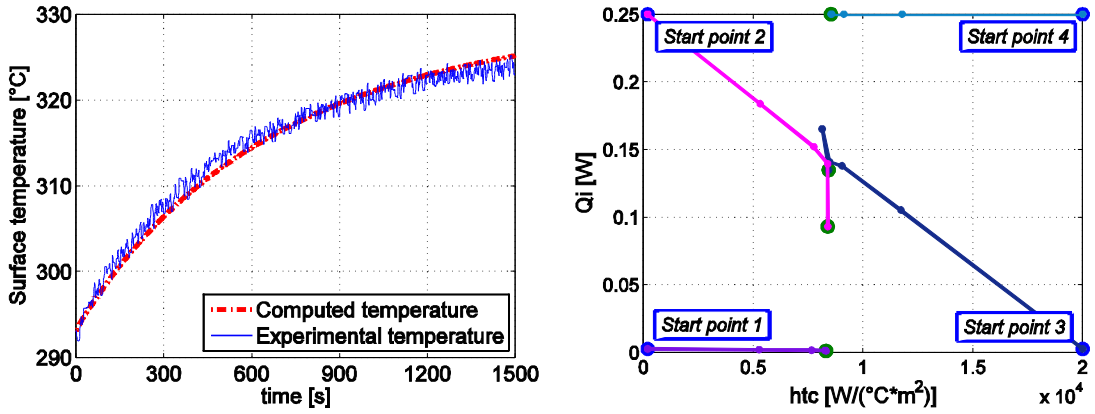

a) b)

Figure 6.18: Inverse analysis results for Case 8:
a) comparison between temperatures; b) convergence curves.

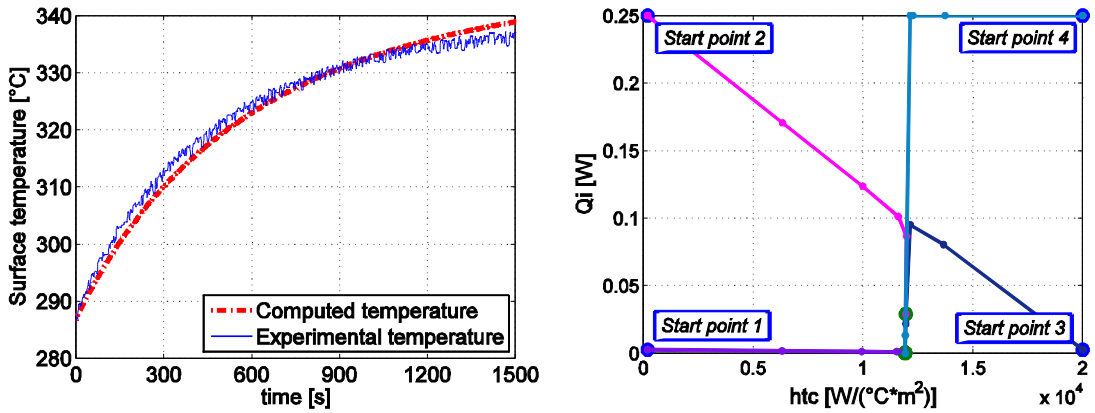

a) b)

Figure 6.19: Inverse analysis results for Case 9:
a) comparison between temperatures; b) convergence curves.

Hot disc temperature: 600 °C

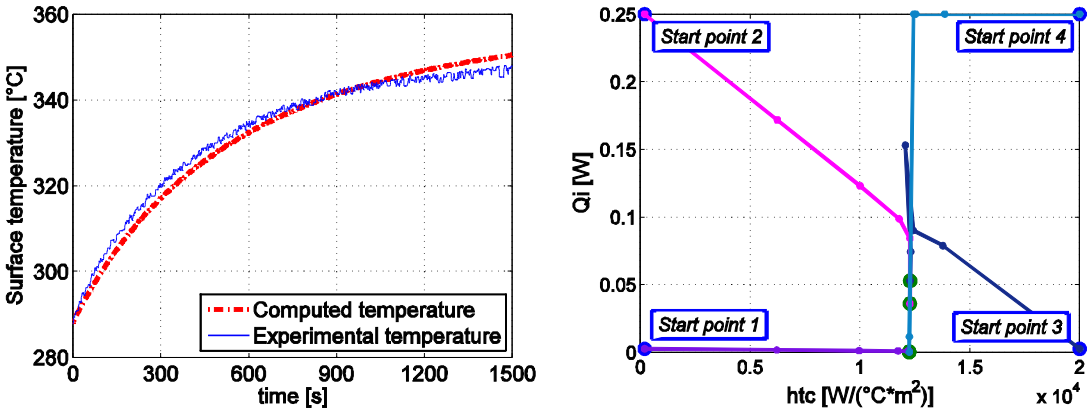

a) b)

Figure 6.20: Inverse analysis results for Case 10:
a) comparison between temperatures; b) convergence curves.

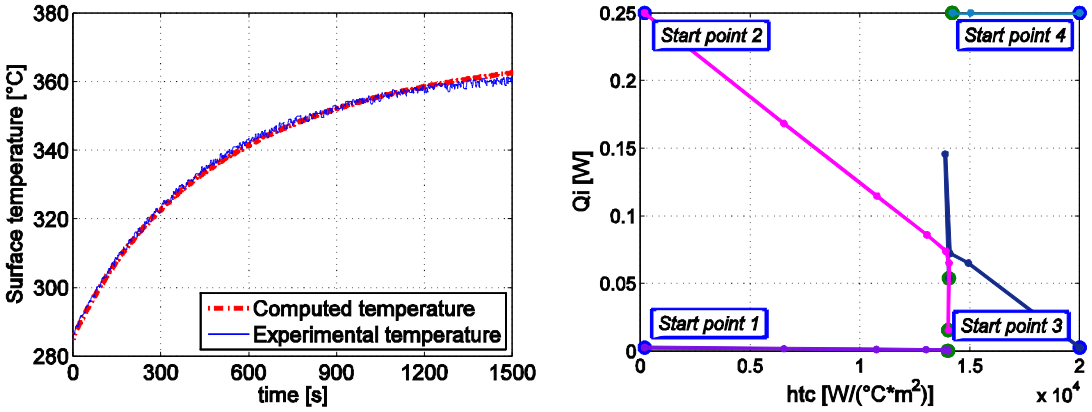

a) b)

Figure 6.21: Inverse analysis results for Case 11:
a) comparison between temperatures; b) convergence curves.

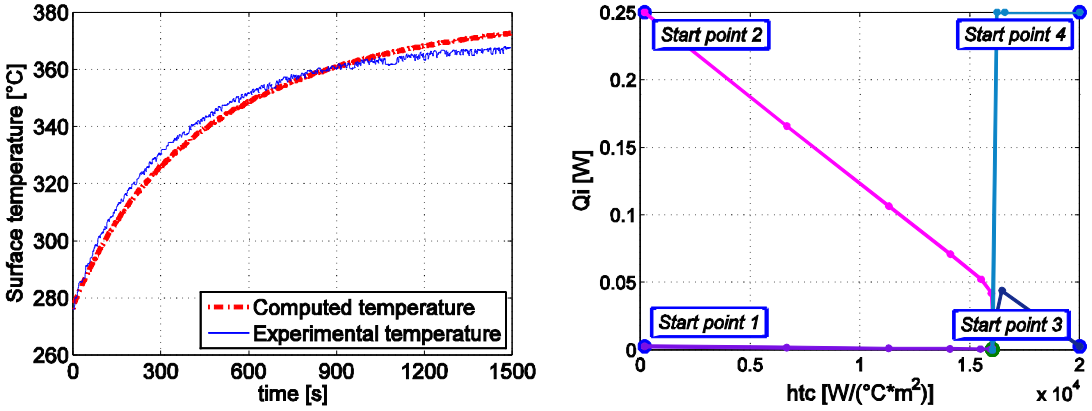

a) b)

Figure 6.22: Inverse analysis results for Case 12:
a) comparison between temperatures; b) convergence curves.

6.3.1.3. Hot disc temperature of 800 °C

The inverse analysis results referring to 800 °C cases are summarized in Table 6-4. The comparison between experimental results and inverse analysis solution are shown respectively in Figure 6.23a - Figure 6.27a. Instead, convergence curves from the extremities of the bi-dimensional parameter space are shown for each case in Figure 6.23b - Figure 6.27b.

Considerations made for the first cluster are valid also the present test conditions.

Hot disc temperature	Normal Load [N]	Case	Start point			Solution		Residual
			n°	htc [W/°C*m^2]	qi [W]	htc [W/°C*m^2]	qi [W]	
800 °C	500	13	1	200	0,0025	**4350**	0,0000	3,22E-02
			2	20000	0,0025	**4459**	0,1781	3,61E-02
			3	200	0,2500	**4354**	0,0061	3,24E-02
			4	20000	0,2500	**4353**	0,0002	3,22E-02
	1000	14	1	200	0,0025	**4349**	0,0001	1,12E-02
			2	20000	0,0025	**4420**	0,1858	1,27E-02
			3	200	0,2500	**4361**	0,0309	1,14E-02
			4	20000	0,2500	**4352**	0,0002	1,12E-02
	1500	15	1	200	0,0025	**4465**	0,0001	4,09E-02
			2	20000	0,0025	**4516**	0,1759	4,39E-02
			3	200	0,2500	**4471**	0,0203	4,12E-02
			4	20000	0,2500	**4465**	0,0000	4,09E-02
	2000	16	1	200	0,0025	**5075**	0,0004	4,97E-02
			2	20000	0,0025	**5075**	0,0010	4,97E-02
			3	200	0,2500	**5086**	0,0476	5,04E-02
			4	20000	0,2500	**5077**	0,0099	4,99E-02
	2500	17	1	200	0,0025	**4747**	0,0003	3,37E-01
			2	20000	0,0025	**4754**	0,0325	3,38E-01
			3	200	0,2500	**4753**	0,0271	3,38E-01
			4	20000	0,2500	**4748**	0,0000	3,37E-01

Table 6-4: Inverse analysis results for 800 °C of hot disc temperature.

Hot disc temperature: 800 °C

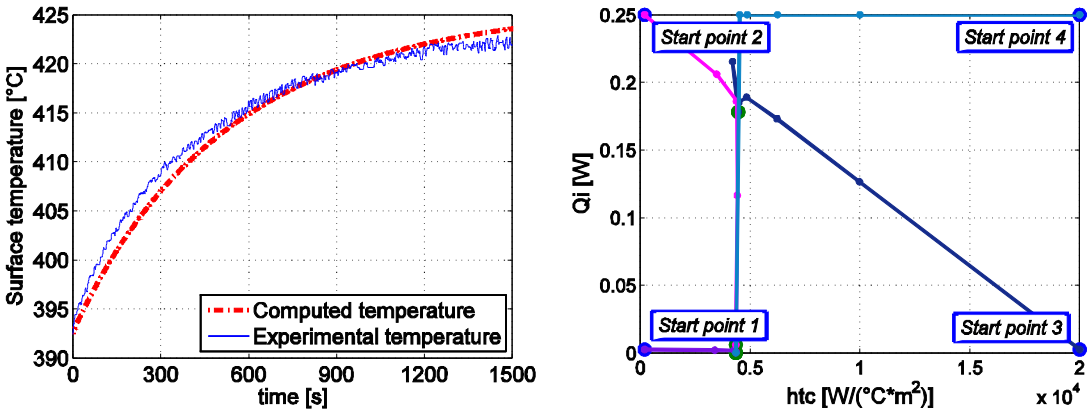

a) b)

Figure 6.23: Inverse analysis results for Case 13:
a) comparison between temperatures; b) convergence curves.

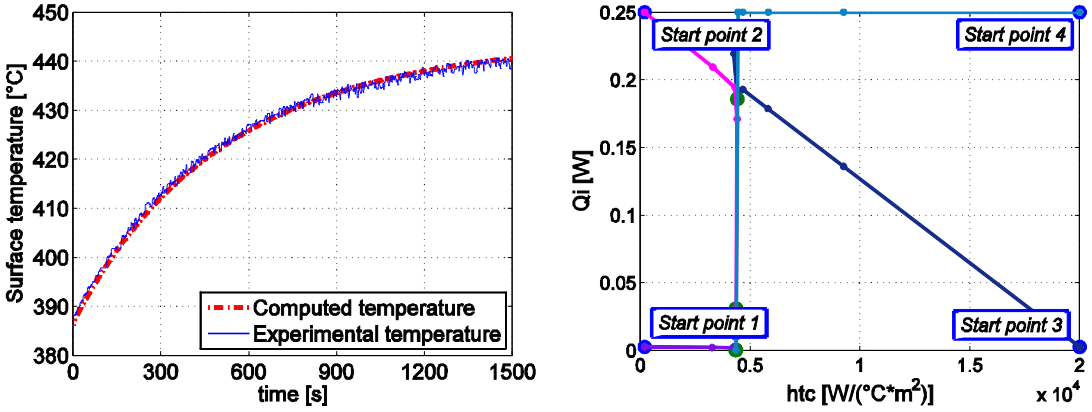

a) b)

Figure 6.24: Inverse analysis results for Case 14:
a) comparison between temperatures; b) convergence curves.

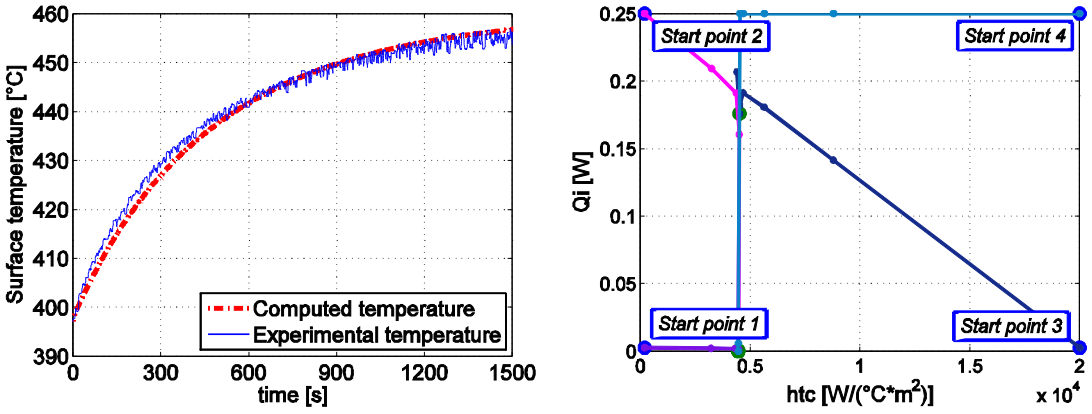

a) b)

Figure 6.25: Inverse analysis results for Case 15:
a) comparison between temperatures; b) convergence curves.

Hot disc temperature: 800 °C

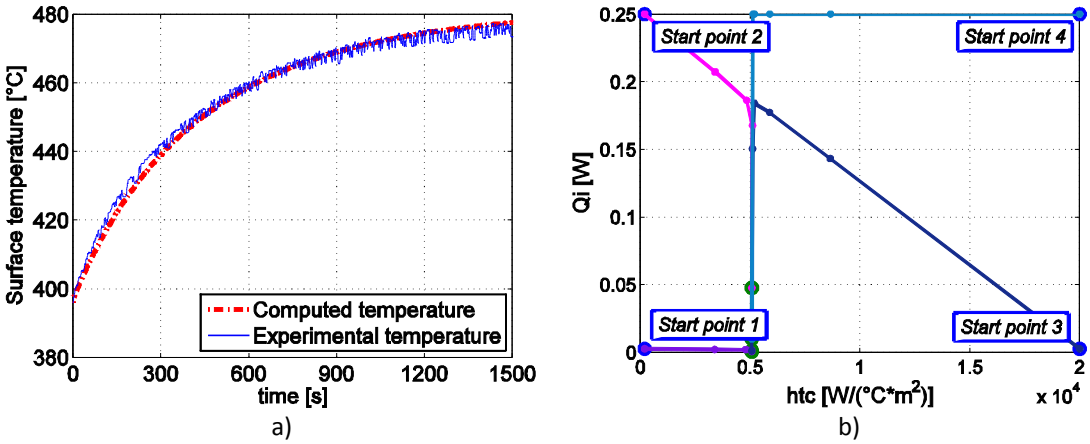

a) b)

Figure 6.26: Inverse analysis results for Case 16:
a) comparison between temperatures; b) convergence curves.

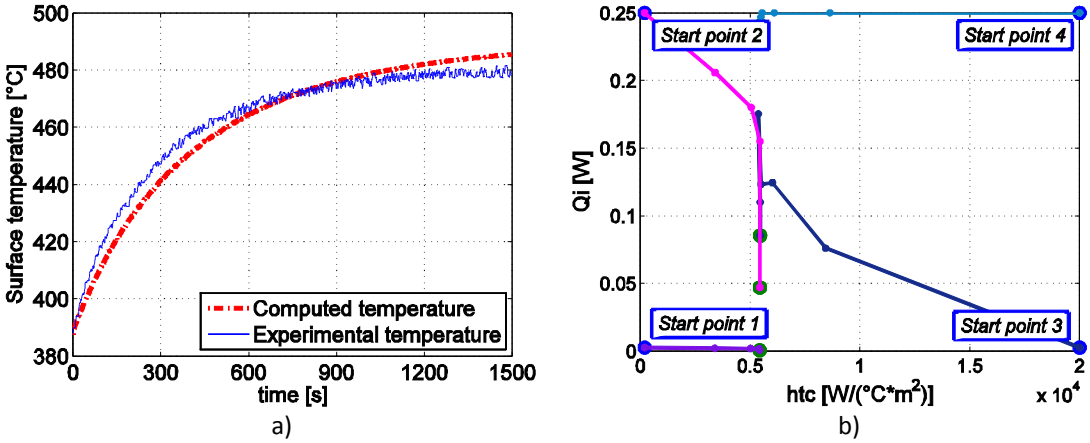

a) b)

Figure 6.27: Inverse analysis results for Case 17:
a) comparison between temperatures; b) convergence curves.

6.3.2. Considerations on the inverse analysis results

The results achieved through the inverse analysis are summarized and plotted in Figure 6.28 and Figure 6.29. The first figure shows the *htc* behavior for the three clusters of results and at different normal load, whereas the second one shows the internal flow behavior under the same conditions.

Looking at Figure 6.28, a similar behavior is detectable for the 400 °C and 600 °C clusters of results. Instead for the 800 °C cluster, a completely different behavior is visible. Indeed, for the first two clusters, a linear dependency of *htc* on the normal load is rather evident, while *htc*

appears to be constant with respect to the normal load for the third cluster. Moreover, for this cluster the *htc* value is much lower than for the previous cases. This marks another important difference for the behaviour at high temperature, as already remarked at the end of previous Section 6.2.

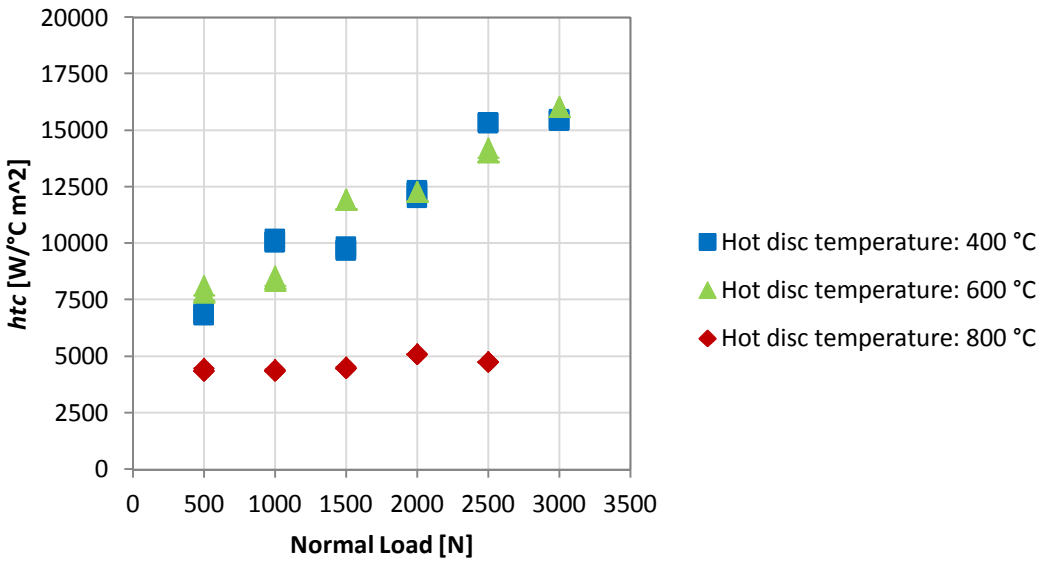

Figure 6.28: Summary of inverse analysis results: htc estimation.

Concerning the internal flow, Figure 6.29 shows how the algorithm computed a very low value, generally lower than 0.1 W, in almost all the inverse analysis runs This is an effect of the experimental procedure, which considers an initial steady state condition such as to provide a thermal equilibrium not only externally at the disc but also between the disc and its spindle, as suggested in Section 3.3.2.1. In addition, results showing a higher value of internal flow could be due to the noise presence in temperature measurements that can generate local minima nearby the global minimum. In any case, the few cases in which that internal flow displays "high" value (11 on total of 68 cases) are not sufficient to discredit the general trend shown by the other results. Moreover, these local minima are not able to modify the *htc* characterization; indeed, different internal flow estimations can lead only to *htc* modifications of one order of magnitude lower than that of the *htc*. Figure 6.29 does not show any dependency of internal flow on the normal load or on the hot disc temperature was detectable. This seems reasonable;

indeed these two parameters act on the external surface and, hence, are not able to modify the internal heat transfer.

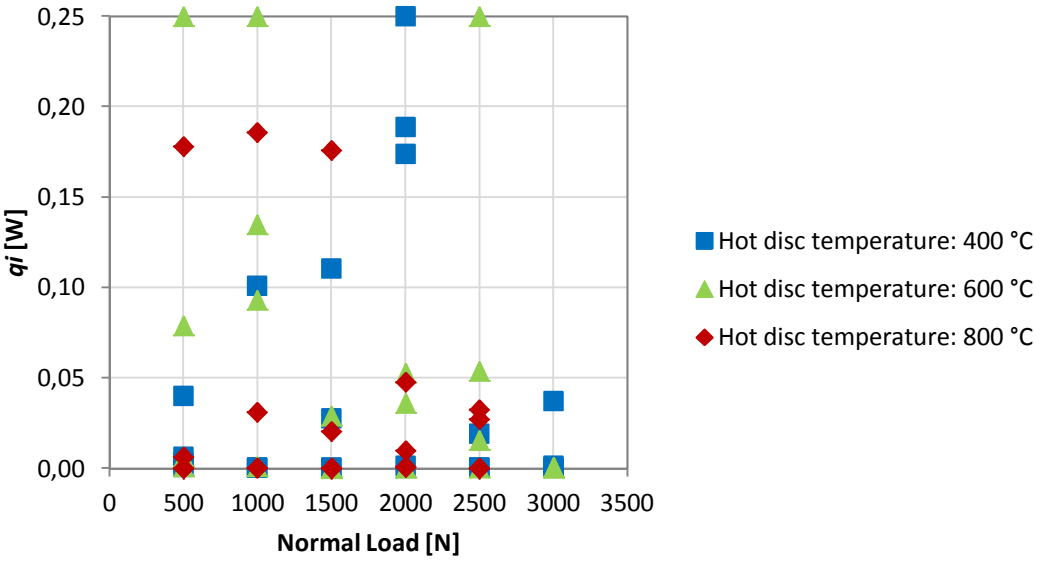

Figure 6.29: Summary of the inverse analysis results: internal heat flow estimation.

htc results can be plotted also in terms of resulting heat flow (q_c), as shown in Figure 6.30. The resulting flow was computed considering the FEM estimation of the contact area and of the initial temperature difference between the two discs.

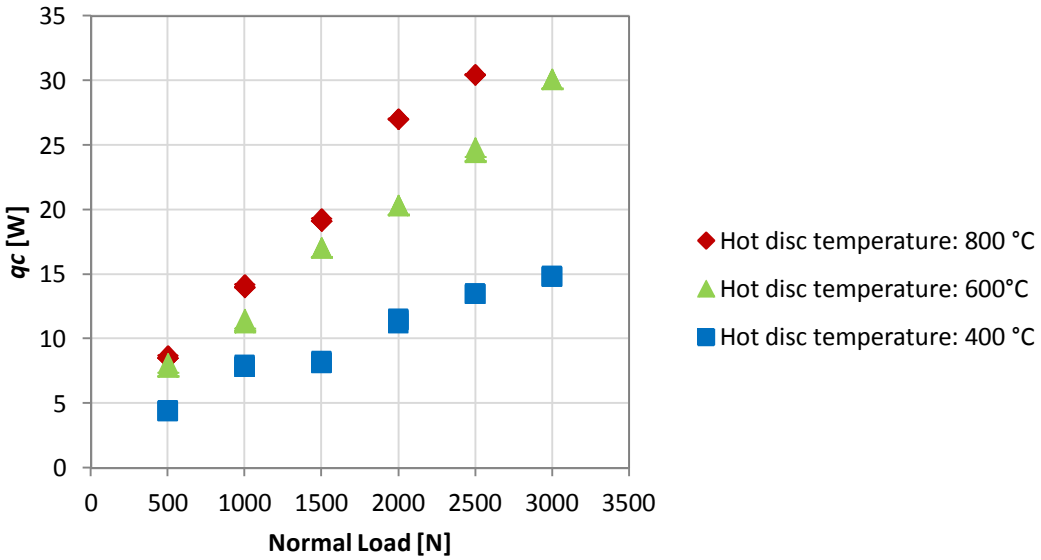

Figure 6.30: Contact heat flow.

The diagram in Figure 6.30 shows a linear dependency on the normal load for both the three hot disc temperatures and this trend appears more evident as the hot disc temperature increases. This result is in contradiction with the trend shown in Figure 6.28 in which, for the 800 °C cluster, the *htc* appears to be almost constant at a low value, independently on the normal load. However, as shown in Figure 6.7, the contact area at 800 °C is greater than for the other two cases and it increases strongly with the normal load increase. So, this explains the trends shown in Figure 6.30. Nevertheless, heat flows q_c plotted in the diagram are computed choosing arbitrarily a temperature difference Δu (indeed $q_c = htc \cdot \Delta u$) and, hence, they lead to possible misinterpretation, since they depend on the chosen cold disc temperature.

It is more interesting to plot the obtained *htc* as a function of the mean contact pressure, as done in the diagram shown in Figure 6.31. Even though the mean contact pressure is only evaluated through the FEM model, the achieved solution trend can be considered as a reliable representation of the real contact pressure trend. Hence, the resulting regression can be trusted despite both contact pressure and *htc* could be considered only as good approximations of their real values.

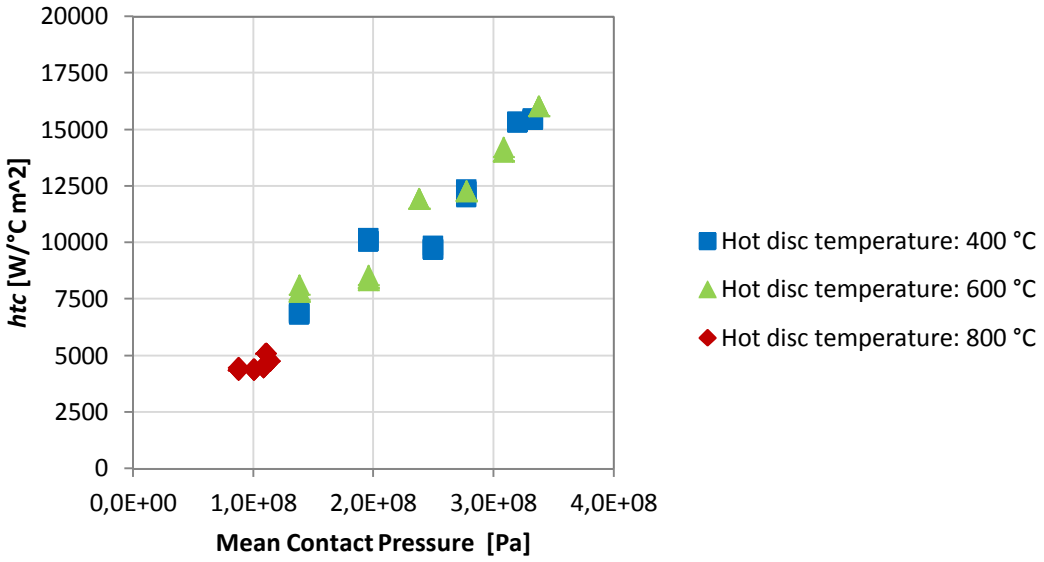

Figure 6.31: htc vs. mean contact pressure.

The diagram shows quite clearly a linear dependence between the *htc* and the mean contact pressure value. Indeed, both the three clusters of results are located almost along a straight line, although they come from different test conditions. The different test conditions promoted different contact conditions (in particular: for a hot disc temperature of 400 °C the contact was purely elastic, for the temperature of 600 °C was elastoplastic and, finally, for 800 °C the contact was basically plastic). However, the resulting *htc* seems to be strictly connected to the absolute value of the contact pressure, as suggested (qualitatively) by Chen in [22].

Even though further investigations would be needed, it is already possible to define a linear correlation for all the achieved data. Figure 6.32 shows how well a linear correlation would fit the inverse analysis results. Indeed, a coefficient of determination value (namely the number that indicates how well a model fits experimental data) of $R^2 = 0{,}965$ was found.

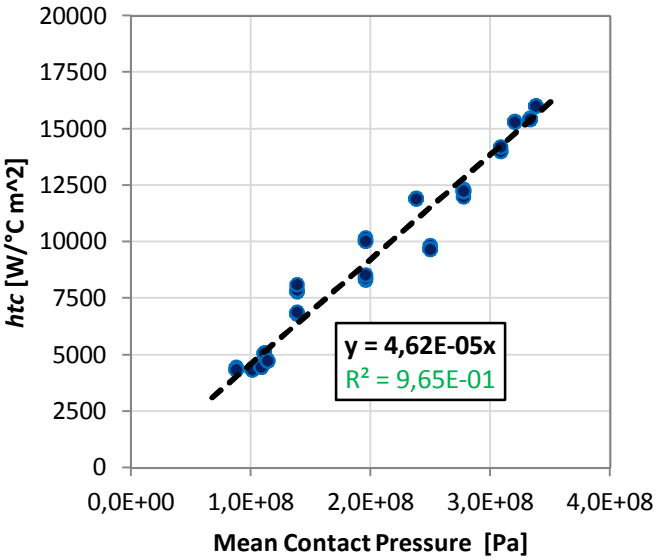

Figure 6.32: htc vs. mean contact pressure: linear regression.

It is interesting to note that the modulus of the straight line is, quantitatively, one order of magnitude lower than the modulus proposed by Chen [22], who suggested a value of about $5000\ \frac{W/(°C\ m^2)}{kg/mm^2} \approx 500\ \frac{W/(°C\ m^2)}{MPa}$ versus a value of $46\ \frac{W/(°C\ m^2)}{MPa}$ found here. However, the resulting *htc* values are in the same order of magnitude of the values obtained by Bryant and Chiu [17], on a full scale mill ($7000\ W/(°C\ m^2)$) and of the values acquired using a

research mill by Harding [47] ($2050\ W/(°C\ m^2)$ at 700 °C and $5100\ W/(°C\ m^2)$ at 1100 °C) and confirmed by Pietrzyk and Lenard [75]. In general, the results presented here are in agreement with the conclusions of Lenard [61], according to which $4000\ W/(°C\ m^2) \div 20000\ W/(°C\ m^2)$ appears to be the correct magnitude of *htc,* when hot rolling of steel occurs.

The *htc* value variability in hot rolling is strictly connected to the complexity of both the contact mechanical conditions and the temperatures of the contacting surfaces [61]. Both are difficult to be characterized due to the extreme environmental conditions. The present methodology allows to overcome most of the complications implied by real plant conditions, avoiding to get the typical data dispersion present nowadays in the literature. Hence, the present integrated experimental and numerical procedure allows to achieve *htc* characterizations that appear less scattered and more refined; moreover, it allows to relate *htc* values to the real contact conditions, which can be kept under control.

Since a dependency between *htc* and contact pressure is detected, it is worth noting that the *htc* achieved shall be considered as a mean value of the real *htc*. Indeed, in the contact region the contact pressure increases from zero to its maximum value and then decreases again to zero. Hence, considering the relationship between the *htc* and the contact pressure to be true, it means that the *htc* shall grow up from zero to its maximum value and then fall to zero again, in the same way as for the contact pressure. Since the *htc* was considered constant over the contact area (see Section 4.6.3), its computed values shall be considered as "mean values" and, from this point of view, it was properly correlated with the corresponding mean contact pressure. Assuming for the *htc* the same trend detected for the contact pressure along the contact arc, the supposed real value for the *htc* can be easily estimated. As it is shown in Figure 6.33, where the maximum *htc* value is plotted as a function of the corresponding contact pressure, the general relationship between these two parameters does not change.

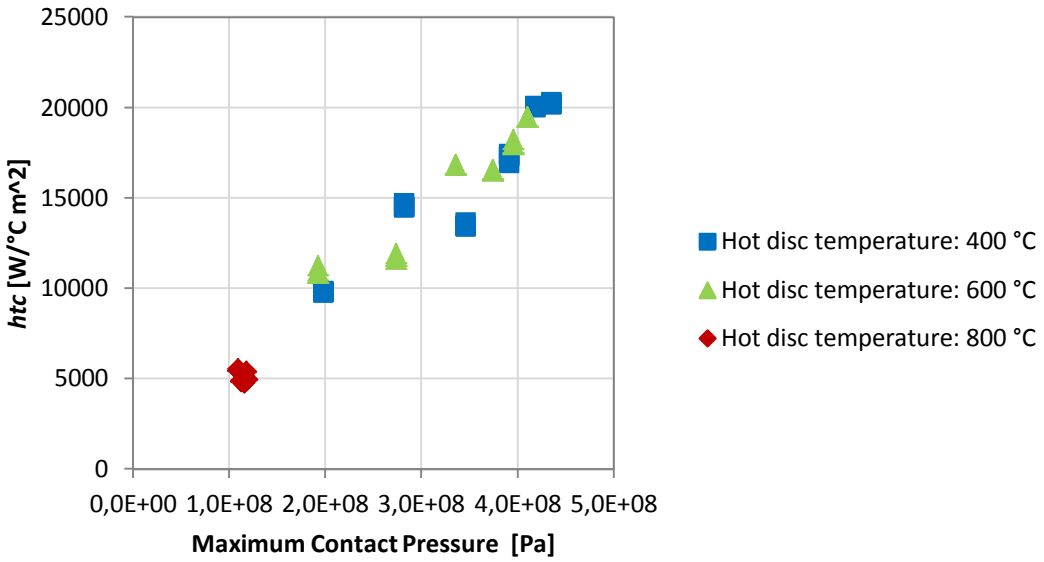

Figure 6.33: local htc vs. maximum contact pressure.

Indeed, values are basically shifted on both axes, but the general trend remains the same, as highlighted in Figure 6.34. If this consideration was further verified, it would mean that the linear correlation between *htc* and contact pressure is valid in terms of both spread value and localized value.

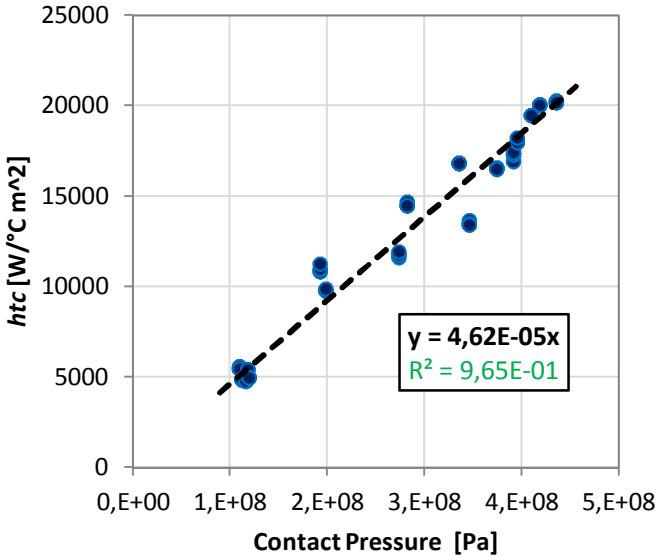

Figure 6.34: htc vs. maximum contact pressure: linear regression.

6.3.3. Further considerations

The developed methodology allows not only to achieve a precise characterization of the *htc* under real hot rolling conditions, but also to investigate the phenomenon of heat generated by friction and its impact on the contact conditions. Indeed, by simply adding a heat flux to the heat transfer by contact it is possible to analyze the friction impact on the surface temperature. At this stage, it is not thinkable to investigate frictional heat generation and to partition the phenomena. This would require additional devoted experimental activities. However, through the previously developed models, a first estimation of the surface temperature increase can be made when both contributions are present, in order to evaluate the thermal condition that the sample undergoes during a frictional test. So, it would be interesting to investigate the contribution of frictional heating with reference to frictional tests under piercing conditions.

Referring to the test presented in Section 3.3.1.4, the flash temperature can be assessed firstly through an estimation of the contact angle and contact pressure via the FEM model (see Section 6.2). From the latter parameter, the corresponding *htc* can be estimated by means of the just observed relationship; instead, from the former one, the area where contact heat transfer and frictional heat generation take place can be evaluated. Secondly, the surface temperature increase can be achieved by means of the analytical solution presented in Chapter 4. This solution requires an estimation of the two heat fluxes. The heat flux transferred by contact can be evaluated as:

$$q_c = htc(u_{HD} - u) \qquad (6.1)$$

where u_{HD} is the hot disc temperature and u is the cold disc temperature. The heat flux generated by friction can be assessed through a well-known formula:

$$q_f = \varpi \frac{\mu v N}{A_c} \qquad (6.2)$$

where μ is the experimental friction coefficient, v the sliding speed, N the applied normal load, A_c the contact area. As concluded by Francis and Kennedy [34], it is considered that nearly all the frictional energy ($\mu v N$) is dissipated as heat, primarily within the top few microns of the

contacting bodies. The coefficient ϖ describes how the heat generated is partitioned between the two bodies. This coefficient was fixed to a first approximation equal to 0.5. Through these fluxes, it is possible to estimate the flash temperature and the contribution of each flux to the surface temperature increase.

Referring to the contact condition characterized by 0,9 *m/s* of sliding speed and 2500 *N* of normal load, the local temperature increment is plotted in Figure 6.35. In particular, three different surface temperature increases are plotted: the blue line represents the temperature increase due only to the heat transfer by contact, the magenta line represents the increase owing to frictional heat generation, and the green one is the estimation of the superimposition of the two contributions. Looking at the diagram, it appears that, probably, a single effect alone is not able to promote significant surface variations. Even though friction heat generation represents the main contribution, the surface temperature increases significantly up to almost only 100 °C when frictional heat is considered together with contact heat.

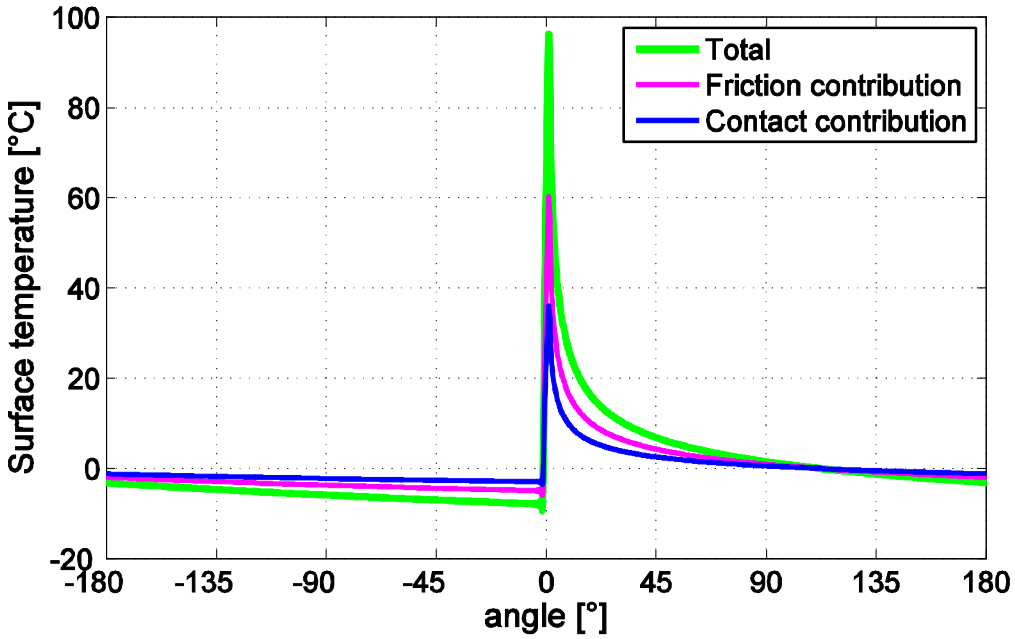

Figure 6.35: Surface temperature increment estimation for tribological test under piercing condition.

This increase could be high enough to support any localized surface modification. For example, looking at Figure 3.9, temperatures higher than 100 °C could determine a considerably

lower yield strength and a similar modification could be detected also for the other physical properties of the material. In the same way, it is well-known that some chemical reactions, as oxidation, are fostered by high temperature. As stated by Lenard [61], the effect of temperature on the magnitude of friction in hot working should not be separated from other phenomena. Hence, the resulting friction behavior cannot be considered as an independent phenomenon, but, actually, it is the result of the summation of effects due to all phenomena (mechanical, chemical, thermal, etc.), which take place at the interface of the contacting bodies. So, the characterization of the thermal condition is only the first stage to be reached for a full understanding of the tribological behavior of the two bodies in contact.

Chapter 7. Conclusions

The present research focused on the characterization of the main energy transfers typical of hot working processes, with specific reference to hot rolling in the industrial production of seamless pipes. The research was developed within a collaboration with an industrial partner and attempted to achieve both academic and industrial research goals.

Regarding the analysis of the mechanical energy transfer, a non-Coulombian friction model was characterized under the hot rolling condition. Experimental results achieved under nearly industrial plant conditions highlighted the validity of the Wanheim and Bay law [97] to model friction in hot processes. Moreover, experimental activities pointed out some key variables which affect the friction behavior. In particular, since high temperatures are able to promote chemical processes and/or to influence the material mechanical properties, an analysis on the thermal conditions must be performed, in order to deeply understand the different phenomena which take place within the contact area. This calls for a throughout investigation on heat transfer processes. For this reason, a dedicated experimental campaign was put in place to characterize a coefficient apt to describe the heat transferred by contact, namely the heat transfer coefficient *htc*. This kind of coefficient cannot be deduced directly from the experimental results, but it requires appropriate mathematical tools that were developed in the course of this work. In detail, the *htc* was determined through an inverse analysis procedure, implemented on purpose, which takes advantage of an innovative analytical solution simulating the phenomena that appear in the experimental tests at the tribometer scale, within an experimental facility that was developed during this research.

First of all, a new analytical solution was developed to mimic the physical processes occurring in the experimental configuration. Starting from the analytical solution of a theoretical

problem that sketches the real problem, an approximate effective solution was also achieved. The theoretical problem is basically the heat conduction problem applied to a rotating hollow cylinder exposed to internal and external convection and subjected to a concentrated heat flux on the outer boundary. Starting from the partial solutions of the problem available in the literature, a complete solution was ex-novo developed. Then, the solution was further simplified and optimized in order to achieve an efficient model without loss of accuracy. Indeed, a crucial aim of this activity was that of reaching a heat conduction solution able to solve the problem as quickly as possible. In this way, an inverse analysis procedure allows to identify the unknown *htc* in reasonable computational time. The achieved analytical solution has shown, indeed, very suitable for this purpose. However, it was necessary to modify it further, to include all thermal contributions to which the sample was subjected to. Thus, initial condition, air convective and radiation contributions were added to the final model, to replicate real test configuration conditions.

A dedicated inverse analysis algorithm was then implemented to attain a sufficiently accurate characterization of the *htc*. The inverse analysis algorithm integrates the analytical solution as the direct problem solution and minimizes the discrepancy between corresponding simulations and experimental results, in order to achieve the best solution for the *htc* for the considered problem. As most of Inverse Heat Transfer Problems (IHTPs), the analyzed problem shall be considered ill-posed, due to solution sensitivity to measurement errors. Therefore, signals were properly processed to avoid troubles related to measurement inaccuracies and, so, to bring back the considered IHTP to a common least mean square problem. Hence, a Trust region-Reflective algorithm was chosen to solve the resulting inverse problem in the fewest steps as possible.

Finally, the mathematical tools specifically developed were applied to process the experimental results obtained at the ring-on-ring tribometer scale. Through the inverse analysis, the *htc* and the internal heat flow between sample and spindle were estimated. The latter was

found to be of a small entity, as expected from experimental results. Instead, for the *htc* some interesting original trends were found. In particular, a linear relationship between the *htc* and the mean contact pressure were identified, in agreement with proposals by other authors.

The results allowed to estimate the flash temperature for the mechanical energy transfer tests. The found temperature peak in the contact area was such to condition the frictional behavior promoting chemical reactions or localized decreases of mechanical properties. In effect, tribology appears as an interdisciplinary subject, which draws from the expertise of several academic subjects (among these, the most important are: mechanical engineering, physics, chemistry and material science). Hence, in conclusion, for a full understanding of a tribological behavior like that analyzed in the present work, a mono-disciplinary approach looks insufficient. Indeed, all phenomena (mechanical, thermal, chemical and so on) taking place in the contact area shall be truly taken into account, as it has been attempted successfully in the present thesis.

Through the present work, innovative approaches were advanced to analyze both frictional behavior and heat transfer by contact under extreme mechanical and thermal contact conditions typical of hot rolling production process of seamless pipe.

Thanks to a newly designed tribometer and to the developed experimental methodologies, it has been possible to analyze, and keep under control, contact conditions typical of the hot working plant. Due to the difficulties in replicating industrial conditions and to carry out reliable measurements, knowledge in this field is often related to theoretical considerations supported by experimental tests performed either in laboratories, but under conditions rather far from those of the industrial process, or directly in the plant, but whose experimental results usually involve data deeply affected by rough systematic errors, uncertainties, scattering, etc., as typical of industrial environments. By replicating the process under controlled laboratory plant conditions, it is possible to measure and analyze directly the frictional behavior under these working conditions. Moreover, all phenomena interconnected to friction can be investigated, by reaching a deeper knowledge on the tribological occurrences that take place in an industrial plant.

The present work focused particularly on the thermal condition analysis. Anyway, the produced effort represents actually the beginning of a wider research activity aimed at characterizing all occurrences that may affect heat transfer phenomena in hot rolling processes. Through the developed mathematical tools, it is now possible to analyze in details several aspects that have not been considered so far. For instance, material couplings, surface conditions and the contact time are all topics that may deserve further examination. Additionally, the present integrated experimental and numerical approach shall allow to extend the investigation to the thermal effect due to friction. Indeed, the mechanical energy converted into thermal energy, the heat partition, etc. can now be assessed together with their effects on the surface temperature. Thereafter, the impact of the temperature variation on the contact conditions may be explored. Indeed, thermal analyses constitute only an intermediate, but essential, step in the investigation of the tribological conditions occurring during hot rolling processes in industrial plants.

References

[1] Abramowitz M., Stegun I.A. (1964). *Handbook of Mathematical Functions with Formulas, Graphs and Mathematical Tables*. National Bureau of Standards Applied Mathematics Series (55). U.S. Government Printing Office, Washington, D.C.

[2] Alifanov O.M. (1994). *Inverse Heat Transfer Problems*. Springer-Verlag, New York.

[3] Alilat N., Baïri A., Laraqi N. (2004). *Three-dimensional calculation of temperature in a rotating disk subject to an eccentric circular heat source and surface*. Numerical Heat Transfer, Part A, 46(2): 167-180.

[4] Amontons G. (1699). *De la Résistance Causeée dans les Machines*. Mémoires de l'Académie Royale, A: 257-282.

[5] Archard J.F. (1957). *Elastic deformation and the laws of friction*. Proceedings of the Royal Society of London. Series A, Mathematical and Physical Sciences, 243(1233): 190-205.

[6] Archard J.F. (1958/59). *The temperature of rubbing surfaces*. Wear, 2(6): 438-455.

[7] Arizzi F., Rizzi E. (2014). *Elastoplastic parameter identification by simulation of static and dynamic indentation tests*. Modelling and Simulation in Materials Science and Engineering, 22(3): 035017.

[8] Atefi G., Abdous M.A., Ganjehkaviri A. (2008). *Analytical solution of temperature field in hollow cylinder under time dependent boundary condition using Fourier series*. American Journal of Engineering and Applied Sciences, 1(2): 141-148.

[9] Barber J.R. (1969). *The conduction of heat from sliding solids*. International Journal of Heat and Mass Transfer, 13(5): 857-869.

[10] Bartholomew-Biggs M.C. (2003). *A Newton method with a two-dimensional line search*. Advanced Modeling and Optimization, 5(3): 223–245.

[11] Bay N. (1986). *Frictional stress and normal stress in bulk metal forming processes*. Journal of Mechanical Working Technology, 14(2): 203-223.

[12] Beck J.V., Arnold K.J. (1977). *Parameter Estimation in Engineering and Science*. Wiley Interscience, New York.

[13] Beck J.V., Blackwell B., St. Clair C.R. (1985). *Inverse Heat Conduction: Ill-Posed Problems*. Wiley Interscience, New York.

[14] Beynon J.H. (1999). *Finite-element modelling of thermomechanical processing*. Philosophical Transactions of the Royal Society of London Series A, 357(1756): 1573-1587.

[15] Block H. (1963). *Flash temperature concept*. Wear, 6(6): 483-494.

[16] Bowden F.P., Tabor, D. (1950). *The Friction and Lubrication of Solids, Part I*. Revised edition: 1954 - Paperback edition: 1986, Clarendon Press, Oxford, UK.

[17] Bryant G.F., Chiu T.S.L. (1982). *Simplified roll-temperature model: convective cooling*. Metal Science, 9(1): 478-484.

[18] Bush A.W., Gibson R.D., Thomas T.R. (1975). *The elastic contact of a rough surface*. Wear, 35(1): 87-111.

[19] Carslaw H.S., Jaeger, J.C. (1959). *Conduction of Heat in Solids*, second edition. Clarendon Press, Oxford.

[20] Carter F.W. (1926). *The electric locomotive*. Proceedings - Institution of Civil Engineers, 221: 221-252.

[21] Chen W.L., Yang Y.C. (2010). *Inverse problem of estimating the heat flux at the roller/workpiece interface during a rolling process*. Applied Thermal Engineering, 30(10): 1247-1254.

[22] Chen W.C., Samarasekera I.V., Hawbolt E.B. (1993). *Fundamental phenomena governing heat transfer during rolling*. Metallurgical Transactions A, 24(6): 1307-1320.

[23] Christensen P., Everfelt H. and Bay N. (1986). *Pressure distribution in plate rolling*. Annals of the CIRP, 35(1): 141-146.

[24] Cinelli G. (1965). *An extension of the finite Hankel transform and applications*. International Journal of Engineering Science, 3(5): 539-559.

[25] Conn A.R., Gould N.I.M., Toint P.L. (2000). *Trust Region Methods*. MPS-SIAM Series on Optimization, Philadelphia.

[26] Cooper M.G., Mikic B.B., Yovanovich M.M. (1969). *Thermal contact conductance*. International Journal of Heat and Mass Transfer, 12(3): 279-300.

[27] Coulomb C.A. (1785). *Théorie des Machines Simples, en ayant regard au Frottement de leurs Parties, et a la Roideur des Cordages*. Mem. Math. Phys., X: 161-342.

[28] Czichos H. (1978). *Tribology - A Systems Approach to the Science and Technology of Friction, Lubrication and Wear*. Elsevier, Amsterdam.

[29] Des Ruisseaux N.R., Zerkle R.D. (1970). *Temperature in semi-infinite and cylindrical bodies subjected to moving heat sources and surface cooling*. ASME Journal of Heat Transfer, 92(3): 456-464.

[30] Devadas C., Samarasekera I.V., Hawbolt E.B. (1991). *The thermal and metallurgical state of steel strip during hot rolling: Part I. Characterization of heat transfer*. Metallurgical Transactions A, 22(2): 307-319.

[31] Dowson D. (1979). *History of Tribology*. Longman Group Limited, London.

[32] Euler L. (1750). *Sur la frottment des corps solides*. Memories de l'Accademie de sciences de Berlin: 122-148.

[33] Fenech H., Rohsenow W.M. (1963). *Prediction of thermal conductance of metallic surfaces in contact*. Journal of Heat Transfer, 85(1): 15-24.

[34] Francis E., Kennedy J. (1984). *Thermal and thermomechanical effects in dry sliding*. Wear, 100(1–3): 453-476.

[35] Frieberg C., Kneer R. (2008). *Determination of thermal contact resistance from transient temperature measurements*. International Journal of Heat and Mass Transfer, 51(5-6): 1017-1023.

[36] Gao J., Lee S.C., Xiaolan A., Nixon H. (2000). *An FFT-based transient flash temperature model for general three-dimensional rough surface contacts*. Journal of Tribology, 122(3): 519-523.

[37] Gecim B., Winer W. (1984). *Steady temperature in a rotating cylinder subject to surface heating and convective cooling*. Journal of Tribology, 106(1):120-126.

[38] Gecim B., Winer W. (1986). *Effect of a surface film on the surface temperature of a rotating cylinder*. Journal of Tribology, 108(1): 92-97.

[39] Gecim B., Winer W. (1986). *Steady temperatures in a rotating cylinder. Some variations in the geometry and the thermal boundary conditions*. Journal of Tribology, 108(3): 446-453.

[40] Goryacheva I.G. (1998). *Contact Mechanics in Tribology*. Kluwer Academic Publishers, Dordecht, The Netherlands.

[41] Gradeck M., Kouachi A., Borean J., Gardin P., Lebouche M. (2011). *Heat transfer from a hot moving cylinder impinged by a planar subcooled water jet*. International Journal of Heat and Mass Transfer, 54(25-26): 5527-5539.

[42] Greenwood J.A., Williamson J.B.P. (1966). *Contact of nominally flat surfaces.* Proceedings of the Royal Society of London. Series A, Mathematical and Physical Sciences, 295(1442): 300-319.

[43] Guo R. (1998). *Two-dimensional transient thermal behavior of work rolls in rolling process*. Journal of Manufacturing Science and Engineering - Transactions of the ASME, 120(1): 28-33.

[44] Hadamard J. (1923). *Lectures on Cauchy's Problem in Linear Partial Differential Equations*. Yale University Press, New Haven, Connecticut.

[45] Hahn D.W., Necati Ozisik M. (2012). *Heat Conduction*, third Edition. John Wiley & Sons, Inc., Hoboken, New Jersey.

[46] Hamraoui M., Zouaoui Z. (2009). *Modelling of heat transfer between two rollers in dry friction*. International Journal of Thermal Sciences, 48(6): 1243-1246.

[47] Harding R.A. (1976). *Temperature and Structural Changes in Hot Rolling*. Ph.D dissertation, University of Shaffield, Shaffield.

[48] Hertz H.R. (1882). *Über die Beruehrung elastischer Koerper*. Gesammelte Werke - Vol. 1, Leipzig.

[49] Hlady C.O., Brimacombe J.K., Samarasekera I.V., Hawbolt E.B. (1995). *Heat transfer in the hot rolling of metals*. Metallurgical and Materials Transactions B, 26(5): 1019-1027.

[50] Holman F.P. (2010). *Heat Transfer*, tenth Edition. McGraw Hill, New York.

[51] Hooke R. (1685). Discourse of carriage before the Royal Society, on Feb. 25, 1685. With a description of Stevi's Siling Chariot, made for prince of Orange. *Philosophical Experiments and Observation of the Late Eminent Dr. Robert Hooke (1726)*. W. Derham and J. Innys, London.

[52] Huang C., Ju T., Tseng A. (1995). *The estimation of surface thermal-behavior of the working roll in hot-rolling process*. International Journal of Heat and Mass Transfer, 38(6): 1019-1031.

[53] Jarger J.C. (1942). *Moving sources of heat and the temperature at sliding contacts*. Journal and Proceedings of the Royal Society of New South Wales, 76, Part III, Art. XVII: 203-224.

[54] Johnson K.L., Kendall K., Roberts A.D. (1971). *Surface energy and the contact of elastic solids*. Proceeding of Royal Society of London. Series A, Mathematical and Physical Sciences, 324(1558): 301-313.

[55] Jost P. (1966). *Lubrication (tribology) - A Report on the Present Position and Industry's Needs*. Department of Education and Science, HMSO, London.

[56] Juul N.H. (1982). *View factors in radiation between two parallel oriented cylinders of finite length*. Journal of Heat Transfer, 104(2): 384-388.

[57] Keanini K. (1998). *Inverse estimation of surface heat flux distributions during high speed rolling using remote thermal measurements*. International Journal of Heat and Mass Transfer, 41(2): 275-285.

[58] Krzyzanowski M., Beynon J.H., Farrugia D.C.J. (2010). *Oxide Scale Behaviour in High Temperature Metal Processing*. Wiley-VCH Verlag GmbH &Co., KGaA, Weinheim.

[59] Laraqia N., Alilat N., Garcia de Maria J.M., Baïri A. (2009). *Temperature and division of heat in a pin-on-disc frictional device - Exact analytical solution*. Wear, 266(7):765-770.

[60] Lee Y. (2004). *Rod and Bar Rolling: Theory and Application*. Marcel Dekker, Inc, New York.

[61] Lenard J.G. (2000). *Tribology in metal rolling keynote presentation forming Group F*. CIRP Annals - Manufacturing Technology, 49(2): 567-590.

[62] Lenard J.G. (2002). *Metal Forming Science and Practice - An Examination of the Coefficient of Friction*. Elsevier, Oxford.

[63] Madhusudana C.V. (1996). *Thermal Contact Conductance*, Springer-Verlag, New York.

[64] Marchi E., Zgrablich G. (1964). *Heat conduction in hollow cylinders with radiation*. Proc. of the Edinburgh Mathematical Society, 14(2): 159-164.

[65] MATLAB (2014). *Optimization Toolbox™ User's Guide*. Release 6.13. The MathWorks Inc., USA.

[66] Mikic B.B. (1974). *Thermal contact conductance: theoretical considerations*. International Journal of Heat and Mass Transfer, 17(2): 205-214.

[67] Montmitonnet P. (2006). *Hot and cold strip rolling processes*. Computer Methods in Applied Mechanics and Engineering, 195(48-49): 6604–6625.

[68] Nadai A. (1939). *The force required for rolling steel strip under tension*. Journal of Applied Mechanics ASME, 61: A54-A62.

[69] Necati Ozisik M., Orlande H.R.B. (2000). *Inverse Heat Transfer: Fundamentals and Applications*. Taylor & Francis, New York.

[70] Orowan E. (1943). *The calculation of roll pressure in hot and cold flat rolling*. Proceedings of the Institution of Mechanical Engineers, 150(1): 140-167.

[71] Osman T., Guenoun S., Boucheffa A. (2010). *Temperature field in a rotating roller subjected to interface heating*. The European Physical Journal of Applied Physics, 50(2): 1-12.

[72] Patula E.J. (1981). *Steady-state temperature distribution in a rotating roll subject to surface heat fluxes and convective cooling*. Journal of Heat Transfer, 103(1): 36-41.

[73] Persson B.N.J., Bucher F., Chiaia B. (2002). *Elastic contact between randomly rough surfaces: Comparison of theory with numerical results*. Physical Review B, 65(184106).

[74] Petersen S.B., Martins P.A.F., Bay N. (1997). *Friction in bulk metal forming: a general friction model vs. the law of constant friction*. Journal of Materials Processing Technology, 66(1): 186-194.

[75] Pietrzyk M., Lenard J.G. (1989). *A study of thermal-mechanical modeling of hot flat rolling*. Journal of Materials Shaping Technology, 7(2): 117-126.

[76] Popov V.L. (2010). *Contact Mechanics and Friction – Physical Principles and Applications*. Springer-Verlag, Berlin.

[77] Rabinowicz E. (1982). ASME/ASLE Lubrication Conference, Washington D/C/.

[78] Rabinowicz E. (1995). *Friction and Wear of Materials - second edition*. John Wiley and Sons, Inc., New York.

[79] Reynolds O.O. (1886). *On the theory of lubrication and its application to Mr. Beauchamp tower's experiments, including an experimental determination of the viscosity of olive oil*. Philosophical Transactions of the Royal Society of London, 177: 157-234.

[80] Roberts L. (1983). *Hot Rolling of Steel*. Marcel Dekker, New York.

[81] Rosenthal D. (1946). *The theory of moving sources of heat and its applications to metal treatments*. Transaction of the ASME, 68(11): 849-866.

[82] Rowe G.W. (1977). *Principles of Industrial Metalworking Processes*. Edward Arnold, London.

[83] Saboonchi A, Abbaspour A.M. (2004). *Changing the geometry of water spray on milling work roll and its effect on work roll temperature*. Journal of Materials Processing Technology, 148(1): 35-49.

[84] Samarasekera I.V. (1990). *The importance of characterizing heat transfer in the hot rolling of steel strip*. Proceedings of the Int. Symp. on the Mathematical Modelling of the Hot Rolling of Steel, 29th Annual Conference of Metallurgists: 145-167.

[85] Saunders N., Guo Z., Li X., Miodownik A.P., Schillé J.-P. (2003). *Using JMatPro to Model Materials Properties and Behavior*. Journal of The Minerals, Metals & Materials , 55(12): 60-65.

[86] Snedon I.N. (1972). *The Use of Integral Transform*. McGraw-Hill, New York.

[87] Steihaug T. (1983). *The conjugate gradient method and trust regions in large scale optimization*. SIAM Journal on Numerical Analysis, 20(3): 626-637.

[88] Tavasci A., Arizzi F., Rizzi E. (2013). *Friction coefficient measurements to assess tooling behaviour in hot rolling processes*. Proceedings of the 9th International and 6th European Rolling Conference.

[89] Tavasci A., Arizzi F., Dini D., Rizzi E. (2014). *Heat flux evaluation in high temperature ring-on-ring contacts*. Wear, accepted for publication.

[90] Tikhonov A.N., Arsenin V.Y. (1977). *Solution of Ill-Posed Problems*. Winston & Sons, Washington, DC.

[91] Tseng A., Chang J., Raudensky M., Horsky J. (1995). *An inverse finite element evaluation of roll cooling in hot-rolling of steels*. Journal of Materials Processing & Manufacturing Science, 3(4): 387-408.

[92] Vanden Berghen F. (2004). *Constrained, Non-linear, Derivative-free Parallel Optimization of Continuous, High Computing Load, Noisy Objective Functions*. Doctoral Thesis, University of Bruxelles.

[93] Volle F., Maillet D., Gradeck M., Kouachi A., Lebouche, M. (2009). *Practical application of inverse heat conduction for wall condition estimation on a rotating cylinder*. International Journal of Heat and Mass Transfer, 52(1-2): 210-221.

[94] Weisz-Patrault D., Ehrlacher A., Legrand N. (2012). *Evaluation of temperature field and heat flux by inverse analysis during steel strip rolling*. International Journal of Heat and Mass Transfer, 55(4): 629-641.

[95] Wanheim T (1973). *Friction at high normal pressure*. Wear, 25(2): 225-244.

[96] Wanheim T., Bay N., Petersen A.S. (1974). *A theoretically determined model for friction in metal working processes*. Wear, 28(2): 251-258.

[97] Wanheim T., Bay N. (1978). *A model for friction in metal forming processes*. Annals of the CIRP, 27(1): 189-194.

[98] Watson G.N. (1922). *A Treatise on the Theory of Bessel*. University Press, Cambridge.

[99] Watts R.G. (1969). *Temperature distributions in solid and hollow cylinders due to a moving circumferential ring heat source*. Journal of Heat Transfer, 91(4): 465-470.

[100] Williamson M., Majumdar A. (1992). *Effect of surface deformations on contact conductance*. Journal of Heat Transfer, 114(4): 802- 810.

[101] Wusatowski Z. (1969). *Fundamentals of Rolling*. Pergamon Press , Oxford.

[102] Yovanovich M.M., Schneider G.E. (1976). *Thermal constriction resistance due to a circular annular contact*. AIAA 14th Aerospace Sciences Meeting: 76-142.

[103] Yevtushenko A., Chapovska R. (1997). *Distribution of the friction heat between two stationary pins and a rotating disc*. Heat and Mass Transfer, 33(1-2): 59-65.

[104] Yevtushenko A., Tolstoj-Sienkiewicz J. (2006). *Distribution of friction heat between a stationary pin and rotating ring*. Archive of Applied Mechanics, 76(1-2): 33-47.

[105] Zhang G., Xiao H., Wang C. (2006). *Three-dimensional model for strip hot rolling*. Journal of Iron and Steel Research, International, 13(1): 23-26.

[106] Zhang J.Z., Xu C.X. (1999). *A class of indefinite dogleg path methods for unconstrained minimization*. SIAM Journal on Optimization, 9(3): 646–667.

[107] Zhang W., Bay N. (1997). *Numerical analysis of cross shear plate rolling*. Annals of the CIRP, 46(1): 195-200.

Appendix A: Seamless tube manufacturing processes

The advent of rolling mill technology and its development during the first half of the nineteenth century involved also the industrial manufacturing of tubes and pipes. Initially, rolled strips of sheet were formed into a circular cross section by funnel arrangements or rolls, and then butt or lap welded in the same heat (forge welding process). Towards the end of that century, various processes became available for the manufacture of seamless tubes and pipes, with production volumes rapidly increasing over a relatively short period at time. In spite of the application of other welding processes, the ongoing development and further improvement of seamless techniques led to welded tubes being almost completely pushed out of the market, with the result that seamless tubes and pipes dominated until World War Two. During the subsequent period, the results of research into welding technology led to a way back of the welded tube, with wide diffusion of numerous tube welding processes. Currently, around one third of the steel tube production in the world are accounted for by seamless processes. These are briefly described below, for further information on the industrial context of the present research work.

A.1. Seamless tube and pipe

Despite many earlier tests, trials and technologies, the invention of the cross roll piercing process by the Mannesmann brothers towards the end of the 1880s is regarded as the beginning of industrial seamless tube and pipe production.

This cross roll concept marked the first departure from the characteristic feature of all the rolling processes known until that time, i.e. the fact that the roll axes all lay in the same plane, the rolls are rotated in opposite directions and the stock exit speed is approximately equal to the roll circumferential speed. In the cross roll piercing process, the roll axes were arranged as parallel to the stock axis but at an angle to the stock plane. With the rolls rotating in the same direction, therefore, this arrangement produced a helical passage for the stock through the roll gap. Moreover, the exit speed was slower by about a power of 10 than the circumferential speed of the rolls.

By introducing a piercing plug arranged in the roll gap, the solid material could be pierced to produce a hollow shell in the rolling heat by the action of the cross rolls. However, it was not possible to produce yet tubes of normal wall thicknesses in useable lengths by the cross roll piercing process alone. It was only after the introduction and development of a second forming stage - the pilger rolling process - again by the Mannesmann brothers, that it became a practicable and economical way to manufacture seamless steel tubes. This pioneering development encouraged many inventors at the time to submit a number of patent applications, in some cases merely to circumvent the proprietary rights of the Mannesmann brothers, but also to break completely new ground in the manufacture of seamless tubes.

Among these, the so-called continuous mandrel rolling mill shall be mentioned. This process initially involved several two-high stands arranged in tandem by means of which the thin-walled hollow bloom was rolled over a mandrel bar to produce the finished tube. Owing to difficult mechanical engineering and driving problems, however, the process was soon confined to history. Fifty years later, with the advent of the modern technology to solve, in particular, the open-loop and closed-loop control problems, it was reborn as one of the most efficient ever invented tube rolling mills.

Moreover, as a result of the further development of individual forming facilities, new processes were also invented, such as the cross roll piercing mill derivatives in the form of the Assel and Diescher processes, or the tube extrusion process derived from the Ehrhardt press.

A.2. Piercing process

The blooms are heated in a rotary hearth furnace to a forming temperature of approximately 1280 °C. Following high-pressure water jet descaling, the bloom is pierced in the cross roll piercing mill to produce a thin-walled hollow shell, which is elongated to between 3 and 4.5 times its original length, corresponding to a deformation level between 65% and 75%.

The cross roll piercing mill type (Figure A.1) used in the plug mill is composed by two driven work rolls featuring a biconical pass, and their axes, which are likewise arranged parallel to the stock, are inclined to the horizontal of between 6° and 12°. The gap between the work rolls is extensively closed by a top and a bottom guide shoe. These guide shoes introduced by R.C. Stiefel contribute to the elongation process by acting as stationary rolls, so enabling the production of a relatively thin-walled hollow bloom. Again, the stock follows a helical line as it passes through the roll gap, so enabling the piercing mandrel, acting as an internal tool, to displace the material more effectively.

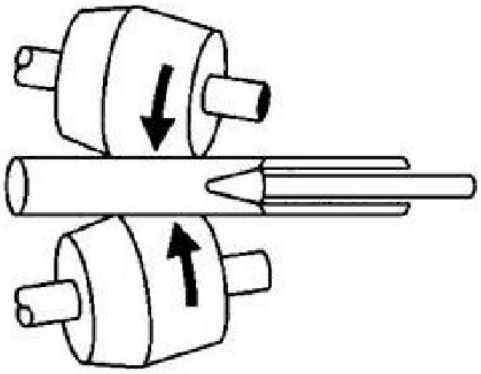

Figure A.1: Schematic representation of a cross roll piercing mill.

In plug mills employed for the manufacturing of large tube diameters, arranged between the barrel-type piercer and the plug stand a second piercing mill of the same design is frequently present. This is often described as “elongator”, the purpose of which is, in particular, to extend the inside and outside diameters and to further elongate the hollow shell.

In recent times, however, these two piercing mills have been replaced by heavy-duty plug mills, featuring just one cone piercing unit (Figure A.2). Here again, the work rolls feature a

biconical design. They are each angled at approximately 30° to the hollow bloom axis and inclined at approximately 10° to 12° to the horizontal. The roll gap is closed by means of two side discs which are also driven. This arrangement results in higher degrees of elongation, increased diameter expansion, and also faster hollow shell exit speeds (up to 1.5 m/s).

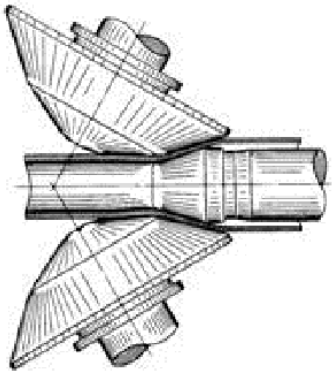

Figure A.2: Diagrammatic representation of a cone piercing mill.

The process of forming the hollow shell into the finished tube is performed in the same heat in the downstream plug stand, with processes and equipment that may take various forms. Among these, the continuous mandrel rolling process is worthy to be cited.

A.3. Rolling process

The continuous mandrel rolling process came as a result of arranging in tandem several graduated rolling passes in a series of rolling stands, to form a rolling line. This mill type elongated the hollow shell pierced in the piercing mill over a floating mandrel bar acting as the internal tool to produce the finished tube.

During the early period of development of this process, problems of material flow coordination tended to occur between the various stands, with the different rates of roll wear arising from stand to stand, further exacerbating the situation. Only with the advent of modern driving and control technologies has the continuous mandrel rolling mill been able to develop over the last few decades into today's high-performance production process. In the more modern mills of this type, the practice has been adopted whereby only one or two hollow shell/tube blank sizes are produced in the continuous rolling train, with the downstream stretch-reducing

mill finish-rolling them down. The wall thicknesses produced in this process range from 2 to 25 mm, depending on the outside diameter.

The starting material used takes the form of round billets, either rolled or cast. These are charged into the rotary hearth furnace where they are heated to the rolling temperature. Following high-pressure water descaling, the solid billet is pierced to produce a thin-walled hollow shell in a Stiefel-type cross roll piercing mill (automatic mill). In this process, the stock is elongated to between 2 and 4 times its original length, corresponding to a reduction in the cross section of 50% to 75%. Nowadays, driven guide discs (so-called Diescher discs) are employed in place of the previously used guide shoes, in order to prevent frictional losses and thus to provide a further increase in capacity.

The hollow shell produced in the cross roll piercer is subsequently rolled out in the continuous rolling mill, over a mandrel bar without reheating, to produce a continuous tube. In this process, a maximum elongation of 400% is achieved, corresponding to a reduction in the cross section of 75%.

Continuous mandrel rolling mills consist of between 7 and 9 closely arranged in-line rolling stands, which are offset by 90° to their adjacent neighbours and inclined at 45° to the horizontal. Each stand features its own variable-speed drive motor. The circumferential speeds of the rolls are adjusted to one another, in accordance with the target reductions in cross-sectional area, so as to ensure that there are no appreciable tensile or compression forces acting on the stock between the stands. There is a certain clearance between the mandrel bar and the pipe material in the region of the flanks of the oval pass formed by the two-high rolls (Figure A.3). In the last round pass, this clearance is evenly distributed around the entire circumference, in order to enable the tube to be stripped off from the mandrel bar.

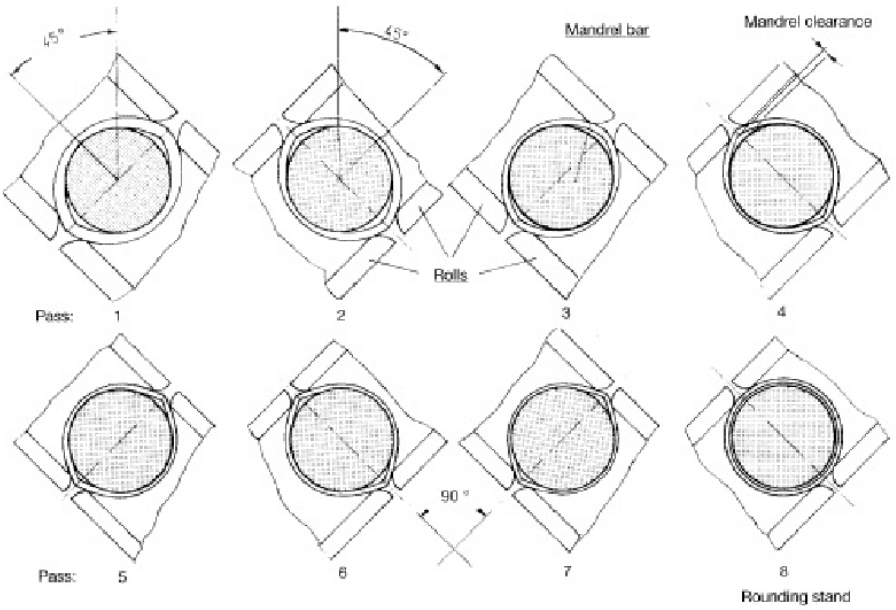

Figure A.3: Roll arrangement of continuous mandrel mill.

Before the beginning of the rolling operation, the mandrel bar is inserted into the hollow shell; then, once it has reached a certain position, the shell/mandrel bar assembly is inserted into the continuous mandrel rolling mill. The stock is gripped by the rolls and elongated from stand to stand as the ever-smaller roll passes act on the mandrel bar. As the speed with which the stock travels through the rolling stands increases, so does that of the mandrel bar. Finally, at a point adjacent to the rolling line, the mandrel bar is removed from the tube, cooled and prepared for the next rolling operation.

In more recent times, rolling practice in mills of this type has reverted to the use of controlled, i.e. constrained, instead of freely floating mandrel bars. The advantage of this process variant lies in the fact that substantially shorter and fewer mandrel bars are required, and that the tube is rolled from the bar; owing to positive forming conditions, larger tube outside diameters can be produced in tube lengths up to 30 m. This version of the continuous mandrel rolling process is also referred to as simply the MPM (Multi-stand Plug Mill) and is becoming increasingly popular for new plant investments throughout the world, in place of larger plug mills.

In the course of this continuous rolling process up to the extraction of the mandrel bar, the tube temperature falls to approximately 500 °C. Consequently, it is fed to a reheating furnace where it is held for between 10 to 15 minutes, in order to enable it to regain a forming temperature of between 950 °C and 980 °C. On exit from the reheating furnace, the tube is rolled to its finished dimensions in the downstream stretch-reducing mill, where no internal tool is used. This can involve further elongation up to ten times the incoming length, depending on the required final dimensions.

Stretch-reducing mills can contain anything between 24 and 28 stands or more, all arranged in a close in-line formation. Nowadays, each stand has its own variable-speed drive and is fit with three rolls of the smallest possible diameter. The three rolls together form a pass which has been offset and becomes progressively smaller from stand to stand.

In accordance with the ever increasing tube length and accompanying reduction in the outside diameter and wall thickness of the tube, the circumferential speed of the rolls continually increases from the inlet to the exit end of the rolling train. Depending on the number of installed stands, various diameters of finished tube can be produced by such an arrangement. Figure A.4 shows the structure and process sequence encountered in a continuous mandrel rolling mill.

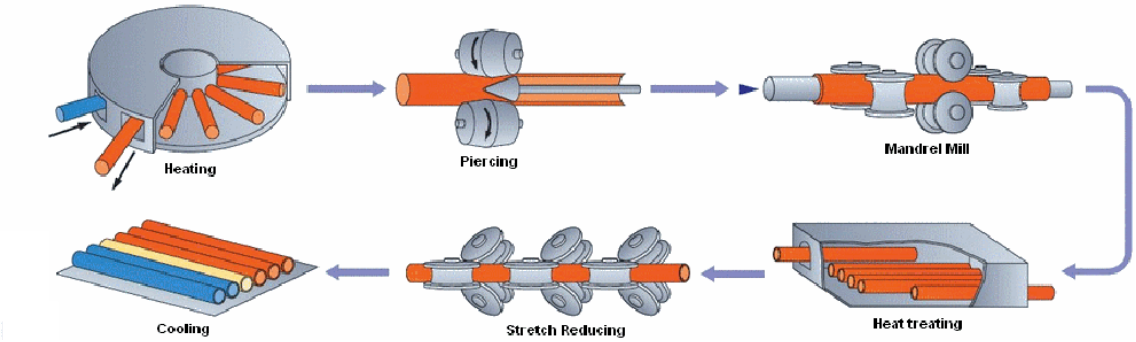

Figure A.4: Schematic representation of a production route for seamless pipe.

Appendix B: Heat transfer: fundamentals

This study falls within the wide field of heat conduction, as targeted on the determination of the temperature distribution and flow of thermal energy within solid bodies. Some fundamental concepts on this topic are presented in this appendix. In particular, the differential equation of heat conduction is derived first in a reference orthonormal Cartesian coordinate system, and then in a cylindrical coordinate system. Finally, the general boundary conditions and initial condition necessary to solve the heat transfer problem are presented. The presentation gathers concepts and notations used in the analytical derivations of the various solutions developed within the body of the thesis.

B.1. Heat flux

The thermal energy exchanged by the constituent particles from a region with a greater local temperature to a region with a lower local temperature is called *heat* (e.g. [38]). Conduction is a specific mode of heat transfer and is linked to the presence of a temperature gradient within the system.

Once the temperature distribution $u(\boldsymbol{r}, t)$ is known within a medium, as a function of space position (defined by position vector $\boldsymbol{r}$) and time (defined by scalar t), heat flow is described by the governing equations of heat transfer. The relationship between the so-called heat flux and the temperature within a body is defined by *Fourier's law* (e.g. [38]). For a homogeneous, isotropic solid (i.e. a material in which thermal conductivity properties are independent of the spatial direction), Fourier's law may be written in the following analytical form:

$$\boldsymbol{q}(\boldsymbol{r}, t) = -k\, \boldsymbol{\nabla} u(\boldsymbol{r}, t) \qquad \text{(B.1)}$$

where:

- $\boldsymbol{q}(\boldsymbol{r},t)$ [W/m^2] is the *heat flux vector* and represents the heat flow per unit time, per unit area of each isothermal surface, with positive component in the direction of decreasing temperature;
- k [W/(m·K)] is the *thermal conductivity* of the material, that is a positive, scalar quantity;
- $\boldsymbol{\nabla} u(\boldsymbol{r},t)$ [K/m] is the temperature gradient ($\boldsymbol{\nabla} = \partial/\partial \boldsymbol{r}$ being the gradient operator), i.e. a vector normal to the isothermal surface $u = const$.

Since the heat flux vector $\boldsymbol{q}(\boldsymbol{r},t)$ points at the direction of decreasing temperature, the minus sign in Eq. (B.1) is included to make the heat flux components as positive quantities where temperature gradient components are negative.

In a reference orthonormal Cartesian coordinate system Eq. (B.1) may be written as:

$$\boldsymbol{q}(x,y,z,t) = q_x \boldsymbol{i} + q_y \boldsymbol{j} + q_z \boldsymbol{k} = -k\frac{\partial u}{\partial x}\boldsymbol{i} - k\frac{\partial u}{\partial y}\boldsymbol{j} - k\frac{\partial u}{\partial z}\boldsymbol{k} \qquad (B.2)$$

where $\boldsymbol{i},\boldsymbol{j},\boldsymbol{k}$ are the unit vectors along the reference x,y,z directions, respectively, and q_x, q_y, q_z are the components of the heat flux vector in the same directions, respectively. The singular heat flux components are then given as:

$$q_x = -k\frac{\partial u}{\partial x}, \qquad q_y = -k\frac{\partial u}{\partial y}, \qquad q_z = -k\frac{\partial u}{\partial z} \qquad (B.3a,b,c)$$

As it is assumed in Eqs. (B.3a,b,c) the heat flow rate at a given temperature gradient is taken as directly proportional to the thermal conductivity k. There is a wide difference in the thermal conductivity of various engineering materials. Typical ranges of the thermal conductivity of various material classes are reported in [45]; values of the thermal conductivity of typical engineering materials are also reported in [45]. For example, for steel materials, a thermal conductivity $k = 45$ W/(m·K) is commonly assumed.

B.2. Differential equation of heat conduction

The differential equation of heat conduction, often called the *heat equation*, may be derived by imposing the general statement of conservation of energy, based on the first principle of thermodynamics. Briefly, the heat equation imposes that the rate of heat entering through the bounding surfaces of a control volume V plus the rate of energy generated internally in it (indicated with $g(\boldsymbol{r},t)$) is equal to the rate of energy stored in it [38], namely:

$$-\int_S \boldsymbol{q}\cdot\boldsymbol{n}\,dS+\int_V g(\boldsymbol{r},t)\,dV=\int_V \rho c\frac{\partial u(\boldsymbol{r},t)}{\partial t}dV \qquad (B.4)$$

where in the first term (rate of heat entering through the bounding surface of a control volume V):

- the minus sign is included to ensure that the heat flows into the volume element V.
- S is the surface area of the control volume V;
- $\boldsymbol{q}$ is the heat flux vector;
- $\boldsymbol{n}$ is the outward-drawn normal unit vector to the surface element dS.

In the third term of Eq. (B.4) (rate of energy stored in V) the following quantities have been introduced:

- ρ is the *mass density* of the control volume V;
- c is the *constant volume specific heat* that is, for an incompressible body, the *constant pressure specific heat*.

Through the divergence theorem it is possible to convert the flux surface integral into a volume integral, as follows:

$$-\int_S \boldsymbol{q}\cdot\boldsymbol{n}\,dS=-\int_V \boldsymbol{\nabla}\cdot\boldsymbol{q}\,dV \qquad (B.5)$$

where $\boldsymbol{\nabla}\cdot\boldsymbol{q}=\ div\,\boldsymbol{q}$ is the divergence field of the heat flux vector in V. In light of Eq. (B.5), Eq. (B.4) may be rewritten as a volume integral in the following form:

$$\int_V \left[-\boldsymbol{\nabla}\cdot\boldsymbol{q}(\boldsymbol{r},t)+g(\boldsymbol{r},t)-\rho c\frac{\partial u(\boldsymbol{r},t)}{\partial t}\right]dV=\boldsymbol{0} \qquad (B.6)$$

Thus, since this shall hold for any arbitrary control volume V, the field equation of heat conduction becomes:

$$-\boldsymbol{\nabla} \cdot \boldsymbol{q}(\boldsymbol{r},t) + g(\boldsymbol{r},t) - \rho c \frac{\partial u(\boldsymbol{r},t)}{\partial t} = 0 \qquad (B.7)$$

Further, by substituting Eq. (B.1) into Eq. (B.7), it is possible to obtain the *differential equation of heat conduction* in the unknown temperature field $u(\boldsymbol{r},t)$:

$$\boldsymbol{\nabla} \cdot k\, \boldsymbol{\nabla}\, \boldsymbol{u}(\boldsymbol{r},t) + g(\boldsymbol{r},t) = \rho c \frac{\partial u(\boldsymbol{r},t)}{\partial t} \qquad (B.8)$$

When the thermal conductivity k is set constant, Eq. (B.8) may be rewritten in the following form:

$$\nabla^2 u(\boldsymbol{r},t) + \frac{1}{k} g(\boldsymbol{r},t) = \frac{1}{\alpha} \frac{\partial u(\boldsymbol{r},t)}{\partial t} \qquad (k = const) \qquad (B.9)$$

where α [m^2/s] is the *thermal diffusivity* defined as:

$$\alpha = \frac{k}{\rho c} \qquad (B.10)$$

and $\nabla^2 = \boldsymbol{\nabla} \cdot \boldsymbol{\nabla}$ is the Laplacian operator, namely in a Cartesian coordinate system (x, y, z):

$$\nabla^2 = \frac{\partial^2}{\partial x^2} + \frac{\partial^2}{\partial y^2} + \frac{\partial^2}{\partial z^2} \qquad (B.11)$$

Then, in the case of a medium with $k = const$ and, further, with no internal heat generation ($g(\boldsymbol{r},t) = 0$) and under steady-state conditions of the temperature variation in time ($\partial u(\boldsymbol{r},t)/\partial t = 0$), the heat equation takes the form of a classical *Laplace's equation* in the unknown temperature field $u(\boldsymbol{r},t)$:

$$\nabla^2 u(\boldsymbol{r},t) = 0 \qquad (B.12)$$

Hereinafter, heat Eq. (B.8) is presented in a Cartesian and in a cylindrical coordinate system, without explicit derivation. Reference is made to [14] for the details.

B.2.1. Differential equation of heat conduction in a Cartesian coordinate system

Given Eq. (B.8) and its particular case Eq. (B.9) above, each of the following relations provides the *heat equation*, i.e. the differential equation of heat conduction, in a Cartesian coordinate system, for a homogeneous, isotropic solid with heat generation g within the body:

$$\frac{\partial}{\partial x}\left(k\frac{\partial u}{\partial x}\right)+\frac{\partial}{\partial y}\left(k\frac{\partial u}{\partial y}\right)+\frac{\partial}{\partial z}\left(k\frac{\partial u}{\partial z}\right)+g=\rho c\frac{\partial u}{\partial t} \qquad (B.13)$$

and, when the thermal conductivity is set constant ($k = const$):

$$\frac{\partial^2 u}{\partial x^2}+\frac{\partial^2 u}{\partial y^2}+\frac{\partial^2 u}{\partial z^2}+\frac{g}{k}=\frac{1}{\alpha}\frac{\partial u}{\partial t} \qquad (B.14)$$

B.2.2. Differential equation of heat conduction in a cylindrical coordinate system

The heat equation in a cylindrical coordinate system (r, ϑ, z) may be obtained from Eq. (B.8) by the following relation, which takes advantage of the representation of the div operator in cylindrical coordinates:

$$\frac{1}{r}\frac{\partial}{\partial r}\left(kr\frac{\partial u}{\partial r}\right)+\frac{1}{r^2}\frac{\partial}{\partial \vartheta}\left(k\frac{\partial u}{\partial \vartheta}\right)+\frac{\partial}{\partial z}\left(k\frac{\partial u}{\partial z}\right)+g=\rho c\frac{\partial u}{\partial t} \qquad (B.15)$$

and, when the thermal conductivity is set constant ($k = const$):

$$\frac{1}{r}\frac{\partial}{\partial r}\left(r\frac{\partial u}{\partial r}\right)+\frac{1}{r^2}\frac{\partial^2 u}{\partial \vartheta^2}+\frac{\partial^2 u}{\partial z^2}+\frac{g}{k}=\frac{1}{\alpha}\frac{\partial u}{\partial t} \qquad (B.16)$$

B.3. General boundary conditions and initial condition for the heat equation

The 2[nd]-order differential equation of heat conduction requires *two* boundary conditions for each spatial dimension and *one* initial condition for the non steady-state problem. The boundary conditions specify the temperature or the heat flux at the boundaries of the region, meanwhile the initial conditions specify the temperature distribution in the medium at the origin of time, namely $u(\boldsymbol{r}, t = 0)$.

At a given boundary surface, the boundary conditions can be prescribed by the temperature distribution (boundary conditions of the First Type), by the heat flux distribution (boundary conditions of the Second Type) or by the heat flux exchange due to *convection* with an adjacent environment at a given temperature (boundary conditions of the Third Type). In the present treatment, for the analytical solution of linear heat conduction problems, such three types of linear boundary conditions are considered and briefly presented in the following, for later use.

It is worthwhile to note that a given boundary or initial condition may be classified as either homogeneous or non-homogeneous, as discussed below.

B.3.1. Boundary Condition of the First Type (Prescribed Temperature)

This is the situation when the temperature is prescribed at the boundary surface, that is:

$$u|_{b.s.} = u_0(\boldsymbol{r}, t), \quad \boldsymbol{r} \in b.s. \tag{B.17}$$

where u_0 is a prescribed temperature distribution described by a function of position on the boundary surface and time. Eq. (B.17) is called a *boundary condition of the first type*. In mathematics, boundary conditions of the first type are called *Dirichlet boundary conditions*.

The special case of zero temperature at the boundary:

$$u|_{b.s.} = 0 \tag{B.18}$$

corresponds to a homogeneous boundary condition of the first type.

B.3.2. Boundary Condition of the Second Type (Prescribed Heat Flux)

This is the situation in which the heat flux in the direction orthogonal to the boundary surface is prescribed at the boundary surface, that is:

$$q_n|_{b.s.} = -k \left.\frac{\partial u}{\partial n}\right|_{b.s.} = q_0(\boldsymbol{r}, t), \quad \boldsymbol{r} \in b.s. \tag{B.19}$$

where $\partial u/\partial n$ is the derivative of the temperature along the outward normal to the surface n and q_0 is a prescribed heat flux distribution described by a function of position on the boundary

surface and time. Eq. (B.19) is called a *boundary condition of the second type*. In mathematics, boundary conditions of the second type are called *Neumann boundary conditions*.

The special case of zero heat flux at the boundary (perfectly insulated or adiabatic):

$$\left.\frac{\partial u}{\partial n}\right|_{b.s.} = 0 \qquad (B.20)$$

is called a homogeneous boundary condition of the second type and states that there is no temperature variation across the boundary surface.

B.3.3. Boundary Condition of the Third Type (Convection)

This is the pure convection boundary condition. The heat flux to or from a surface along normal direction $\boldsymbol{n}$ by convection heat transfer is described by *Newton's law of cooling* as:

$$q_{n_{conv}} = h(u - u_\infty) \qquad (B.21)$$

where u_∞ is the reference temperature of the surrounding ambient fluid (e.g. liquid or gas) and h is the *convection heat transfer coefficient* of units W/(m^2·K). Eq. (B.21) is not tied to the overall coordinate system, since it is locally linked to the outward normal *n* to the body.

The boundary condition can be derived by considering the conservation of energy at the surface, assumed to be stationary and noting that no energy can be stored at an infinitely thin surface. Thus, by writing an energy balance equation at the surface of the body, one obtains:

$$q_{n_{in}} = -k\left.\frac{\partial u}{\partial n}\right|_{b.s.} = h(u|_{b.s.} - u_\infty) = q_{n_{out}} \qquad (B.22)$$

For generality, the ambient fluid temperature u_∞ may be assumed to be a function of position and time, yielding:

$$-k\left.\frac{\partial u}{\partial n}\right|_{b.s.} = h\big(u|_{b.s.} - u_\infty(\boldsymbol{r}, t)\big) \qquad (B.23)$$

Eq. (B.23) is called a *boundary condition of the third type*.

The special case of zero for fluid temperature ($u_\infty = 0$) leads to:

$$-k\left.\frac{\partial u}{\partial n}\right|_{b.s.} = h\,u|_{b.s.} \quad or \quad \frac{h}{k}u|_{b.s.} + k\left.\frac{\partial u}{\partial n}\right|_{b.s.} = 0 \qquad (B.24)$$

Eq. (B.24) is called a *homogeneous boundary condition of the third type*, since the dependent variable or its derivative now appear in all nonzero terms. This represents convection into a fluid medium at zero temperature. Notice that a common practice is to redefine or shift the temperature scale such that the fluid temperature can be reset to zero.

A convection boundary condition is physically different from Type 1 (prescribed temperature) or Type 2 (prescribed flux) boundary conditions in that the temperature gradient within the solid at the surface is now coupled to the convective flux at the solid–fluid interface. Neither the flux nor the temperature are prescribed; rather, a balance between conduction and convection is set, with the exact surface temperature and surface heat flux to be determined by the combination of convection coefficient, thermal conductivity, and ambient fluid temperature. Clearly, the boundary conditions of the first and second type can be obtained from Type 3 boundary conditions as special cases, if k and h are treated as coefficients. Indeed, Eq. (B.24) shows this to be a linear combination of Type 1 and Type 2 boundary conditions, through coefficients h and k.

A few final words are dedicated to these three important boundary conditions. Mathematically speaking, convection boundary conditions introduce the greatest complexity; however, from a physical point of view they are the simplest to occur in practice, since many actual systems are governed by a natural energy balance between conduction and convection; hence, no active control is necessary. In contrast, prescribed temperature boundary conditions, while mathematically simpler, are actually rather difficult to be set in practice, since they are nearly always associated to surface heat flux. Therefore, for a transient problem, a constant temperature boundary condition necessitates a controlled, time-dependent surface heat flux to maintain the prescribed temperature. This is often difficult to be achieved in real situations. A prescribed temperature boundary condition is perhaps best realized when a physical phase change (e.g., evaporation/boiling) occurs at the surface. Alternatively, the constant temperature boundary condition may be thought of as a limiting case of a convective boundary condition as

$h \to \infty$, yielding $u|_{surface} = u_\infty = \text{constant}$. Boundary conditions of the second type may physically correspond to heaters (e.g., thin electric strip heaters) attached to the surface, which with low contact resistance and proper control can provide a prescribed heat flux condition.

Appendix C: Separation of variables

Analytical solutions of boundary value problems ruled by linear ordinary differential equations are usually obtained by producing first a general solution. The general solution is obtained by integration and contains as many independent arbitrary constants as the maximum order of the derivatives in the original differential equation. Incorporation of boundary conditions subsequently defines the values of such integration constants.

In contrast, general solutions of linear partial differential equations involve arbitrary functions of specific functions. Incorporation of boundary conditions involves the determination of functional relationships and is rarely feasible or practical. An alternative solving approach could be based instead on determining first a set of particular solutions and then combining then so as to satisfy the prescribed boundary conditions. A specific, useful and simple implementation of the idea above is known as the method of separation of variables.

In essence, the method is based on the assumption that, here, if one is looking for a solution to a transient, one-dimensional heat conduction problem of the form $u(\boldsymbol{r},t)$, it is possible to express the sought solution by the product:

$$u(\boldsymbol{r},t) = R(\boldsymbol{r})T(t) \qquad (C.1)$$

where the functions $R(\boldsymbol{r})$ and $T(t)$ are each a function of a single independent variable satisfying specific Ordinary Differential Equations (ODEs). One proceeds by first solving the associated ODEs, which are then combined in the product form given above.

Regardless of the space dimensionality of the differential problem, the equation for $T(t)$ is always of the first order and appears readily solvable by elementary methods.

The equation for $R(\boldsymbol{r})$ is always of the second order and, together with the boundary conditions, leads to an eigenvalue problem (proper Sturm-Liouville system). So, by applying the

principle of superposition, the required solution for $R(\boldsymbol{r})$ can be formally and very generally expressed by the following representation (inversion formula):

$$R(\boldsymbol{r}) = \sum_{m=1}^{\infty} K(\lambda_m, \boldsymbol{r})\bar{R}(\lambda_m) \qquad (C.2)$$

where the kernel functions $K(\lambda_m, \mathbf{r})$ are the normalized eigenfunctions of the associated Sturm-Liouville system and the sum runs over all the eigenvalues of the system. Moreover, the integral transform $\bar{R}(\lambda_m)$ is given by the formula:

$$\bar{R}(\lambda_m) = \int K(\lambda_m, \boldsymbol{r}')R(\boldsymbol{r}')d\boldsymbol{r}' \qquad (C.3)$$

Therefore, once the boundary conditions are translated from $u(r,t)$ to $R(r)$, the resulting Sturm-Liouville system is solved, yielding the appropriate eigenfunctions and eigenvalues. From these, one then determines the kernel functions $K(\lambda_m, r)$ and the integral transform $\bar{R}(\lambda_m)$. The inversion formula is used next to obtain function $R(\boldsymbol{r})$. Finally, the desired solution $u(\boldsymbol{r},t)$ is achieved by substituting the obtained expression in the assumed product form.

To summarize, the practical steps to derive the solution are [45]:

- Decompose $u(\boldsymbol{r},t)$ into products of functions of one variable.
- Decompose the PDE into a set of ODEs.
- Identify boundary conditions and the corresponding Sturm-Liouville problems.
- Solve the Sturm-Liouville problems and obtain the corresponding eigenvalues.
- Apply the principle of superposition to obtain the eigenfunction expansion for a general solution.
- Impose the initial conditions to obtain generalized Fourier coefficients of the eigenfunction expansion.

Appendix D: Bessel Functions

A wide treatment on Bessel equations, Bessel functions and their properties is provided e.g. in [1] or [98], and references quoted therein. For the present use, some of such properties are resumed below.

Both $J_v(x)$ and $Y_v(x)$ Bessel functions display on oscillatory behaviour, which is characteristic of all orthogonal functions. Moreover, the following relations hold for Bessel functions of the first kind with zero argument:

$$J_0(0) = 1 \qquad (D.1)$$

$$J_v(0) = 0 \quad for \quad v \neq 0 \qquad (D.2)$$

A second important feature concerns the behaviour of Bessel functions of the second kind as the argument approaches zero, namely:

$$Y_v(x \to 0) \to -\infty \quad for \quad v \geq 0 \qquad (D.3)$$

Typical representations of Bessel functions of the first and second kind are provided below in Figure D.1 and in Figure D.2.

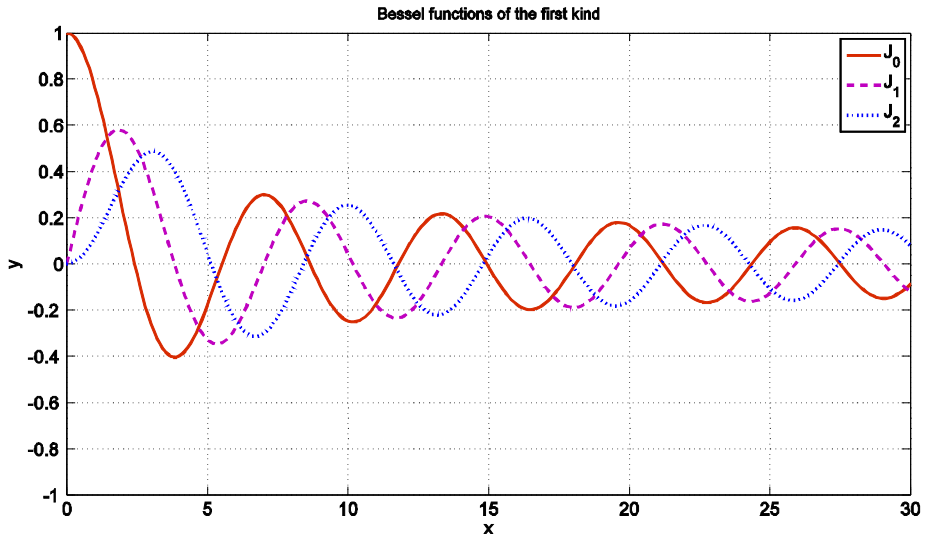

Figure D.1: Bessel functions of the first kind and 0,1,2 order.

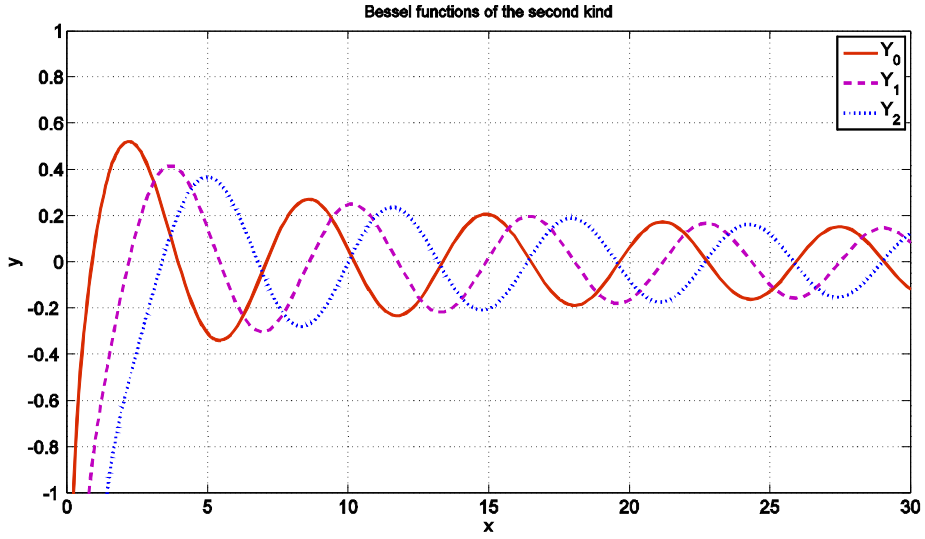

Figure D.2: Bessel functions of the second kind and 0,1,2 order.

It is also useful to list here the first-order derivatives of the Bessel functions $J_\upsilon(x)$ and $Y_\upsilon(x)$, as well as of the Bessel functions $J_\upsilon(\lambda x)$ and $Y_\upsilon(\lambda x)$:

$$\frac{d}{dx}[J_0(x)] = -J_1(x) \quad (D.4)$$

$$\frac{d}{dx}[J_0(\lambda x)] = -\lambda J_1(\lambda x) \quad (D.5)$$

$$\frac{d}{dx}[Y_0(x)] = -Y_1(x) \quad (D.6)$$

$$\frac{d}{dx}[Y_0(\lambda x)] = -\lambda Y_1(\lambda x) \quad (D.7)$$

and

$$\frac{d}{dx}[J_\upsilon(x)] = \frac{\upsilon}{x} J_\upsilon(x) - J_{\upsilon+1}(x) \quad (D.8)$$

$$\frac{d}{dx}[J_\upsilon(\lambda x)] = \frac{\upsilon}{x} J_\upsilon(\lambda x) - \lambda J_{\upsilon+1}(\lambda x) \quad (D.9)$$

$$\frac{d}{dx}[Y_\upsilon(x)] = \frac{\upsilon}{x} Y_\upsilon(x) - Y_{\upsilon+1}(x) \quad (D.10)$$

$$\frac{d}{dx}[Y_\upsilon(\lambda x)] = \frac{\upsilon}{x} Y_\upsilon(\lambda x) - \lambda Y_{\upsilon+1}(\lambda x) \quad (D.11)$$

It is possible to note that Eqs. (D.4)-(D.7) follow directly from Eqs. (D.8)-(D.11) as particular cases, for $\upsilon = 0$.

It is also useful to annotate the Bessel function integration properties:

$$\int x^{v} J_{v-1}(\lambda x)dx = \frac{1}{\lambda} x^{v}\, J_{v}(\lambda x) \tag{D.12}$$

$$\int x^{v} J_{v+1}(\lambda x)dx = -\frac{1}{\lambda x^{v}}\, J_{v}(\lambda x) \tag{D.13}$$

$$\int x^{v} Y_{v-1}(\lambda x)dx = \frac{1}{\lambda} x^{v}\, Y_{v}(\lambda x) \tag{D.14}$$

$$\int x^{v} Y_{v+1}(\lambda x)dx = -\frac{1}{\lambda x^{v}}\, Y_{v}(\lambda x) \tag{D.15}$$

and the indefinite integral of the square Bessel functions:

$$\begin{aligned} \int x^{v} G_{v}^{2}(\lambda x)dx &= \frac{1}{2} x^{2} [G_{v}^{2}(\lambda x) - G_{v-1}(\lambda x) G_{v+1}(\lambda x)] \\ &= \frac{1}{2} x^{2} \left[G'^{2}_{v}(\lambda x) - \left(1 - \frac{v^{2}}{\lambda^{2} x^{2}}\right) G_{v}^{2}(\lambda x) \right] \end{aligned} \tag{D.16}$$

where $G_{v}(\lambda x)$ is any Bessel function of the first or second kind of order v. Prime notation designates differentiation with respect to the entire argument.